The Magnetospheric Structure of Pulsars

by

David H. Roberts

August 1973

SUIPR Report No. 537

National Aeronautics and Space Administration
Grant NGL 05-020-272

National Science Foundation
Grant GP-23840

INSTITUTE FOR PLASMA RESEARCH
STANFORD UNIVERSITY, STANFORD, CALIFORNIA

THE MAGNETOSPHERIC STRUCTURE OF PULSARS

by

David H. Roberts

National Aeronautics and Space Administration
Grant NGL 05-020-272

National Science Foundation
Grant GP-23840

SUIPR Report No. 537

August 1973

Institute for Plasma Research
Stanford University
Stanford, California

ABSTRACT

We describe a model of pulsar magnetospheres which has evolved inductively from the work of Sturrock, where the radiation is produced near the surface of a neutron star. Those observations which are central to our arguments are briefly reviewed. As a foundation for our work we discuss some of the theoretical ideas of others, particularly those of Sturrock.

The braking index n and period-pulse-width distribution of pulsars are first re-investigated by relaxing the conventional assumption that $R_Y = R_L$, where R_Y is the radius of the neutral points marking the transition from closed to open magnetic field lines, and R_L is the radius of the light cylinder. This is replaced by the parametrization $R_Y = R_*^{1-\eta} R_L^{\eta}$, where R_* is the neutron star radius. If the radio frequency radiation is created near the surface and beamed along open field lines, it is found that a good fit to the period-pulse-width distribution can be obtained for η in the range $0.5 \leq \eta \leq 0.7$. The relation $n = 1 + 2\eta$ then gives $n = 2.2 \pm 0.2$, which is in good agreement with the values measured for the Crab pulsar.

Recent observational studies concerning timing irregularities and the dispersion measure of the Crab pulsar and wisp motions in the Crab nebula indicate that pulsar magnetospheres may contain large amounts of non-relativistic gas. We point out that substantial accumulation can occur only in the vicinity of the force-balance radius R_{FB}, where gravitational and centrifugal forces cancel. It is argued that $R_Y \approx R_{FB}$. For this model, the braking index $n = 7/3$ and the expected period-pulse-width distribution and period-age distribution agree well with

observational data. A glitch is interpreted as an instability leading to the ejection and/or dumping of accumulated gas.

We have constructed approximate models for the magnetic field structure, considering in detail the cases of aligned and orthogonal spin and magnetic axes. If the magnetic field is initially closed (out to the light cylinder) gas will collect where there is "microscopic stability". Such locations exist for $r \geq R_{FB}$. Most of this region is "macroscopically unstable" since, when sufficient gas is collected, the centrifugal force overcomes the magnetic stress and converts closed field lines into open field lines. However, there is a small region near $r = R_{FB}$, both microscopically and macroscopically stable, where gas can collect and remain.

Such a magnetospheric structure leads to a braking index $n = 7/3$, in good agreement with the Crab pulsar. We calculate the polar cap boundaries, and the resulting period-pulse-width distribution agrees well with an improved sample of pulsars. The surface magnetic field strengths B_* deduced from this model are roughly a factor of ten less than previous estimates; for the Crab pulsar we find $B_* \approx 2 \times 10^{11}$ gauss.

In conclusion we discuss the ability of the resulting model to account for the observed features of pulsars in general and the Crab pulsar in particular. We mention some shortcomings, and suggest possible future avenues of investigation.

ACKNOWLEDGMENT AND DEDICATION

None of this work would have been possible without the inspiration and encouragement of my advisor, Professor Peter Sturrock. His contributions to the scientific and literary content of this thesis are too many to enumerate. I owe him my thanks.

Discussions with many people have greatly benefited the author, and I would especially like to thank Professor Vahé Petrosian, Dr. Charles Newman, Ms. Mary Fedarko, and Messrs. William Adams, Spiro Antiochos, Joshua Knight and David Smith for their helpful comments and valuable support. Much of the merit of this work is due to the skill of Ms. Evelyn Mitchell, who prepared elegant copy from a ragged manuscript.

This research has been supported by the National Science Foundation under Grant GK-23840 and by the National Aeronautics and Space Administration under Grant NGL 05-020-272.

This thesis is dedicated to the memory of Steve Turk. His incisive understanding and generous help always made my job easier, and his friendship made my life better. I hope it may serve to remind everyone of the better things Steve never got to do.

CONTENTS

LIST OF TABLES

LIST OF FIGURES

Page

Chapter 1

INTRODUCTION

Ever since Gold (1968) made the cogent suggestion that pulsars are basically rotating neutron stars, theoretical studies have followed two more or less distinct lines. First are those which attack the problem of a rotating, conducting, magnetized sphere from first principles. The aim of these papers has been to discover the structure of the electromagnetic fields and plasma surrounding such a neutron star (the magnetosphere). It is assumed that once this has been done, the mechanisms which produce the observed radiation will be discernable.

The second class of studies contains those which examine specific processes which might produce radio, optical, x-ray, or gamma radiation in the vicinity of a neutron star. The magnetic field structure is often prescribed by fiat, and may or may not be related to model magnetospheres studied by others. Broadly speaking, radiation mechanisms may be divided into two groups, depending on whether the radiation is thought to arise near the surface of the star or at the light cylinder.

In this thesis we describe a model of pulsar magnetospheres which has been developed inductively around the hypothesis that radiation is produced near the surface of the star, specifically, at the magnetic poles (Radhakrishnan et al. 1969; Komesaroff 1970; Sturrock 1970, 1971a). Analysis of various data has led us to modify our model in stages, to the point where it can account for a number of important observations in a unified manner.

A short review of the relevant observations is given in Chapter 2. To provide a background and in order to introduce some of the ideas and

definitions which will be used frequently, we discuss briefly some of the important theoretical work of others. The model of Sturrock (1970, 1971a, 1971b) is described in some detail, since it provides the framework upon which this work is based.

The bulk of this thesis consists of three papers by the author and his advisor, Professor Peter Sturrock. They are presented essentially as published, with several appendices to elaborate upon certain calculational details.

In Chapter 3, the braking index n and the period-pulse-width (W-T) distribution of pulsars are re-investigated by relaxing the conventional assumption that $R_Y = R_L$, where R_Y is the radius of the Y-type neutral points marking the transition from closed to open magnetic field lines, and R_L is the radius of the light cylinder. This assumption is replaced by the parametrization $R_Y = R_L^{\eta} R_*^{1-\eta}$, where R_* is the neutron star radius. Comparison is made with the observed braking index of the Crab pulsar, the W-T distributions of two samples of pulsars, and with the number of pulsars showing an interpulse. It is found that a value of η in the range $0.5 \leq \eta \leq 0.7$ is consistent with all of the data. (This material is from Paper I, Roberts and Sturrock 1972a.)

The magnetospheric structure discussed in Chapter 3 (where $R_Y \ll R_L$) is radically different from that usually assumed ($R_Y = R_L$). In Chapter 4 it is shown that such a configuration is a natural consequence of the presence in pulsar magnetospheres of the large amounts of non-relativistic gas which were inferred from observations by Scargle and Pacini (1971). It is argued that in such a case $R_Y \approx R_{FB}$, where R_{FB} is the force-balance distance, the radius at which the gravitational and centrifugal

forces on a corotating particle cancel out. For this model $n = 7/3$, and the resulting W-T and period-age distributions agree well with observational data. A glitch is interpreted as an instability leading to the ejection and/or dumping of accumulated gas. (Paper II, Roberts and Sturrock 1972b.)

This model is explored in greater detail in Chapter 5. We have constructed approximate models for the magnetic field structure, considering in particular the aligned and orthogonal cases. The stability of single particles ("microscopic stability") is studied in detail. The more difficult question of the stability of large amounts of collected material ("macroscopic stability") is discussed in simple physical terms. We find the consequent magnetic field structure and braking index ($n = 7/3$) and the boundaries of the polar caps. The resulting W-T distribution and number of pulsars expected to show interpulses are compared with an improved sample of pulsars. (Paper III, Roberts and Sturrock 1973.)

In Chapter 6 we review our modifications of Sturrock's model, commenting on the limitations as well as the strengths of the results. We discuss areas in which our work may be extended. Finally, we comment briefly on those observations, as yet unexplained, which we believe to be of crucial importance to a fuller understanding of the physics of pulsars.

Chapter 2

REVIEW OF OBSERVATIONS AND PREVIOUS THEORETICAL WORK

I. Observations

There is certainly no dearth of observational facts to challenge the pulsar theorist. Below we present a brief review of those which are especially relevant to our work. The wealth of data which are not presented have been more than amply reviewed by Hewish (1970), Huguenin, Manchester, and Taylor (1971), Ginzburg (1971), ter Haar (1972), and Backer (1973), among others.

Each of the 89 pulsars presently known was first detected by its extremely periodic bursts of radio frequency radiation. The observed repetition period T of the pulses lies between 0.033 sec (Crab, PSR 0531+21) and 3.75 sec (PSR 0525+21), with a median of 0.655 sec. In all cases where the time derivative $\dot{T}$ has been measured it is positive, and the "age" $\tau = T/\dot{T}$ varies between 2.5×10^3 yr (Crab) and 2.5×10^8 yr (PSR 0809+74).

Another observational fact is the relatively short duration W of the pulses compared to the period ($W/T \approx 0.05$). Six of the pulsars (including the Crab pulsar) exhibit an "interpulse" -- a second, smaller pulse which comes roughly half-way between consecutive main pulses. It is also possible to classify pulsars according to pulse shape, and whether they show the "drifting sub-pulse" phenomenon, in which features of the pulse move through the overall envelope from pulse to pulse (Taylor and Huguenin 1971; Backer 1973).

A feature of the radio emission unique to the Crab pulsar is the "precursor". It occurs about 1.6 msec before the main pulse, has no optical counterpart, and is observed only below 600 MHz. Below 400 MHz

its energy is comparable to that of the main pulse, and its duration is roughly five times longer. The polarization is almost 100 percent linear, and the position angle is the same as that of the main pulse.

The extremely accurate timing data which has been accumulated for the Crab and Vela (PSR 0833-45) pulsars exhibit additional features which require explanation. First, the "braking index" n ($n = \omega\ddot{\omega}/\dot{\omega}^2 = 2 - T\dddot{T}/\ddot{T}^2$), which measures the frequency dependence of the torque which slows the neutrons star's rotation (torque $\propto \omega^n$), has been measured for the Crab pulsar; it is found to have a value $n = 2.4 \pm 0.2$ (Boynton et al. 1972). Second, the slow-down is not smooth, but exhibits both seemingly random "noise" (Crab) and larger, apparently discontinuous, jumps in frequency. Two such "glitches" have been observed for each of these pulsars; $\Delta\omega/\omega \approx +10^{-9}$ for the Crab pulsar, and $\Delta\omega/\omega \approx +10^{-6}$ for the Vela pulsar. According to Boynton et al. (1972), the noise seen in the Crab may be well represented by mini-glitches of $\Delta\omega/\omega \leq 2 \times 10^{-10}$ occurring at least once per week.

Differences in the times of arrival of a pulse at two different frequencies may be expressed in terms of the dispersion measure

$$D_{ij} = \frac{t(\nu_i) - t(\nu_j)}{\nu_i^{-2} - \nu_j^{-2}} \quad . \tag{2.1}$$

When the radio frequency is much greater than the plasma frequency $\nu_p = (n_e e^2/\pi m_e)^{1/2}$,

$$D_{ij} \simeq (1/2c)\int \nu_p^{\,2}\, d\ell = 10^{-2.88}\int n_e\, d\ell \quad . \tag{2.2}$$

Careful observations of the Crab pulsar (Rankin, Counselman, and Richards 1971; Rankin, Campbell, and Counselman 1971; Rankin and Counselman 1973) show that its dispersion measure (nominally about 2.36×10^{17} sec Hz^{-2}, so that $\int n_e \, d\ell \approx 56.8$ parsec cm^{-3}) is not strictly constant, but shows variations on the order of 2 parts in 10^4 on time scales of months. One such change in integrated plasma density occurred during a two month period beginning around the time of the September 1969 glitch. However, similar fluctuations have occurred without being associated with timing irregularities, and no increase in dispersion measure followed the Crab glitch of October 1971.

Careful observations of small-scale features ("wisps") in the Crab nebula near the pulsar have revealed motions and brightenings that may be associated with timing irregularities of the pulsar (Scargle 1969; Scargle and Harlan 1970; Scargle and Pacini 1971). Correlations are claimed for small irregularities occurring near March 10 and June 1, 1970, as well as with the large glitch of September 1969, but there was no activity following the large glitch of October 1971. The energy required for these events is claimed to be at least 10^{41} ergs (Scargle and Harlan 1970).

The high brightness temperature of the rf radiation was seen from the outset to require a coherent mechanism. (Assuming the radiation comes from a region of linear dimension less than cW, the brightness temperature is about 10^{20}-10^{25} ^{o}K.) It appears that the rf signals display (in addition to interstellar scintillation effects) fluctuations intrinsic to the source, notable examples of which are the drifting subpulses, the "nulling" phenomenon (Backer 1970), and the "giant pulses" of the Crab pulsar (Sutton, Staelin, and Price 1971). There is a great deal of

spectral information concerning pulsars. In general, there is a low frequency cut-off around 100 MHz and the radio flux is a decreasing function of frequency. In addition, the rf radiation is frequently strongly linearly polarized, and is often found that the electric vector sweeps through a large angle during a pulse (Radhakrishnan et al. 1969).

Pulsed radiation in other frequency bands, coincident (after correction for dispersion delays) with the rf pulses, has been detected from the two fastest pulsars (Crab and Vela). While the Vela pulsar has been detected only in x-rays (Harnden et al. 1972), the Crab has been observed in the optical (Cocke et al. 1969), x-ray (Fritz et al. 1969) and gamma-ray (Hillier et al. 1970) spectral ranges. The ratio of energy in the interpulse to that in the main pulse, which is small in the radio band, grows steadily from the optical through the gamma-ray, where it is larger than unity.

The optical pulse of the Crab pulsar is exceedingly stable. The main pulse-interpulse configuration is asymmetric, and exhibits a cusp-like main peak, unresolved on a time scale of 30 microseconds (Papaliolios et al. 1970). The optical pulse shows some linear but no circular polarization. The electric vector sweeps through an angle of 130° during the main pulse, and is parallel to that of the rf pulse at the peak (Manchester 1971a). The spectrum of the optical pulses has a broad maximum in the visual part of the spectrum, and turns over in the infrared. The spectrum apparently extends into the x-ray band and from there to the gamma-ray band. There was no change in the optical pulse shape or intensity during or following the September 1969 glitch.

II. Pulsar Electrodynamics-Canonical Models

One possible approach was taken by Pacini (1968) and Ostriker and Gunn (1969; Gunn and Ostriker 1969, 1970). They examined the dynamics of an object possessing gravitational or magnetic fields not symmetric about the rotation axis. In a vacuum, electromagnetic and gravitational energy is radiated at rates given by

$$dE_{md}/dt = -\frac{2}{3} m_{\perp}^{2} \omega^{4}/c^{3} \tag{2.3}$$

and

$$dE_{gq}/dt = -\frac{1}{45} G D_{\perp}^{2} \omega^{6}/c^{5} . \tag{2.4}$$

Here $m_{\perp}$ and $D_{\perp}$ are the components of the magnetic-dipole and mass-quadrapole moments perpendicular to the rotation axis. Such an object, if rotating almost rigidly, will also loose angular momentum at a rate given by

$$dJ/dt = \omega^{-1} dE/dt . \tag{2.5}$$

Thus the braking indices for these models are $n = 3$ (magnetic dipole radiation) and $n = 5$ (gravitational quadrapole radiation).

Surface magnetic fields of 100 gauss are not unreasonable for young, massive stars, the likely progenetors of neutron stars. Flux conservation in a collapse from a radius R_{*} of 10^{11} cm would produce a surface field B_{*} on the order of 10^{12} gauss at $R_{*} = 10^{6}$ cm. Thus the magnetic moment $R_{*}^{3} B_{*} \approx 10^{30}$ emu for the resulting neutron star, and Eq. (2.3) becomes

$$dE_{md}/dt \approx -10^{28.3} \omega^{4} \text{ erg s}^{-1} . \tag{2.6}$$

The Crab pulsar has $\omega \approx 10^{2.3}\ s^{-1}$, so $\dot{E}_{md}^{Crab} \approx -10^{37.5}\ erg\ s^{-1}$. This interpretation is strengthened by the observation (Gold 1969) that if it is slowing down, it is losing rotational energy at the rate

$$-\frac{d}{dt}\left[(1/2)I_*\omega^2\right] = -I_*\omega\,\dot{\omega}\ erg\ s^{-1} \quad . \tag{2.7}$$

Neutron star models have moments of inertia $I_* \simeq 10^{44.5}\ g\ cm^2$, the Crab is observed to have $\dot{\omega} \simeq -10^{-9.6}\ s^{-2}$, so the energy loss is $\approx 10^{37.2}$ erg s^{-1}. In addition, this is about the right amount of energy that is required to power the Crab nebula (Shklovsky 1968; Haymes et al. 1968; Wang and Sartori 1973).

Combining Eqs. (2.3) and (2.7), we may express the surface magnetic field in terms of the observed slow-down rate:

$$B_* \simeq \left(\frac{3c^3 I_*}{2\pi\omega^2 R_*^6}\right)^{1/2} = \left(\frac{-3c^3 I_*}{2R_*^6}\frac{\dot{\omega}}{\omega^3}\right)^{1/2} = \left(\frac{3c^3 I_*}{8\pi^2 R_*^6}\right)^{1/2} (T\dot{T})^{1/2}. \tag{2.8}$$

It is rather remarkable that although $\dot{T}$ varies over three orders of magnitude and T over two orders, the magnetic field (evaluated for a given neutron star model from Eq. [2.8]) varies by only a factor of four for the 25 measured pulsars. However, the large range of $I_*^{1/2}/R_*^3$, especially for small neutron stars masses, makes it impossible to determine magnetic fields to better than 3-4 orders of magnitude (Greenstein 1972).

Gravitational radiation will always dominate over magnetic radiation if the frequency is sufficiently high. However, the measured braking index of $n \approx 2.4$ for the Crab pulsar implies that this is not important at the present epoch, and we will not discuss it further.

The simplest model of a pulsar magnetosphere starts with a neutron star possessing a dipolar magnetic field, its magnetic axis parallel (or antiparallel) to its spin axis. Although it is obvious that such a time-independent axisymmetric model cannot account for the pulses, it is usually assumed (and Mestel [1971] has shown this to be very plausible) than an oblique rotator will be qualitatively the same as an aligned rotator.

The pioneering calculation was that of Goldreich and Julian (1969), who noted that the extremely good conductivity inside the star requires that

$$\vec{E} + \left(\frac{\vec{\omega} \times \vec{r}}{c}\right) \times \vec{B} = 0 \ . \tag{2.9}$$

If there are no charges surrounding the star, the potential for $r > R_*$ may be found from Laplace's equation. The resulting electric field is quadrapolar, there is a surface charge

$$\sigma = - \frac{B_* R_* \omega}{4\pi c} \cos^2\theta \ , \tag{2.10}$$

and outside the star

$$\vec{E} \cdot \vec{B} = - \frac{\omega R_*^8 B_*^2}{c\, r^7} \cos^3\theta \ . \tag{2.11}$$

However, for the magnetic fields ($B_* \approx 10^{12}$ gauss) in pulsars such a configuration is highly unstable, since the non-zero electric force along the magnetic field is enormously greater than the gravitational force. Unless quantum effects at the surface are sufficient to bind the charges (Ruderman 1971; Ginzburg and Usov 1972), they are pulled off into the magnetosphere and behave as a conducting extension of the star. In this

case, as long as inertial and gravitational forces are small compared with electric forces, the Lorentz force law and infinite conductivity require that $\vec{E} \cdot \vec{B} = 0$ outside the star as well as inside. The resulting motion of charged particles is a combination of corotation and motion along field lines. When the contribution of the corotating charge to the magnetic field is included, the charge density outside the star is approximately

$$n_+ - n_- = \frac{-\vec{\omega} \cdot \vec{B}}{2\pi ec} \left[\frac{1}{1-(\omega r/c)^2 \sin^2\theta} \right] . \qquad (2.12)$$

This applies only to the corotating part of the magnetosphere, which consists of those magnetic field lines which lie entirely within the "light cylinder". The radius of the light cylinder, where the corotation speed is equal to the speed of light, is given by

$$R_L = c/\omega = cT/2\pi . \qquad (2.13)$$

Field lines which penetrate the light cylinder must be open in order that particle velocities remain less than c.

The torque N on the star is obtained by integrating the Maxwell stress tensor over a spherical surface centered on the star. The result is

$$N \simeq B_*^2 R_*^6 \omega^3 / 8c^3 = \frac{1}{8} \left[B_* (R_*/R_L)^3 \right]^2 R_L^3 \qquad (2.14)$$

where R_* is the radius of the neutron star, and B_* the polar magnetic field strength at the surface. From Eq. (2.14) we see that the braking index in the Goldreich-Julian model is $n = 3$. Equation (2.14) leads to an energy loss comparable to that from a vacuum rotator.

Although this model surely possesses some of the most important features, it is not a self-consistent solution of Maxwell's equations and the dynamical laws. Attempts to extend this analysis have been made by Scharlemann and Wagoner (1973), Michel (1973a, 1973b) and Julian (1973), who also neglect inertial and gravitational forces. However, these calculations seem to require specification of the current at the surface of the star or the configuration of the magnetic field at infinity. Thus it is not clear that a unique solution exists, at least as the problem has been posed. (It is contended that inclusion of inertia will make the solution unique, but this has yet to be demonstrated.)

The equation of motion

$$d(I_* \omega)/dt = -N = -A\omega^n \tag{2.15}$$

may be integrated easily. Assuming that A and I_* are independent of time, and the present epoch to be $t = 0$,

$$\omega(t) = \omega(0)\,[1 + (n-1)t/\tau]^{1/(1-n)}\ , \tag{2.16}$$

where

$$\tau = T/\dot{T}\Big|_{t=0} = -\omega/\dot{\omega}\Big|_{t=0}\ . \tag{2.17}$$

For magnetic braking ($n = 3$), the frequency becomes singular at a time $t = -\tau/2$. For the Crab pulsar, this agrees reasonably well with the birth of the Crab nebula in 1054 AD. Or taking the age of the Crab pulsar as 919 years and $n = 3$, $\omega(\text{birth}) = 2.3\,\omega(0)$. Lowering n towards the observed value decreases $\omega(\text{birth})$, but not very much. However, the largest n that could have operated from birth is about 3.4.

An excellent review of pulsar electrodynamics and pulsar dynamics has been provided by Ruderman (1972).

III. Radiation Mechanisms

Although these two models explain reasonably well the kinematics of pulsar slow-down and the energy budget of the Crab nebula, neither attempts to account for the observed pulses. Many theoretical ideas concerning the nature of the radiation mechanism were advanced soon after the discovery of pulsars (see, for instance, Hewish 1970). Most of these ideas have died quietly, either from neglect or under the weight of adverse evidence. One school of thought, stimulated by an early suggestion by Gold (1968), holds that radiation is produced by relativistic particles in the vicinity of the light cylinder. This difficult problem has been attacked by Shklovsky (1970), Eastlund (1968, 1970), Lerche (1970a, 1970b), Pacini and Rees (1970), and others. However, Michel (1973a) has recently shown that in a self-consistent inertia-less model where all the plasma corotates and does not flow along field lines, the radiation arising at the light cylinder is too low by a factor of about 10^8 to be the source of pulsar rf radiation.

Proceeding in the direction first indicated by Radhakrishnan et al. (1969), other theorists (Komesaroff 1970; Pacini and Rees 1970; Sturrock 1970, 1971a; Tademaru 1971) have explored in detail the idea that the short duty cycle and linear polarization sweep of the rf radiation are consequences of emission near the neutron star surface at the magnetic poles. These models require that the flow of charged particles at the polar caps should be bunched. It has also been proposed (Chiu and Canuto 1971; Ginzburg et al. 1969) that an alternative way of obtaining radiation

of high brightness temperature is through some kind of maser mechanism.

ter Haar (1972) has reviewed these and other suggestions, and the reader is referred to his article for a thorough discussion of the merits and shortcomings of these and other proposals. In what follows we shall be concerned with those models in which the radiation is produced close to the surface of the neutron star at the magnetic polar caps.

IV. Sturrock's Pulsar Model

Sturrock (1970, 1971a, 1971b) has constructed a model of pulsars extending the work of Goldreich and Julian (1971), but relaxing their assumption that the electric and magnetic fields are everywhere orthogonal. In the Goldreich-Julian model there is a toroidal (B_φ) component so that the integral $\oint \vec{B} \cdot d\vec{s}$ around the light cylinder is non-zero. This means that curl $\vec{B}$ is non-zero, which implies that there are currents flowing in the system. The distribution of these currents, which flow from the magnetic polar caps out to infinity, may be roughly inferred from the magnetic field configuration. There must be a positive current from an angular ring and a negative current from the center of the polar cap, or vice versa, depending on whether the magnetic and spin axes are aligned or anti-aligned. This view was advanced also by Goldreich and Julian.

At this point Sturrock departs from Goldreich and Julian by noting that a laboratory device such as an electron gun will not give a current unless a voltage is applied to it. In fact there is a source of voltage at the polar cap, namely the rotation-induced electric field. For the case of the Crab pulsar, ions would accelerate to about 10^{16} eV per electronic charge. Because of radiation reaction, electrons will reach only about 10^{14} eV. This acceleration occurs very close to the star,

probably within a kilometer of the surface. Since the ions and electrons move along the curved magnetic field lines, they are copious emitters of high energy gamma-rays (of order 10^{12} eV).

The key mechanism in Sturrock's model is the conversion of these high energy gamma rays into electron-positron pairs in the intense magnetic field. The gamma rays are produced by curvature radiation and initially move parallel to the magnetic field. However, since the field is curved, they soon see a transverse component of magnetic field. When the condition E_γ (eV) $B_\perp$ (gauss) $\geq 10^{18.6}$ is met, the gamma ray will annihilate into an electron-positron pair.

There are two important consequences of this pair creation. One is that the electrons and positrons are produced with non-zero pitch angles, and will therefore radiate by the synchrotron mechanism, possibly in the gamma, x-ray, or optical regions of the spectrum. Some of the gamma rays produced by the secondary electrons will in turn annihilate into e^+e^- pairs, and so on. The resulting cascade produces about $10^{7.5}$ secondaries per primary electron, and the total number of relativistic leptons injected into the Crab nebula is around $10^{41} s^{-1}$. This agrees with the number required to produce the synchrotron radiation from the nebula (Shklovsky 1968).

The other consequence follows from the fact that some positrons will probably be turned around by the electric field and flow toward the surface. If this happens there will be a two-stream configuration which is known to be very unstable. This is likely to lead to bunched rather than steady flow. If bunches of electrons are moving along curved field lines, then radio emission will be produced by the mechanism outlined by

Radhakrishnan and Cooke (1969), and more fully analyzed by Tademaru (1971). This radiation is beamed along the direction of the magnetic field, and is polarized along the projection of the magnetic field seen by the observer. Thus, as pointed out by Radhakrishnan et al. (1969), the electric vector will sweep in position angle as the line of sight of the observer passes through the polar cap.

The hypothesis that pair creation is responsible for the radio emission may be tested (Sturrock 1971b). Expressing the magnetic field and the electron energies (via the electric field) in terms of the period T and the age τ, the condition that pairs can be created in the electron polar zone (EPZ) may be written as

$$T < T_{ePC} = 10^{-14.0} I_*^{2/3} R_*^{-1} \tau^{-2/3} . \qquad (2.18)$$

Similarly, for pair creation in the ion polar zone (IPZ), the requirement is

$$T < T_{iPC} = 10^{-17.3} I_*^{2/3} R_*^{-1} \tau^{-2/3} . \qquad (2.19)$$

Here I_* (g cm^2) is the moment of inertia of the neutron star. These conditions are compared with the observed period-age distribution in Figure 2.1. It is seen that radio emission ceases approximately where one would expect pair production to end in the EPZ. The condition (2.19) is satisfied for only the Crab pulsar, and Sturrock (1970) has suggested that this offers an explanation of why the Crab pulsar alone shows a precursor (a similar suggestion has been advanced by Pacini [1971]).

The spectrum computed on the basis of this model account fairly well for the radio emission. The x-ray emission of the Crab pulsar may be

understood reasonably well if it comes from the IPZ.

On the basis of this model, Sturrock made three predictions. First, that gamma radiation should be detectable from the Crab pulsar. This has been verified. Second, that x-rays should be observable from the Vela pulsar. This, too, has been verified. The third prediction was that the polarization of the optical radiation should have an electric vector orthogonal to that of the radio emission. This has been found to be untrue (Manchester 1971a), and has led to the abandonment of the mechanism originally proposed for the optical radiation. Recently, Turk, Sturrock, and Petrosian (1973) have shown that coherent curvature radiation from first or second generation secondary electrons can account for the optical radiation from the Crab pulsar.

However, Sturrock's model predicts a braking index of $n = 3$, and pulse widths that are much smaller than those which are observed. The way in which we have modified his model to account for these observations, as well as provide a basis for understanding the irregularities in the timing data, is described in the subsequent chapters.

FIGURE CAPTION

Figure 2.1. Distribution of pulsars in period T and age τ, compared with the predictions of Eqs. (2.1) and (2.2) (Sturrock 1971b). ●, S-type structure; △, C-type structure; □, D-type structure, in the notation of Taylor and Huguenin (1971). The theoretical curves are based on the assumption that $R_Y = R_L$.

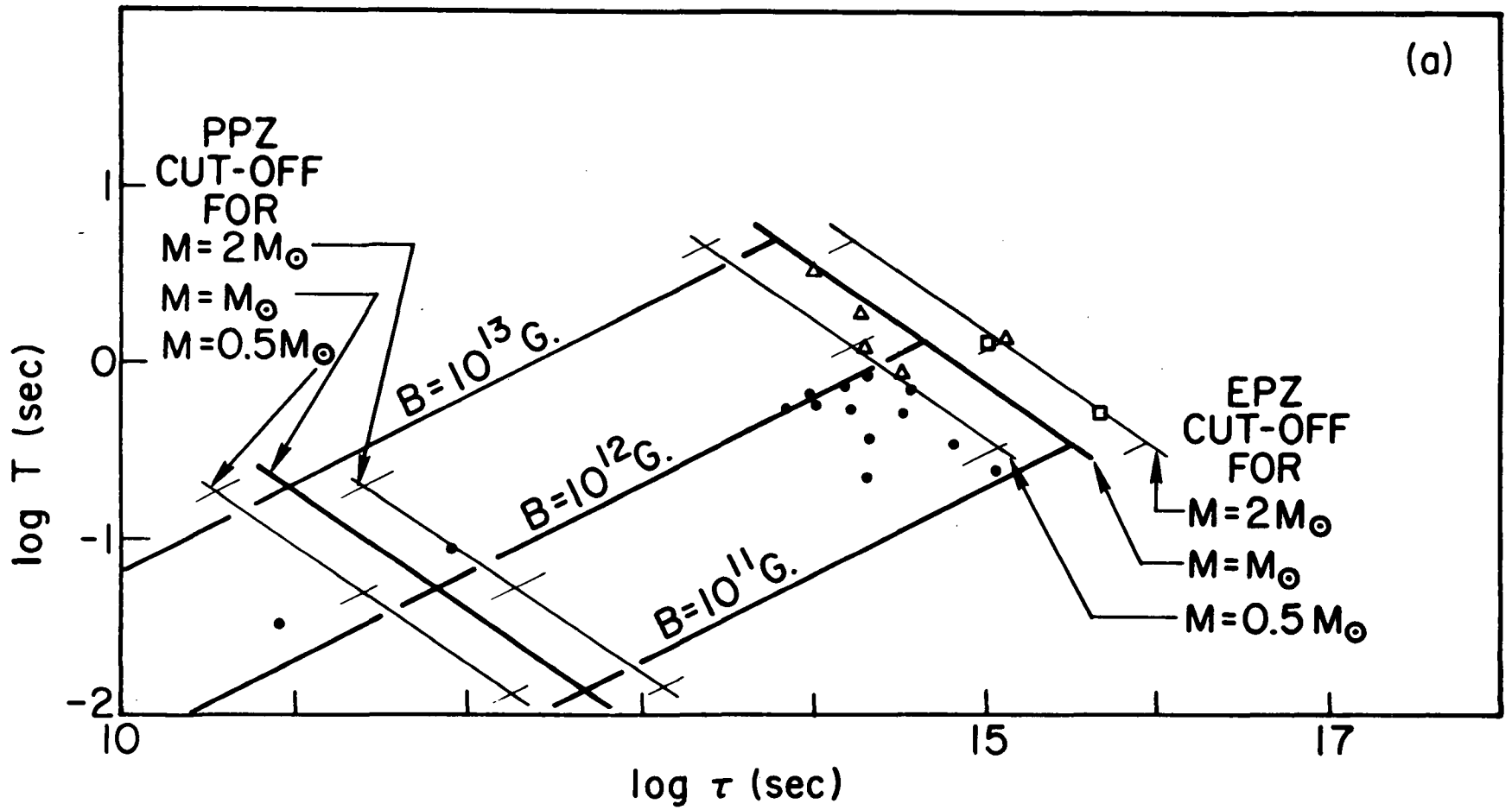
(a)
PPZ
CUT-OFF
FOR
M = 2 M⊙
M = M⊙
M = 0.5 M⊙
B = 10^13 G.
B = 10^12 G.
B = 10^11 G.
EPZ
CUT-OFF
FOR
M = 2 M⊙
M = M⊙
M = 0.5 M⊙
log T (sec)
log τ (sec)
1
0
-1
-2
10
15
17

Figure 2.1

Chapter 3

THE BRAKING INDEX AND PERIOD-PULSE-WIDTH DISTRIBUTION

I. Introduction

Although there is some uncertainty concerning the braking index for the Crab Pulsar, it is generally agreed that the observations cannot be reconciled with any existing theory (Richards et al. 1970; Duthie and Murdin 1971; Roberts and Richards 1971). Likewise, there is a problem concerning the distribution of pulsars in period (T, sec.) and pulse-width (W, sec.). As noted by Gunn and Ostriker (1970), one expects that the observations should satisfy the law $W \propto T^{1/2}$ if the (RF) radiation is produced near the polar caps defined as those areas of the surface of a neutron star coupled by magnetic-field lines to the light cylinder.[1] The purpose of this chapter is to show that both sets of observations may be understood in terms of a modified polar cap model.

II. Model--Braking Index

It is generally assumed that the transition from closed to open magnetic field lines occurs at the light cylinder, as proposed by Goldreich and Julian (1969). It is clear that the radius R_Y of the "Y-type" neutral points (Sturrock and Smith 1968), which characterize the transition from closed to open field lines, cannot occur outside the light cylinder, which has radius $R_L = cT/2\pi$. However, it is not at all clear that R_Y cannot be less than R_L. Sturrock (1971b) has suggested that one consider R_Y to be determined as follows:

---

[1] Gunn and Ostriker find that a better fit is $W \propto T^{0.7}$, which corresponds to $\eta = 0.6$ in the model to be described.

$$R_Y = R_*^{1-\eta} R_L^{\eta} , \tag{3.1}$$

where η is a parameter in the range $0 < \eta \leq 1$. If one notes that the magnetic field strength varies as r^{-3} in the range $R_* < r < R_Y$ and as r^{-2} in the range $R_Y < r < R_L$, and if one notes that one should retain the assumption that the magnetic-field spiral-angle is about 45^o at the light cylinder, one finds that the formula for the magnetic torque N given by Sturrock (1971a) is replaced by

$$N = \frac{1}{2} B_*^2 R_*^6 R_Y^{-2} R_L^{-1} , \tag{3.2}$$

where $R_*(\text{cm})$ is the radius of the star and $B_*(\text{gauss})$ is the value of the magnetic field at the surface of the star. On using equation (3.1), this becomes

$$N = \frac{1}{2} B_*^2 R_*^{4+2\eta} R_L^{-1-2\eta} , \tag{3.3}$$

which shows that $N \propto T^{-1-2\eta}$. Hence the braking index n is given by

$$n = 1 + 2\eta . \tag{3.4}$$

III. Period-Pulse-Width Distribution

We next consider the period-pulse-width distribution to be expected on the basis of equation (3.1), by extending the analysis of Henry and Paik (1969). We assume that radiation is due to charge sheets moving along open magnetic-field lines at the polar caps. We consider, for definiteness, that the dominant contribution is produced close to the surface of the star, but the conclusions are not greatly affected if the radiation is produced within a few star-radii.

If the magnetic dipole axis makes an angle Θ with the rotation axis, field lines which are tangent to a cylinder of radius R_Y, parallel to the rotation axis, define a polar cap at each magnetic pole. The semi-major-axis is of angular size $R_*^{1/2} R_Y^{-1/2}$ and is in the direction of increasing longitude (referred to the rotational axis); the semi-minor-axis is of angular size $R_*^{1/2} R_Y^{-1/2} G(\Theta)$ and is in the direction of increasing latitude. $G(\Theta)$ varies slowly over the range $G(0) = 1$ to $G(\pi/2) = .620$. If the radiation polar diagram is defined by the cone which is tangent to the field lines passing through the boundaries of each polar cap, the major and minor half-angles of this cone are

$$\psi_\ell = \frac{3}{2} R_*^{1/2} R_Y^{-1/2} , \quad \psi_b = \frac{3}{2} R_*^{1/2} R_Y^{-1/2} G(\Theta) . \tag{3.5}$$

The details of this calculation are given in Appendix A.

If ϕ is the angle between the rotation axis and the line of sight, the pulse-width W is given by

$$W = \frac{T\psi_\ell}{\pi \sin \phi} \left[1 - \frac{(\phi - \Theta)^2}{\psi_b^2} \right]^{1/2} \tag{3.6}$$

for one polar cap, and a similar expression $(\Theta \to \pi - \Theta)$ for the other polar cap. (If W is found to be imaginary, radiation is not detectable by the observer.)

If we assume that the rotation axis is randomly oriented, and if we assume that the magnetic axis is randomly oriented with respect to the rotation axis, we find (neglecting certain terms of order W/T) that the probability that radiation from either pole is observed and has a pulse width in the range W to $W + dW$ is

$$P_W(W,T)dW = T^{-1} L(x)\, dW . \tag{3.7}$$

In this expression,

$$x = ky \tag{3.8}$$

where

$$y = T^{2-\eta} W^{-2} \tag{3.9}$$

and

$$k = \frac{9}{4\pi^2}\left(\frac{2\pi R_*}{c}\right)^{\eta} . \tag{3.10}$$

The function $L(x)$ is given by

$$L(x) = 2\pi \int_0^{\Theta_m} d\Theta \, \frac{\sin^4\Theta \, G(\Theta)}{(x-\sin^2\Theta)^{1/2}} , \tag{3.11}$$

where

$$\left.\begin{aligned} \Theta_m &= \text{arc sin } x^{1/2} , \quad x \le 1 \\ &= \pi/2 , \quad x > 1 . \end{aligned}\right\} \tag{3.12}$$

In order to make comparison with observational data, it is easier to consider the probability that a pulsar of period T is characterized by a value of y in the range y to $y + dy$. This is given by

$$P_y(T,y)dy = \frac{1}{2} T^{-\eta/2} \, y^{-3/2} \, L(ky) \, dy . \tag{3.13}$$

We denote by $F(T)dT$ the "population" of pulsars (sufficiently close and sufficiently luminous to be observed) with periods in the range T to $T + dT$. If $f(y)dy$ is the number of pulsars which are observed to be characterized by values of y in the range y to $y + dy$, then

$$f(y) = \int_0^\infty dT\ P_y(T,y)\ F(T)\ . \qquad (3.14)$$

On using equation (3.13) and noting that N_o, the total number of pulsars observed, is given by

$$N_o = \int_0^\infty f(y)dy\ , \qquad (3.15)$$

we find that

$$f(y) = N_o \lambda^{-1}\ k^{-1/2}\ y^{-3/2}\ L(ky)\ , \qquad (3.16)$$

where

$$\lambda = \int_0^\infty dz\ z^{-3/2}\ L(z)\ . \qquad (3.17)$$

A more detailed, generalized, derivation of equation (3.13) is made in Appendix B. In Appendix C we discuss the calculation of the function $L(x)$ and its integrals.

IV. Comparison with Observational Data

Two sets of histograms have been constructed from observational data for comparison with the theoretical distribution given by equation (3.16). We adopt $R_* = 13.5$ km, which is close to the values computed by Cohen and Cameron (1971) for neutron stars in the mass range $0.3M_\odot \leq M_* \leq 2M_\odot$. The theoretical histogram is taken from Appendix C; its midpoint is found from the relation $x_{peak} = 1$, i.e., $\log y_{peak} = -\log k$, with k given by equation (3.10). Using the values of y computed from the data for each η, the observed distribution is constructed for the same bins around y_{peak} that were used for the theoretical distribution.

To make Sample A as large as possible, we have included all 49 pulsars for which pulse widths had been published at the time Paper I was written (Davies and Large 1970; Maran and Modali 1970). To make this sample as uniform as possible, we have adopted for the width the value W quoted by Maran and Modali which, in some cases, is the "full width" and in other cases is the "equivalent width". Sample B consists of the 13 pulsars for which Gunn and Ostriker (1970) list more careful measurements, and 5 additional pulsars from Maran and Modali (1970). These are listed, with our judgment of the best measure of W, in Table 3.1.

Histograms formed from Sample A are compared with histograms generated from the theoretical distribution in Figure 3.1, for a range of values of η. The best fit is found in the range $0.6 \leq \eta \leq 0.7$. The fact that the widths of the curves do not match too well is attributed to the intrinsic scatter in the measured pulse widths. Similar results are obtained from samples composed of those 25 pulsars with $T > 0.7$ sec and of those 24 pulsars with $T < 0.7$ sec.

Histograms formed from Sample B are compared with the theoretical histogram in Figure 3.2, for a range of values of η. For this sample, the best fit seems to occur in the range $0.5 \leq \eta \leq 0.6$. Although Sample B is smaller than Sample A, it gives a better fit to the theoretical curve. One may attribute the change in the value of η which gives the best fit, in going from Sample A to Sample B, to the fact that the total width is greater than the equivalent width.

The above considerations suggest that $\eta = 0.6 \pm 0.1$. This uncertainty may reflect errors in the determination of η, or it may reflect

a real variation of η among pulsars and/or in time. We see from equation (3.4) that this leads to a braking index $n = 2.2 \pm 0.2$. This quantity has been measured only for the Crab pulsar, for which various values have been proposed. Among the more recent publications, Richards et al. (1970) give $n = 2.16 \pm 0.10$; Duthie and Murdin (1971) give $n = 2.229 \pm 0.003$; and Roberts and Richards (1971) quote a range of values (for different time intervals) varying from $n = 1.80$ to $n = 2.88$. It appears that the value of n (and hence of η) for the Crab pulsar may well vary, and that these changes in magnetospheric structure are related to irregular changes in period, but that the mean value of n for the Crab pulsar is not very different from that inferred for Samples A and B.

V. Interpulse Phenomenon

We may consider the number of pulsars which one might expect, on the basis of the above model, to show an interpulse. Geometrical considerations, discussed in detail in Appendix D, show that the probability $P_1(T)$ that an observer will see at least one pulse from a pulsar of period T is given by

$$P_1(T) = 3(R/R_Y)^{1/2} \int_0^{\pi/2} \sin^2\Theta \, G(\Theta) \, d\Theta = 1.863 \, (R_*/R_Y)^{1/2} , \qquad (3.18)$$

and that the probability $P_2(T)$ that the observer will receive radiation from both magnetic poles is given by

$$P_2(T) = \frac{1}{2} [\psi_b(\pi/2)]^2 = 0.433 \, (R_*/R_Y) . \qquad (3.19)$$

Hence we find that the probability that an observed pulsar will show an interpulse is given by

$$P_i = P_2/P_1 = 0.23\ (R_*/R_Y)^{1/2} \ . \qquad (3.20)$$

One may now estimate the expected number of pulsars, of a given observed sample, which should show an interpulse by evaluating P_i for each pulsar and summing these values. When this is done for Sample A, considering η in the range $0.70 \geq \eta \geq 0.50$, we find that the number of pulsars expected to show interpulses is in the range 0.8 to 1.7. This is to be compared with the fact that four pulsars from Sample A (PSR 0532, 0904, 0950, and 1929) show interpulses. It may also be noted that three of these have short periods, consistent with the fact that $P_i \propto T^{-\eta/2}$.

VI. Discussion

We consider briefly some of the implications of the above results. If, for definiteness, we adopt $\eta = 0.6$ and $R_* = 10^{6.1}$ cm, we find that, for $T = 1$ sec., $R_Y = 10^{8.3}$ cm whereas $R_L = 10^{9.7}$ cm. Hence R_Y is very much smaller than R_L. These considerations therefore indicate a pulsar magnetospheric structure very different from that envisaged by Gold (1969), Goldreich and Julian (1969), and Gunn and Ostriker (1969).

For the Crab pulsar, $T = 10^{-1.5}$ sec., so $R_Y = 10^{7.4}$ cm and $R_L = 10^{8.2}$ cm. On noting that the power extracted from the star is $2\pi T^{-1} N$, and on equating this to the observationally indicated value of 10^{38} erg sec^{-1} (Shklovsky 1968), we find from equation (3.3) that $B_* = 10^{11.2}$ gauss, which is considerably less than the values (10^{12} - $10^{12.7}$ gauss) which have been previously estimated.

Scargle and Pacini (1971) have suggested that the "glitch" phenomenon may be caused by events occurring in pulsar magnetospheres. This

indicates a more complicated model of pulsar magnetospheres than has hitherto been contemplated. The results of the present study point in the same direction. In the next chapter we discuss a model magnetosphere which explains both the period-pulse-width distribution and braking index, and also offers a more detailed explanation of the glitch phenomenon in terms of magnetospheric behavior.

TABLE 3.1

The 18 pulsars making up Sample B, with their periods (T) and our judgements of the total pulse width (W). Those marked in the last column (G and O) make up the sample of 13 well determined pulse widths used by Gunn and Ostriker (1970).

SAMPLE B

Pulsar	T(sec)	W(sec)	G & O
PSR 0329	0.7145	.050	x
NP 0527	3.7455	.090	x
NP 0532	0.0331	.006	x
PSR 0628	1.2444	.140	
MP 0736	0.3749	.034	
CP 0808	1.2922	.070	x
PSR 0833	0.0892	.004	x
CP 0834	1.2738	.050	x
CP 0950	0.2531	.030	x
PSR 1133	1.1879	.050	x
AP 1237	1.3824	.060	
PSR 1508	0.7397	.030	x
PSR 1749	0.5626	.020	x
PSR 1919	1.3373	.040	x
PSR 1929	0.2265	.016	
PSR 2016	0.5580	.028	x
PSR 2045	1.9616	.100	x
AP 2303	1.5759	.030	

FIGURE CAPTIONS

Figure 3.1. Distribution of Sample A of pulsars in the variable y, $y = T^{2-\eta} W^{-2}$, compared with histograms generated from the theoretical curve (broken line), for various values of the parameter η. The best fit occurs for η in the range $0.60 \leq \eta \leq 0.70$. The curves clearly do not fit for the value $\eta = 1$.

Figure 3.2. Distribution of Sample B of pulsars in the variable y, $y = T^{2-\eta} W^{-2}$, compared with histograms generated from the theoretical curve (broken line), for various values of the parameter η. The best fit occurs for η in the range $0.50 \leq \eta \leq 0.60$.

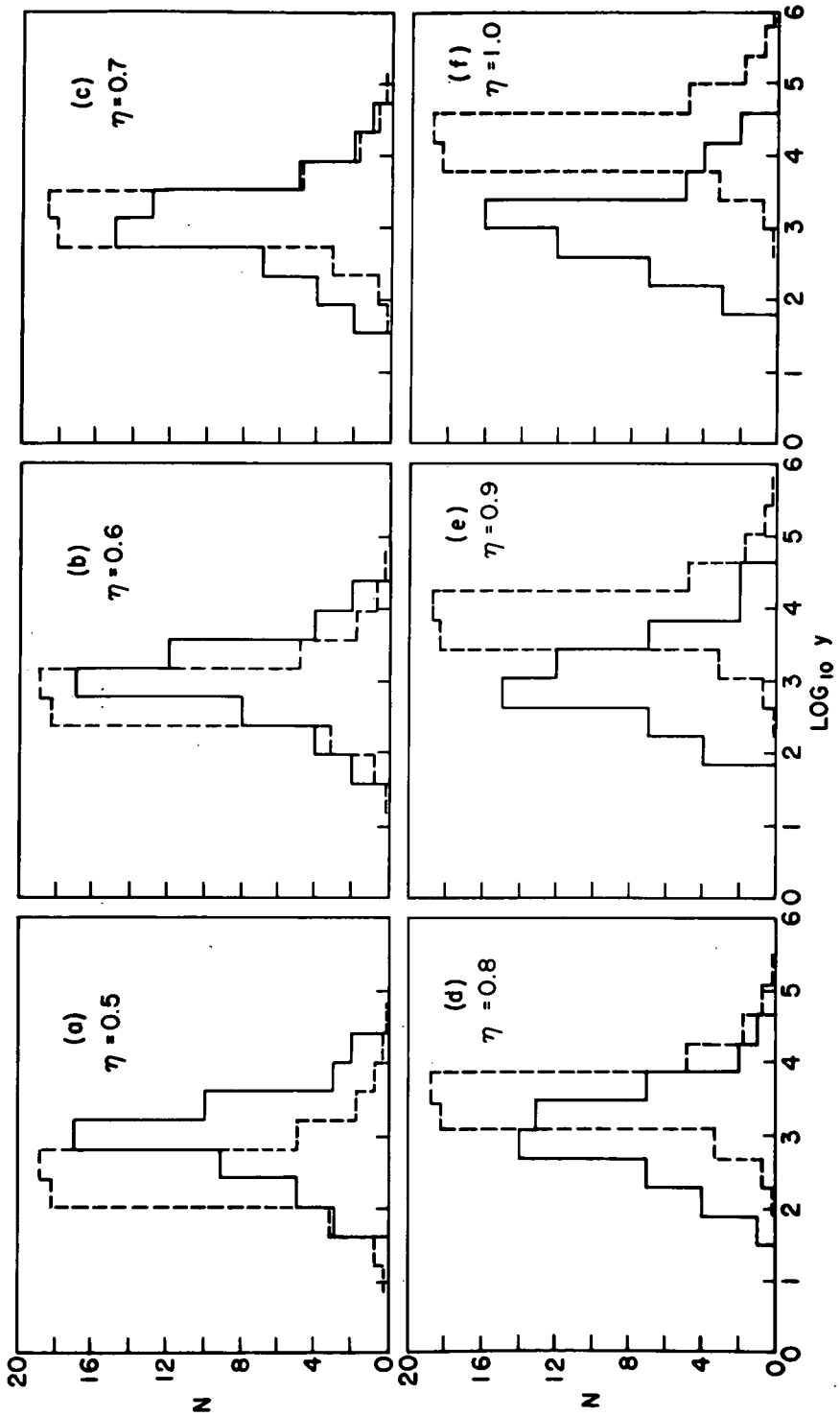

Figure 3.1

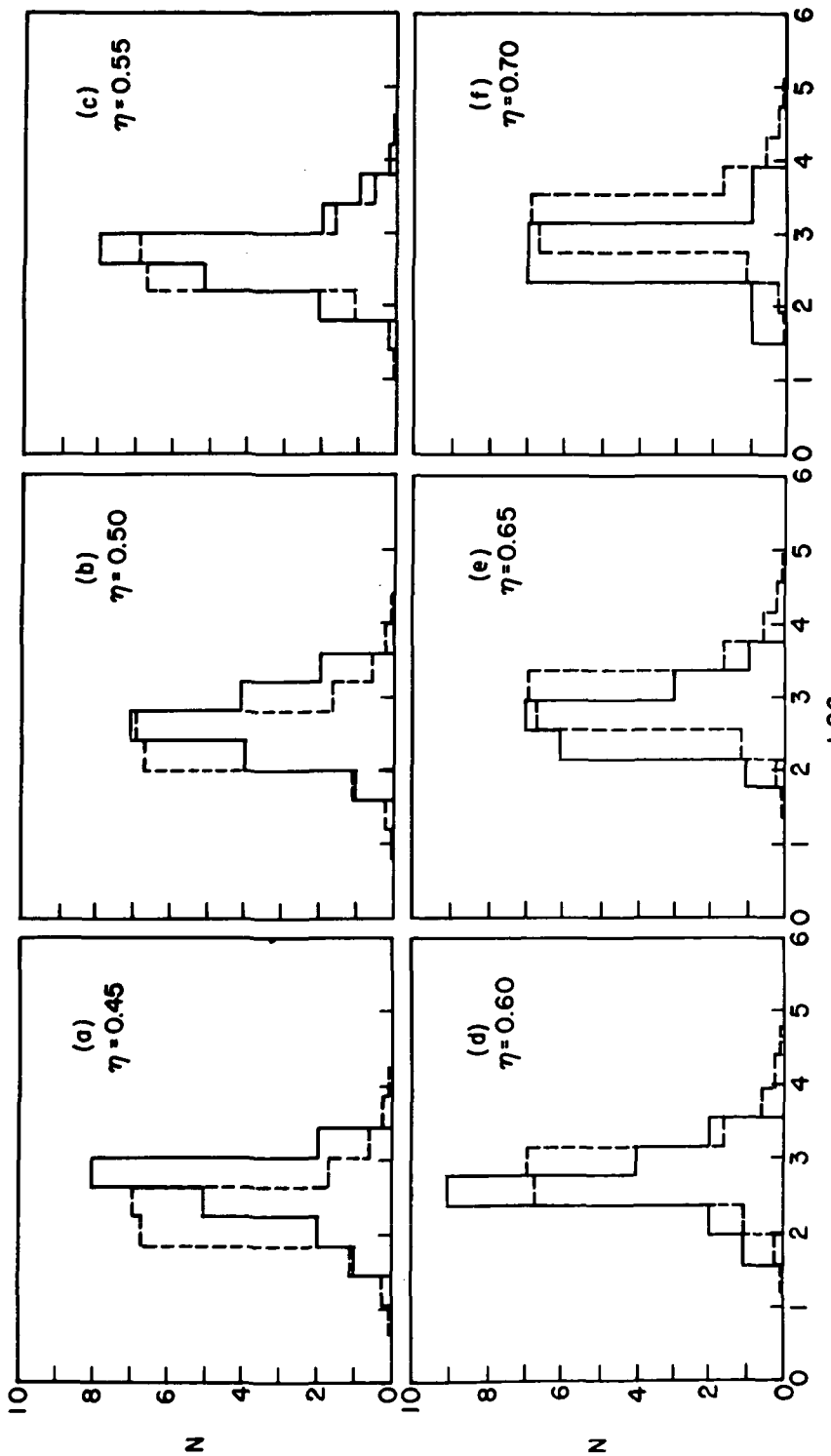

Figure 3.2

Chapter 4

THE EFFECTS OF NON-RELATIVISTIC GAS IN THE MAGNETOSPHERE

I. Introduction

In most models of pulsar magnetospheres (Gold 1969; Goldreich and Julian 1969; Michel 1969; Ostriker and Gunn 1969; Gunn and Ostriker 1970), it is assumed implicitly or explicitly that magnetic field lines contained within the "light cylinder" are closed whereas those which penetrate the light cylinder are open. If the radiation from pulsars originates at the magnetic polar caps (those areas at the neutron-star surface penetrated by open field lines) and is beamed along the magnetic-field lines at these locations (Radhakrishnan and Cooke 1969; Komasaroff 1970; Sturrock 1970, 1971a) there is a discrepancy between the inferred period-pulse-width distribution and the distribution derived from observation (Gunn and Ostriker 1970; see Chapter 3). This is illustrated, for Sample B of Chapter 3, in Figure 4.1; the expected distribution for $R_Y = R_L$ is shown as curve 1.

There is also a discrepancy concerning the braking index n ($n = \omega\ddot{\omega}/\dot{\omega}^2$): if the braking is due primarily to magnetic stresses, these models give $n = 3$; if the braking is due to a relativistic stellar wind, $n = 1$ (Michel 1969). There is a great deal of scatter in the value of n derived from timing measurements of the Crab pulsar, but it is generally agreed that $n > 1$ always and $n < 3$ almost always; Boynton et al. (1972) have found that $n = 2.4 \pm 0.2$, and Rankin, Campbell, and Counselman (1971) have found that $n \approx 2.3$ during quiet periods.

II. Non-Relativistic Gas in Pulsar Magnetospheres

The possibility that pulsar magnetospheres may contain substantial amounts of non-relativistic gas ($\sim 10^{24}$ g) was proposed by Scargle and

Pacini (1971). They introduced this hypothesis as an explanation of "glitches" (sudden changes in the periods of the Crab and the Vela pulsars) which, unlike the explanation in terms of "starquakes" (Ruderman 1969, 1972) would enable one to understand changes in the dispersion of the Crab radio pulses (Rankin and Roberts 1971) and in the optical appearance of the wisps in the Crab nebula (Scargle and Harlan 1970) which appear to be related to the September 1969 glitch in the Crab pulsar. The presence of a large amount of gas in pulsar magnetospheres, and fluctuations in this configuration, would offer an explanation of the prevalent "noise" in the residuals of timing data for the Crab pulsar (Boynton et al. 1972).

The presence of such a large amount of cool gas in a pulsar magnetosphere implies that gas is evaporated from the neutron star surface, presumably by heating due to bombardment of the surface by high-energy particles. However, such a large mass of gas cannot be supported against gravity or contained against centrifugal force by the magnetic field. Hence appreciable mass accumulation can occur only in the region where these two forces are in approximate equilibrium, that is, at the "force-balance" radius R_{FB} where $\omega^2 R_{FB} = GM_* R_{FB}^{-2}$. Gas cannot collect at a radius appreciably less than R_{FB}. If it collects at a radius appreciably greater than R_{FB}, centrifugal force will eventually fling out the collected gas, thereby opening the magnetic field lines to form two open flux tubes separated by a current sheet. This leads to the conclusion that $R_Y \approx R_{FB}$.

III. Braking Index

In this model $B \propto r^{-3}$ for $R_* \leq r \leq R_{FB}$, whereas approximately $B \propto r^{-2}$ for $R_{FB} \leq r \leq R_L$, so that the magnetic field strength at the light cylinder is given approximately by

$$B_L = B_* R_*^3 R_{FB}^{-1} R_L^{-2} , \qquad (4.1)$$

where B_* is the magnetic field strength at the surface of the star. In previous calculations of the magnetic torque exerted on a pulsar, it has been assumed that the toroidal and radial components of the magnetic field are comparable at the light cylinder. It seems reasonable to retain this assumption in the revised model, since if relativistic gas is flowing substantially radially outward at the light cylinder, and is also moving along magnetic field lines, the spiral angle must be approximately 45^o at the light cylinder. (Similar arguments concerning the solar wind lead to the accepted formulas for the magnetic torque on the sun, except that R_L is replaced by the radius at which the solar wind speed is equal to the Alfvén speed (Dicke 1964; Weber and Davis 1967). Hence, using equation (2.6) of Sturrock (1971a),

$$N = \frac{1}{2} R_L^3 B_L^2 , \qquad (4.2)$$

one obtains the following expression for the magnetic torque:

$$N = 10^{-4.12} M_*^{-2/3} B_*^2 R_*^6 T^{-7/3} . \qquad (4.3)$$

Since $N \propto \omega^{7/3}$, we see that $n = 7/3$, in good agreement with the value $n \approx 2.4 \pm 0.2$ derived from analysis of timing data of the Crab pulsar (Boynton et al. 1972).

IV. Period-Pulse-Width Distribution

We may compute the period-pulse-width relation to be expected in the present model. The values should cluster about the relation $W/T = 2\psi_\ell/2\pi$, where $\psi_\ell = \frac{3}{2} (R_*/R_{FB})^{1/2}$. This leads to the relation

$$W \approx 10^{1.15} M_*^{-1/6} R_*^{1/2} T^{2/3} . \qquad (4.4)$$

This relation is shown as curve 2 in Figure 4.1, adopting $M_* = M_\odot$ and $R_* = 10^{6.1}$ cm. The overall agreement is good.

Following the lines of Chapter 3 and the generalization of Appendix B [with $\eta = 2/3$ and $R_o = (GM_*/4\pi^2)^{1/3}$], we may estimate the scatter to be expected in the period-pulse-width distribution due to random orientations of the line of sight and of the magnetic and rotation axes. The resulting theoretical distribution of pulsars in the variable $y = (T^{2/3}/W)^2$ is compared with the observationally determined distribution, for a range of neutron-star models (Cohen and Cameron 1971), in Figure 4.2. The agreement is good for neutron-star masses in the range $0.5\ M_\odot \leq M_* \leq M_\odot$.

V. Glitches

During active periods, the moment of inertia I (g cm^2) of the star plus magnetosphere will be varying. At all times, in addition to the magnetic torque, there may be a loss of angular momentum at a rate L (g cm^2 sec^{-2}) due to the escape of particles from the system. These effects lead to the following expression for n:

$$n - n_o = (n_o - 2) \frac{\omega}{\dot{\omega}} \frac{\dot{I}}{I} - \frac{\omega^2}{\dot{\omega}^2} \frac{\ddot{I}}{I} + \frac{1}{\dot{\omega} I} \left(n_o L - \omega \frac{dL}{d\omega} \right) , \qquad (4.5)$$

where $n_o = \frac{\omega}{N} \frac{dN}{d\omega} = \frac{7}{3}$. A glitch is now interpreted as an instability of the gas-magnetosphere configuration which leads to the ejection of some of the gas from the magnetosphere and/or the dumping of some of the gas to the surface of the star. There is therefore a change δI in the

moment of inertia and a change δH in the angular momentum of the star-magnetosphere configuration. This leads to a change in the angular velocity given by

$$\frac{\delta\omega}{\omega} = -\frac{\delta I}{I} + \frac{\delta H}{\omega I} \quad . \tag{4.6}$$

For the process envisaged, both δI and δH are negative, which allows $\delta\omega$ to be either positive or negative.

After a glitch, the moment of inertia will return slowly to its original value. If the rate of evaporation from the neutron-star surface is approximately constant, and if the rate of mass loss from the collected gas is proportional to the mass of gas, the moment of inertia of the magnetosphere will relax according to the law

$$\Delta I(t) = \Delta I[1 - e^{-t/\tau_G}] \quad . \tag{4.7}$$

Noting that immediately prior to a glitch the moment of inertia of the magnetosphere is ΔI, we find that (despite the fact that $\dot{\omega}\tau_G \gg \delta\omega$) the post-glitch angular velocity ω_{PG} may be related to the extrapolated "no-glitch" angular velocity ω_{NG} by

$$\frac{\omega_{PG}(t)}{\omega_{NG}(t)} = 1 + \frac{\delta H}{\omega I} + \frac{\Delta I}{I} e^{-t/\tau_G} \quad . \tag{4.8}$$

The post-glitch braking index n_{PG} is related to the steady braking index n_S by

$$n_{PG} - n_S = \frac{\omega^2}{\dot{\omega}^2} \frac{\Delta I}{I} \frac{1}{\tau_G^2} e^{-t/\tau_G} \quad . \tag{4.9}$$

Equations (4.8) and (4.9) are in fair agreement with the post-glitch behavior of the Crab and Vela pulsars.

The September 1969 glitch of the Crab pulsar comprised a sudden increase in rotation rate by three parts in 10^9. The subsequent relaxation of the angular frequency agrees approximately with equation (3.8) with $\delta H = 0$ and τ_G approximately two months (Roberts and Richards 1971; see especially Figure 2). The observed value of $\delta\dot{\omega}/\dot{\omega}$ ($10^{-4.3 \pm 0.1}$; Papaliolios, Carleton and Horowitz 1970) leads to a similar estimate for τ_G. Equation (4.9) gives an approximate representation of the behavior of the braking index which was close to 2 prior to the glitch, jumped to nearly 3 after the glitch, and subsequently decayed to ~ 2.5 in about six months (Roberts and Richards 1971; Table 1).

The change $\delta\omega/\omega \approx 10^{-8.5}$ requires the dumping of $10^{21.8}$ g of gas from the force-balance region to the neutron-star surface. The potential or kinetic energy of such a mass in orbit at the force-balance radius is of order $10^{40.3}$ erg, comparable with the energy required to produce the observed wisp disturbances (Scargle and Harlan 1970). The inferred post-glitch time scale of two months implies an evaporation rate of $10^{15.5}$ g sec^{-1} which requires a power of $10^{35.4}$ erg sec^{-1}, about 0.2% of the power developed in the Crab pulsar.

Preliminary calculations indicate that this model of a glitch is consistent with published data (Radhakrishnan and Manchester 1969; Reichley and Downs 1969, 1971) concerning glitches in the Vela pulsar, but more definite conclusions must await the publication of more detailed observational data.

VI. Period-Age Distribution and Magnetic Fields

The period-age distribution of pulsars (Sturrock 1971b) may be reconsidered in terms of the present model. The results are shown in Figure 4.3. It is seen that the "turn-off" condition associated with the cessation of pair-production in the electron polar zone is unchanged and in good agreement with observations. We still find that the Crab pulsar is the only one spinning rapidly enough for pair-production to occur at the ion polar zone, which offers an explanation of the fact that this is the only pulsar exhibiting a precursor. The most important change is that the present model leads to estimates of B_* smaller by a factor of 10 than those based on earlier models. This change goes some way towards resolving the discrepancy noted by Gunn (1971) concerning the relative magnetic field strengths of neutron stars and white dwarfs. For the Crab pulsar, we find $B_* \approx 10^{11.3}$ gauss, which is to be compared with earlier estimates of 10^{12} to $10^{12.6}$ gauss.

FIGURE CAPTIONS

Figure 4.1. Period-pulse-width distribution for Sample B of Chapter 3. Curves 1 and 2 are theoretical curves expected on the basis of the polar-cap model for $R_Y = R_L$ and $R_Y = R_{FB}$, respectively.

Figure 4.2. Distribution of Sample B (Chapter 3) of pulsars in the variable y, $y = [T^{2/3}/W]^2$, compared with histograms generated from theory (broken lines) for $R_Y = R_{FB}$ and various values of the neutron star mass (Cohen and Cameron 1971).

Figure 4.3. Distribution of pulsars in period and "age" $[\tau = T/(dT/dt)]$ compared with theory. ●, S-type pulse structure; △, C-type structure; □, D-type structure, in the notation of Taylor and Huguenin (1971).

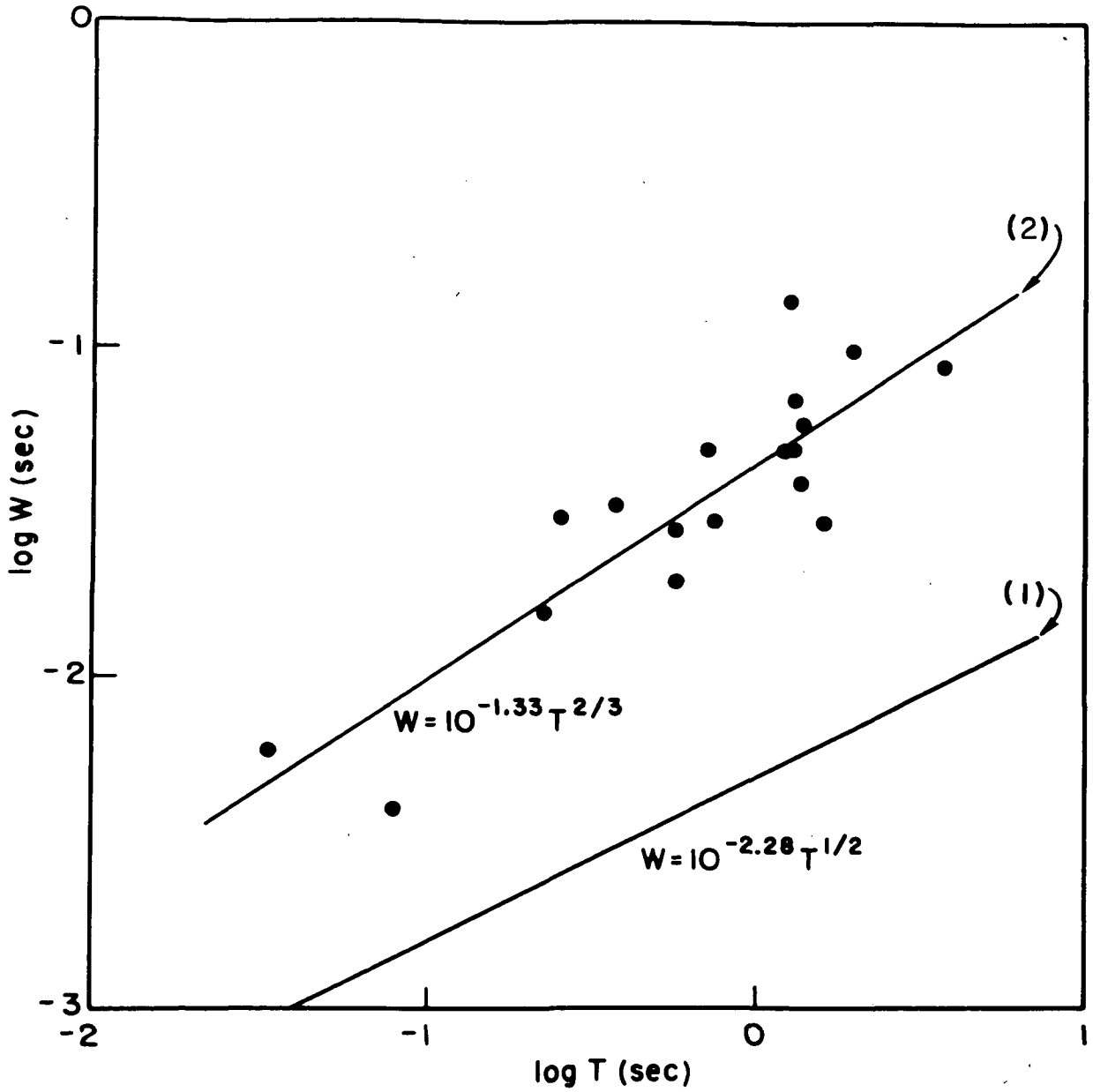

Figure 4.1

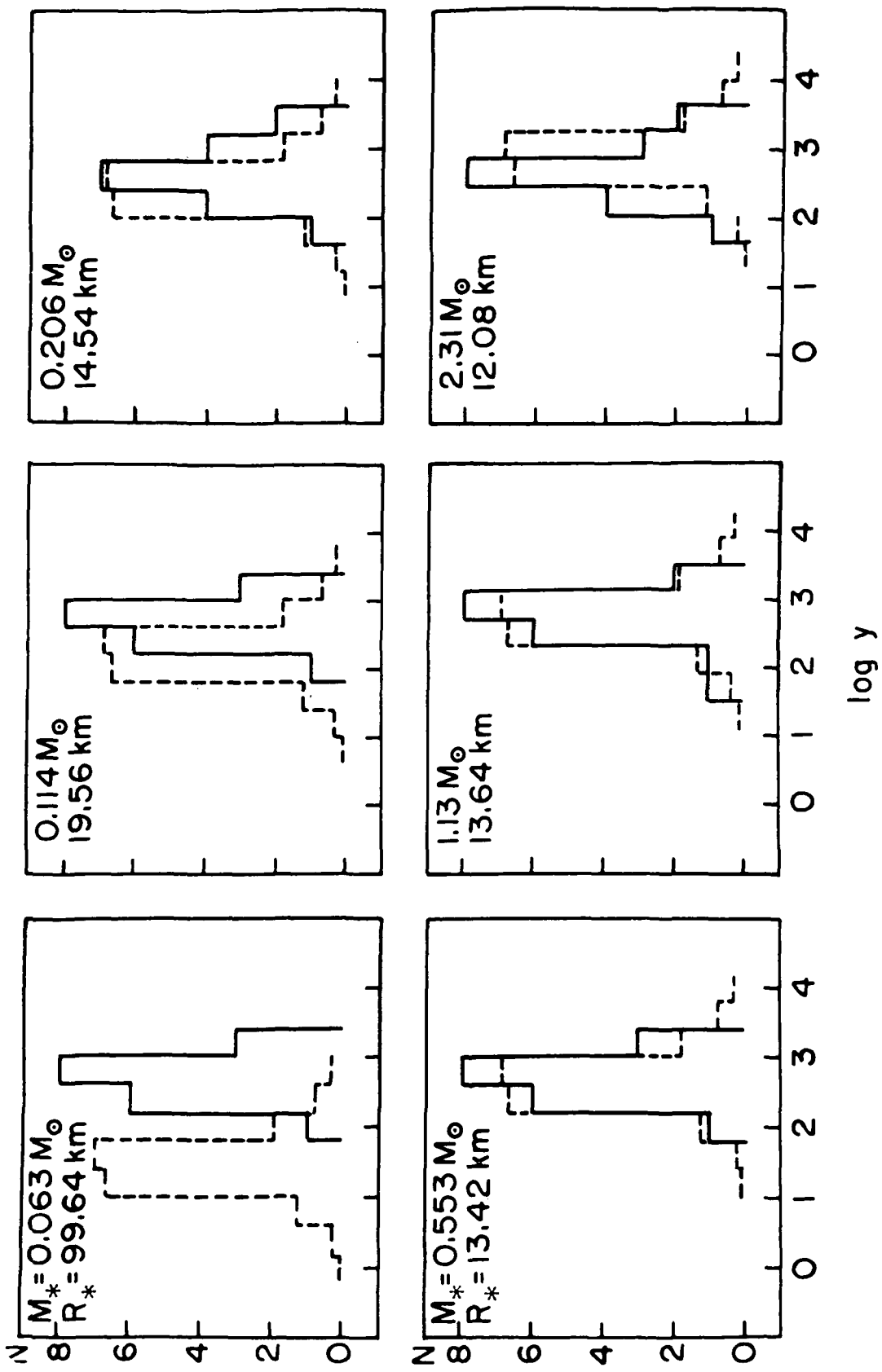
M*=0.063 M⊙
R*=99.64 km
0.114 M⊙
19.56 km
0.206 M⊙
14.54 km
M*=0.553 M⊙
R*=13.42 km
1.13 M⊙
13.64 km
2.31 M⊙
12.08 km
N
0
2
4
6
8
0
1
2
3
4
log y

Figure 4.2

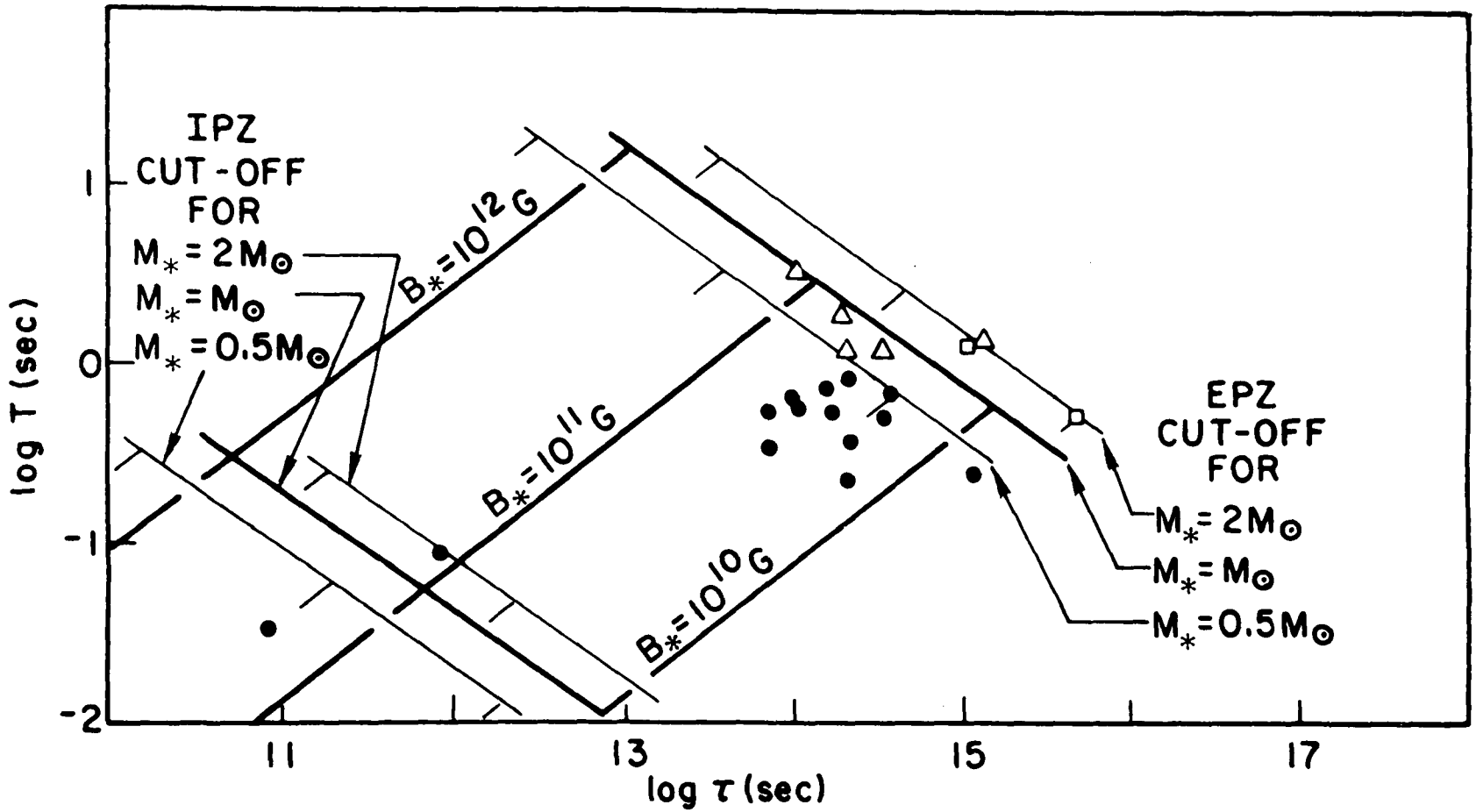
IPZ
CUT-OFF
FOR
M* = 2M⊙
M* = M⊙
M* = 0.5M⊙
B*=10^12 G
B*=10^11 G
B*=10^10 G
EPZ
CUT-OFF
FOR
M* = 2M⊙
M* = M⊙
M* = 0.5M⊙
log T (sec)
log τ (sec)
1
0
-1
-2
11
13
15
17

Figure 4.3

Chapter 5

DETAILED MODEL OF THE COLLECTION OF GAS

I. Introduction

A model of pulsars in which the inner magnetospheric structure is as discussed in Chapter 4 seems to resolve two major discrepancies between the properties of earlier models (for which $R_Y = R_L$) and observational data. It is therefore desirable to analyze this model in more detail. More complete knowledge of the magnetospheric structure would make it possible to improve the calculation of the theoretical period-pulse-width distribution and to estimate the current distribution in the polar caps which would then provide a basis for calculation of pulse shapes. Calculation of the dynamic properties of the magnetosphere would provide information which could be compared with irregularities in timing data such as the persistent "noise" and "glitches." We shall find that this model also suggests an explanation of the "drifting sub-pulse" phenomenon (Hewish 1970) which is a puzzling feature of pulsars.

If a pulsar magnetosphere is initially free of gas, so that R_Y is approximately R_L, and gas evaporates from the surface of the star due to the bombardment of the surface of the star by relativistic particles, we can determine the locations at which gas may initially collect. This is a question of microscopic stability, in which we may for simplicity consider a single particle constrained to move on a corotating magnetic field line under the influence of gravitational and centrifugal forces. This problem is set up in Section II. If there is a progressive accumulation of gas, there will at some stage be sufficient gas in the trapping zones that the configuration will become unstable. This question of

macroscopic stability is much more complex and will not be discussed in detail in this thesis. Instead, we discuss in simple physical terms the motion of collected gas in the limit that the mass becomes very large. These physical arguments show that matter collected substantially beyond the force-balance radius will be flung outward, opening the magnetic field lines to which it is tied.

In Sections III and IV, we discuss the aligned and orthogonal cases in detail. In each case, there are small collection zones which are both microscopically and macroscopically stable. By determining where macroscopic stability changes to instability, we determine the separatrix between closed and open field lines, and hence determine the sizes and shapes of the polar caps. With this information, it is possible to re-examine the period-pulse-width distribution and to compare it with observational data; this is done in Section V. The interpulse phenomenon is examined in Section VI, and further topics are discussed briefly in Section VII.

II. The Model

To investigate the trapping of gas and its effect on the structure of the magnetic field, we find the locus of stable points for single particles constrained to move along field lines. The magnetic field (surface strength B_*) is assumed to be dipolar from the neutron star to the light cylinder. Thus we have the problem of "a bead on a wire"; the bead is subject to gravity, and the wire rotates with a constant angular velocity. The stable points of the motion will tell us where cool gas will begin to collect in the magnetosphere.

In a uniformly rotating reference frame, the Lagrangian for a particle of mass m is given (Landau and Lifshitz 1960) by

$$L = \frac{1}{2} mv^2 + m\vec{v} \cdot \vec{\omega} \times \vec{r} + \frac{1}{2} m(\vec{\omega} \times \vec{r})^2 - U(\vec{r}) , \qquad (5.2.1)$$

where $U(\vec{r})$ is the potential energy of the particle in an inertial frame. The motion is one-dimensional so the term $m\vec{v} \cdot \vec{\omega} \times \vec{r}$ makes no contribution to the Euler-Lagrange equations and the particle moves with effective potential energy

$$V = - \frac{m}{2} (\vec{\omega} \times \vec{r})^2 - GM_* m/r . \qquad (5.2.2)$$

The potential energy $U(\vec{r})$ is the gravitational potential energy due to a spherically symmetric central body of mass M_*. To evaluate V, we define coordinates in the rotating frame such that the magnetic dipole axis is in the z-direction and the angular velocity vector is in the x-z plane with polar angle Θ. If (r,θ,ϕ) are the usual spherical polar coordinates,

$$V = - \frac{m}{2} \left\{ \omega^2 r^2 \left[\sin^2\theta \sin^2\phi + \left(\sin\theta \cos\phi \cos\Theta - \cos\theta \sin\Theta \right) \right]^2 \right\} - \frac{GM_* m}{r} . \qquad (5.2.3)$$

In dimensionless form, all lengths are scaled to the force-balance radius R_{FB}, all energies are given in terms of a typical energy E_o, and all forces in terms of a typical force F_o where

$$R_{FB} = (GM_* \omega^{-2})^{1/3} , \qquad (5.2.4)$$

$$E_o = m \omega^2 R_{FB}^2 , \qquad (5.2.5)$$

$$F_o = m \omega^2 R_{FB} . \qquad (5.2.6)$$

The dimensionless quantities are defined by

$$r = \alpha R_{FB} , \qquad r_o = \beta R_{FB} ; \tag{5.2.7}$$

$$V = \Psi E_o , \qquad E = \epsilon E_o ; \tag{5.2.8}$$

$$\vec{F} = \vec{f} F_o . \tag{5.2.9}$$

The resulting expression for the effective potential is

$$\Psi = - \frac{\alpha^2}{2} \left\{ \sin^2\theta \sin^2\phi + \left(\sin\theta \cos\phi \cos\Theta - \cos\theta \sin\Theta \right)^2 + 2\alpha^{-3} \right\} . \tag{5.2.10}$$

Furthermore, we may label a particle by the magnetic field line to which it is tied. A dipole field line is given by

$$\phi = \text{constant} , \qquad r^{-1} \sin^2\theta = r_o^{-1} , \tag{5.2.11}$$

where r_o is the greatest extent of the field line. In dimensionless form,

$$\phi = \text{constant} , \qquad \beta \sin^2\theta = \alpha , \tag{5.2.12}$$

so that (β,ϕ) identifies a field line and θ locates a particle along it. For a particle so labeled, Eq. (5.2.10) becomes

$$\Psi = - \frac{1}{2} \beta^2 \sin^4\theta \left\{ \sin^2\theta \sin^2\phi + \left(\sin\theta \cos\phi \cos\Theta - \cos\theta \sin\Theta \right)^2 + 2\beta^{-3} \sin^{-6}\theta \right\} . \tag{5.2.13}$$

The rate of change of Ψ along a field line is given by

$$d\Psi/ds = \hat{n} \cdot \vec{\nabla}\Psi , \tag{5.2.14}$$

where $\hat{n}$ is the unit vector parallel to the magnetic field:

$$\hat{n} = (1 + 3\cos^2\theta)^{-1/2}\,(2\cos\theta,\ \sin\theta,\ 0)\ . \qquad (5.2.15)$$

From Eq. (5.2.10),

$$R_{FB}\left(d\Psi/ds\right) = \alpha\left(1+3\cos^2\theta\right)^{-1/2}\Big\{-2\cos\theta\left[\sin^2\theta\sin^2\phi + \left(\sin\theta\cos\phi\cos\Theta - \cos\theta\sin\Theta\right)^2\right]$$
$$- \sin\theta\Big[\sin\theta\cos\theta\sin^2\phi + \left(\sin\theta\cos\phi\cos\Theta - \cos\theta\sin\Theta\right)$$
$$\times\left(\cos\theta\cos\phi\cos\Theta + \sin\theta\sin\Theta\right)\Big] + 2\cos\theta\,\alpha^{-3}\Big\}\ . \qquad (5.2.16)$$

Along a field line labeled by (β,ϕ), this is

$$R_{FB}\left(d\Psi/ds\right) = \beta\sin^2\theta\left(1+3\cos^2\theta\right)^{-1/2}\Big\{-2\cos\theta\left[\sin^2\theta\sin^2\phi + \left(\sin\theta\cos\phi\cos\Theta - \cos\theta\sin\Theta\right)^2\right]$$
$$- \sin\theta\Big[\sin\theta\cos\theta\sin^2\phi + \left(\sin\theta\cos\phi\cos\Theta - \cos\theta\sin\Theta\right)$$
$$\times\left(\cos\theta\cos\phi\cos\Theta + \sin\theta\sin\Theta\right)\Big] + 2\beta^{-3}\cos\theta\sin^{-6}\theta\Big\}\ . \qquad (5.2.17)$$

Another quantity of interest is the energy of a particle tied to a field line, as measured in an inertial frame (at rest with respect to the origin of the rotating frame). Neglecting the kinetic energy due to small velocities in the rotating frame,

$$E = \frac{m}{2}\,(\vec{\omega}\times\vec{r})^2 - GM_*m/r\ . \qquad (5.2.18)$$

In dimensionless form, this is

$$\epsilon = \frac{1}{2}\,\alpha^2\left[\sin^2\theta\sin\phi + \left(\sin\theta\cos\phi\cos\Theta - \cos\theta\sin\Theta\right)^2 - 2\alpha^{-3}\right]\ . \qquad (5.2.19)$$

Along a field line labeled by (β,ϕ),

$$\epsilon = \frac{1}{2}\,\beta^2\sin^4\theta\left[\sin^2\theta\sin^2\phi + \left(\sin\theta\cos\phi\cos\Theta - \cos\theta\sin\Theta\right)^2 - 2\beta^{-3}\sin^{-6}\theta\right]\ . \qquad (5.2.20)$$

Finally, we need the force on a particle in the rotating frame. From Eq. (5.2.2),

$$\vec{F} = -m\vec{\omega} \times (\vec{\omega} \times \vec{r}) - GM_* m\vec{r}/r^3 \ . \tag{5.2.21}$$

In dimensionless form, this has components

$$f_r = \alpha\left[\sin^2\theta\sin^2\phi + \left(\sin\theta\cos\phi\cos\Theta - \cos\theta\sin\Theta\right)^2 - \alpha^{-3}\right] , \tag{5.2.22a}$$

$$f_\theta = \alpha\left[\sin\theta\cos\theta\sin^2\phi + \left(\sin\theta\cos\phi\cos\Theta - \cos\theta\sin\Theta\right)\left(\cos\theta\cos\phi\cos\Theta + \sin\theta\sin\Theta\right)\right] , \tag{5.2.22b}$$

$$f_\phi = \alpha\left[\sin\theta\sin\phi\cos\phi - \sin\phi\cos\Theta\left(\sin\theta\cos\phi\cos\Theta - \cos\theta\sin\Theta\right)\right] . \tag{5.2.22c}$$

For a given field line, we may simply substitute according to Eq. (5.2.12). These results may be confirmed by differentiation of Eq. (5.2.10).

Considerable simplification of our work occurs because the two transformations

$$\phi \to 2\pi - \phi \tag{5.2.23}$$

and

$$\left.\begin{aligned} \phi &\to \pi - \phi \\ \theta &\to \pi - \theta \end{aligned}\right\} \tag{5.2.24}$$

leave Ψ unchanged (see Eq. [5.2.13]). Thus we need explicitly consider only the intervals $0 \le \theta \le \pi/2$ and $0 \le \phi \le \pi/2$. The following notation will be used throughout:

$$\chi = \sin^2\theta \ , \tag{5.2.25}$$

$$\eta = \cos^2\phi \ , \tag{5.2.26}$$

$$\lambda = \cos^2\Theta \ . \tag{5.2.27}$$

Note that a single value of the coordinate χ corresponds in general to two values of the coordinate θ in the complete range $0 \leq \theta \leq \pi$.

The requirement for microscopic equilibrium at a given point is

$$d\Psi/ds = 0 \ . \tag{5.2.28}$$

The condition for microscopic stability at that point is that, in addition,

$$d^2\Psi/ds^2 > 0 \ . \tag{5.2.29}$$

However, it is not necessary to use condition (5.2.29) to decide which equilibrium points are stable. Since $\Psi \to -\infty$ as $r \to 0$, there must be more than one solution of Eq. (5.2.28) if Eq. (5.2.29) is to hold. Specifically, for a given (β,ϕ), a stable point $\theta_s(\beta,\phi)$ is a solution of Eq. (5.2.28) which lies between two other solutions of this equation which correspond to values of Ψ greater than $\Psi(\theta_s)$.

This rule has a simple physical interpretation. On a field line which originates at low magnetic latitude, there is only one equilibrium point and this is an unstable point because the inward gravitational force dominates the centrifugal force. On magnetic field lines which originate at large magnetic latitudes, there are three equilibrium points: the outermost point is in a region where the outward centrifugal force dominates, so it is stable; the other two points are where the components of gravitational and centrifugal forces along the magnetic field cancel out, and each of these is an unstable point. Hence if one knows the number of equilibrium points on a given field line, one can immediately determine whether each point is stable or unstable. Application of these rules will

show that, for any alignment between the magnetic and rotation axes, stable collection points exist on field lines which extend out approximately to R_{FB} or beyond.

We now consider briefly the question of macroscopic stability, i.e., the stability of a mass sufficiently large that the concomitant dynamical and gravitational stresses are comparable with the magnetic stresses. A detailed treatment of this topic represents a complex problem of magnetohydrodynamics which must be deferred for further study. In discussing an onset of instability, one of the key questions is to determine whether the onset is explosive or non-explosive (Sturrock 1966). This involves knowledge of the non-linear processes involved, but the question may often be decided without making a complete non-linear dynamical analysis.

What happens as mass begins to accumulate at microscopically stable points? There are three regions we must consider:

(1) Material collects where the radial force is inward (and the energy E is negative). This can only occur inside and close to the force-balance radius. Were mass in these places decoupled from the magnetic field, it would orbit with angular velocity somewhat higher than that of corotation. This implies that, as mass builds up, it will stretch the magnetic field lines. The magnetic stress will enforce corotation of masses smaller than some critical value, but larger masses will cause the magnetic field to wind up progressively. Since this would lead to a progressive increase in the transverse pressure, the configuration is likely to become MHD unstable to an instability of the Rayleigh-Taylor type (Schmidt 1966). A competing instability, in this situation, would be the tearing-mode instability (Furth, Killeen and Rosenbluth 1963)

which would lead to field-line reconnection. The MHD instability is likely to be explosive and may cause some material to be ejected and some to be dumped to the surface of the star, but the resistive instability is probably non-explosive.

(2) Material collects where the radial force is outward but the energy is negative. This can only occur outside and close to the force-balance radius. This case is similar to Case (1) except that the magnetic field will tend to wind up in the opposite sense since material would tend to orbit with angular velocities lower than that of corotation.

(3) Material collects where the radial force is outward and the energy is positive. This is the case for all collection points beyond the force-balance radius, except for the small region of Case 2. As the mass builds up, it stretches the field lines outward as it attempts to enter an open orbit. The magnetic stress will enforce corotation of masses smaller than a critical value, but larger masses will enter open orbits, carrying the attached magnetic field lines with them. This leads to an open magnetic field configuration. The transition appears to have the character of an explosive instability.

The implication of the above considerations is as follows. If the magnetosphere is initially free of non-relativistic gas and evaporation occurs, gas will collect on field lines which extend to approximately R_{FB} or beyond. When a sufficiently large mass has accumulated, the magnetic field will be distorted. On field lines denoted by Case (3) there will be a change of configuration (possibly explosive), leading to the ejection of gas and the conversion of closed field lines into open field lines. On field lines denoted by Case (2) the change in configuration would not initially be a drastic one, although the accumulation of a

sufficiently large mass of gas might eventually lead to a disruption of the magnetic field, possibly converting closed field lines to open field lines. On the field lines denoted by Case (1) the initial change in configuration will not be drastic, although a sufficiently large mass may lead to a large distortion or disruption of the magnetic field configuration. It seems quite possible that both the glitches and the "noise" observed in the Crab pulsar (Boynton et al. 1972) are the result of processes such as the above occurring in the pulsar magnetosphere.

We also note the possibility that trapped material in the force-balance region may be coupled to magnetic-field lines which have become disconnected from the main magnetic-field pattern of the neutron star, due to differential rotation leading to field-line reconnection as mentioned above. If this occurs, and if the trapped material has an azimuthally nonuniform distribution, the magnetosphere will be subject to a perturbation drifting azimuthally with respect to the neutron star. Such a perturbation would produce an azimuthally drifting perturbation of the current distribution at the polar caps. Since the radio emission is due to these currents, the radiation would display a periodic modulation similar to the observed "drifting subpulse" phenomenon.

In what follows, we are concerned primarily with the separatrix between closed and open field lines. To this end, it is convenient to introduce the following criteria, corresponding to the inner and outer boundaries of Case 3:

Criterion 1. Radial force zero or outward.

Criterion 2. Energy zero or positive.

The preceding considerations indicate that Criterion 1 gives an inner limit to the separatrix, and Criterion 2 gives an outer limit. In analyzing the polar-cap configuration and the period-pulse-width distribution, we shall give results for both criteria, but it will be seen

that it makes little difference which one is adopted.

As a simple application of the preceding rules, we discuss briefly the useful case of a field line at $\phi = \pi/2$ or $\phi = 3\pi/2$ ($\eta = 0$), and show that there exist stable points for all Θ. In this case Eqs. (5.2.17), (5.2.20), and (5.2.22a) reduce to

$$R_{FB}(d\Psi/ds) = \beta\chi(4-3\chi)^{-1/2}(1-\chi)^{1/2}G(\chi) , \quad G(\chi) = -3\lambda\chi - 2(1-\lambda) + 2\beta^{-3}\chi^{-3} \tag{5.2.30}$$

$$\epsilon = \frac{1}{2}\beta^2\chi^2 H(\chi) , \quad H(\chi) = \lambda\chi + (1-\lambda) - 2\beta^{-3}\chi^{-3} \tag{5.2.31}$$

$$f_r = \beta\chi K(\chi) , \quad K(\chi) = \lambda\chi + (1-\lambda) - \beta^{-3}\chi^{-3} . \tag{5.2.32}$$

From the first equation it follows that $\chi = 1$ is an equilibrium point for all β and λ. It is a stable point if there is a single root of $G(\chi) = 0$ in the interval $0 < \chi < 1$. As

$$G'(\chi) = -3\lambda - 6\beta^{-3}\chi^{-4} , \tag{5.2.33}$$

there are no extrema of G in the interval. Thus there is only one root of $G(\chi) = 0$; this appears, initially at $\chi = 1$, when $G(1) \leq 0$. Therefore the point $(\chi = 1, \beta, \eta = 0)$ is a stable point if

$$\beta > \beta_s(\eta = 0,\lambda) = [2/(2+\lambda)]^{1/3} . \tag{5.2.34}$$

Next we consider the energy and radial force at these collection points. It is found that $\epsilon \geq 0$ if

$$\beta \geq \beta_e(\eta = 0,\lambda) = 2^{1/3} \approx 1.260 \tag{5.2.35}$$

and that $f_r \geq 0$ if

$$\beta \geq \beta_f(\eta = 0,\lambda) = 1 \ . \qquad (5.2.36)$$

Thus stable points occur at $\chi = 1$ whenever (5.2.34) is satisfied, the energy is zero or positive at these points when (5.2.35) holds, and the radial force is zero or outward if (5.2.36) is met. Hence we have demonstrated that stable collection is always possible for those field lines at $\phi = \pi/2$ and $\phi = 3\pi/2$, and that whichever criterion is adopted for the opening of field lines, it occurs at a distance which is independent of Θ. If criterion (1) is accepted, then, apart from the case $\Theta = \pi/2$, there is a region in which particles may collect and remain without opening the magnetic field pattern. If criterion (2) is adopted, such field lines exist for all Θ. For either criterion there is a much larger region in which material can collect stably and will drag open the magnetic field. It will become clear in the following sections that there is a finite range of ϕ around $\phi = \pi/2$ and around $\phi = 3\pi/2$ in which material can collect and be contained by the field.

III. The Aligned Case

For $\Theta = 0$, Eqs. (5.2.17), (5.2.20), and (5.2.22a) reduce to

$$R_{FB}d\Psi/ds = \beta\chi(4-3\chi)^{-1/2}(1-\chi)^{1/2}(-3\chi + 2\beta^{-3}\chi^{-3}) \qquad (5.3.1)$$

$$\epsilon = (1/2)\beta^2\chi^2(\chi - 2\beta^{-3}\chi^{-3}) \ , \qquad (5.3.2)$$

and

$$f_r = \beta\chi(\chi-\beta^{-3}\chi^{-3}) \ , \qquad (5.3.3)$$

respectively. From Eq. (5.3.1), $\chi = 1$ is an equilibrium point for all β (all ϕ are equivalent). The other root of $d\Psi/ds = 0$ on $0 < \chi < 1$

is

$$\chi = (2/3\ \beta^3)^{1/4} \tag{5.3.4}$$

and since $\chi < 1$, this exists only if

$$\beta > \beta_s(\Theta = 0) = (2/3)^{1/3} \approx 0.874\ . \tag{5.3.5}$$

From Eq. (5.3.2) the region of zero or positive energy for a given β is found to be

$$\chi \geq (2/\beta^3)^{1/4} \tag{5.3.6}$$

and only those field lines which satisfy

$$\beta \geq \beta_e(\Theta = 0) = 2^{1/3} \approx 1.260 \tag{5.3.7}$$

have such a section. The radial force is zero or positive for a given β if

$$\chi \geq \beta^{-3/4}\ . \tag{5.3.8}$$

Only field lines with

$$\beta \geq \beta_f(\Theta = 0) = 1 \tag{5.3.9}$$

can satisfy Eq. (5.3.8).

We have drawn this picture: All field lines outside of $\beta = 0.874$ have microscopically stable points at $\chi = 1$ ($\theta = \pi/2$). The radial force is outward for those stable particles outside of $\beta = 1$, and the energy is positive for those outside of $\beta = 1.260$. Thus for either criterion for the opening of field lines there is a region of macroscopic stability. In Figure 5.1 we show the various regions of collection. Figure 5.2

is a comparison, approximately to scale, of the magnetospheric structure given by this model and that of Goldreich and Julian (1969).

It is useful to know the depth $D(\beta)E_o$ of the effective potential wells around collection points. We find

$$\left.\begin{aligned} D(\beta) &= (1/2)\beta^2 + \beta^{-1} - (4/3)(3/2)^{1/4}\beta^{-1/4} , \quad \beta \geq \beta_s(\Theta = 0) \\ D(\beta) &= 0 , \quad \beta < \beta_s(\Theta = 0) . \end{aligned}\right\} \qquad (5.3.10)$$

$D(1.260) \approx 0.195$, so the potential well in the trapping region can be almost 20 percent of E_o. Since the work W required to lift a particle from the surface to the collection regions is approximately $W = GM_*m/R_* = (R_{FB}/R_*)E_o$, this depth is around 2 percent of W. However, one need only go as far out as $\beta \approx 5$ to reach $D(\beta)E_o \approx W$, a condition which makes collection of particles (and therefore opening of field lines) very likely.

IV. The Orthogonal Case

We now consider the case $\Theta = \pi/2$. There is substantial evidence, including the swing of the polarization vector during a pulse of the Vela and other pulsars (Radhakrishnan et al. 1969; Manchester 1971b) and the existence of interpulses for six pulsars (PSRS 0531, 0923, 0904, 0950, 1055, and 1929; Backer et al. 1973), that the dipole axis is highly inclined to the rotation axis for these pulsars. When $\Theta = \pi/2$, we have

$$R_{FB}d\Psi/ds = \beta\chi(1-\chi)^{1/2}(4-3\chi)^{-1/2}Q(\chi) , \qquad (5.4.1a)$$

$$Q(\chi) = 3\eta\chi - 2 + 2\beta^{-3}\chi^{-3} \; ; \qquad (5.4.1b)$$

$$\epsilon = \frac{1}{2}\,\beta^2\chi^2 R(\chi) \; , \qquad (5.4.2a)$$

$$R(\chi) = -\eta\chi + 1 - 2\beta^{-3}\chi^{-3} \; ; \qquad (5.4.2b)$$

$$f_r = \beta\chi S(\chi) \; , \qquad (5.4.3a)$$

$$S(\chi) = -\eta\chi + 1 - \beta^{-3}\chi^{-3} \; . \qquad (5.4.3b)$$

Inspection of Eq. (5.4.1a) shows that $\chi = 1$ is a zero of $d\Psi/ds$ for all azimuthal angles (characterized by η). Finding the other roots of $d\Psi/ds = 0$ is equivalent to solving

$$Q(\chi) = 0 \; , \qquad (5.4.4)$$

which, in turn, is equivalent to solving

$$\chi^3 Q(\chi) = 0 \; . \qquad (5.4.5)$$

Although Eq. (5.4.5) is quartic in χ and thus (in principle) soluble analytically, it is possible to obtain all the essential features of the solution without doing so. We only need decide which portions of (η,β)-space correspond to zero, one, and two roots of Eq. (5.4.4) in the range $0 < \chi < 1$. Note that $Q'(\chi)$ is zero in only one place, at

$$\chi_o = 2^{1/4}\,\beta^{-3/4}\,\eta^{-1/4} \; , \qquad (5.4.6)$$

and that $Q''(\chi)$ is always positive, so $Q(\chi_o)$ is the absolute minimum

of $Q(\chi)$. If $Q(\chi_o)$ is negative there are two real roots of Eq. (5.4.4); we must discover how many, if any, of these lie in the desired interval. This may be done and the result is Figure 5.3a, which shows the division of (η,β)-space we sought.

We have found the following: <u>For any η there is a β sufficiently large that there exists a microscopically stable point χ_s at that azimuth</u>. When $\eta < 1/2$, the stable point is $\chi_s = 1$; this requires a field line with $\beta > [2/(2-3\eta)]^{1/3}$. For $\eta > 2/3$, the stable point occurs at $\chi_s < 1$; here we need $\beta > 2^{5/3}\eta$. If $1/2 < \eta < 2/3$, there is initially $(\beta > 2^{5/3}\eta)$ a stable point at some $\chi_s < 1$; as β increases the stable point moves toward $\chi_s = 1$, and reaches $\chi_s = 1$ when $\beta \geq [2/(2-3\eta)]^{1/3}$. [When a stable point occurs at $\chi_s < 1$, there are physically two stable points, one at $\theta = \arcsin(\chi_s^{1/2})$, and the other at $\theta = \pi - \arcsin(\chi_s^{1/2})$.]

Next we investigate the energy and radial force. From Eqs. (5.4.2a) and (5.4.3a) it follows that the sign of ϵ is determined by the sign of $R(\chi)$, the sign of f_r by the sign of $S(\chi)$. The procedures outlined above, applied to R and S, enable us to construct Figures 5.3b and 5.3c, which show the signs of these quantities in various regions of (η,β)-space.

Comparison of Figure 5.3a with Figures 5.3b and 5.3c is sufficient to determine the character of the stable points $(\chi_s = 1)$ for $\eta < 1/2$. Figure 5.3c shows that $f_r > 0$ for all η. Figure 5.3b shows that if $\beta < [2/(1-\eta)]^{1/3}$ the energy is negative at the collection points. We also find that, for $1/2 < \eta < 2/3$, the stable points which occur at $\chi_s = 1$ always have $\epsilon > 0$ and $f_r > 0$.

For $\eta > 1/2$ these results are not sufficient to determine the signs of ϵ and f_r for those stable points located at $\chi_s < 1$. In order to do so we require more detailed knowledge of the roots of $Q(\chi)$, $R(\chi)$, and $S(\chi)$. The asymptotic form of the larger and smaller roots may be found by considering the limits $\beta \to \infty$ and $\chi \to 0$, respectively. In an obvious notation,

$$\chi_Q^+ \to (2/3)(1/\eta) , \tag{5.4.7a}$$

$$\chi_Q^- \to (1/\beta) ; \tag{5.4.7b}$$

$$\chi_R^+ \to (1/\eta) , \tag{5.4.8a}$$

$$\chi_R^- \to 2^{1/3}(1/\beta) ; \tag{5.4.8b}$$

$$\chi_S^+ \to (1/\eta) , \tag{5.4.9a}$$

$$\chi_S^- \to (1/\beta) . \tag{5.4.9b}$$

The smallest possible real zero of $Q(\chi)$ is χ_o, subject to $Q(\chi_o) = 0$; this is

$$\chi_Q^{(1)} = 2^{2/3}(1/\beta) = (1/2)(1/\eta) . \tag{5.4.10}$$

Similarly, the smallest real zeros of R and S are

$$\chi_R^{(1)} = 2(1/\beta) = (3/4)(1/\eta) \tag{5.4.11}$$

and

$$\chi_S^{(1)} = 2^{2/3}(1/\beta) = (3/4)(1/\eta) . \tag{5.4.12}$$

In addition, it may be verified that $\chi = \chi_Q^{(1)}$ is a root of $R(\chi) = 0$, and that it lies on the branch of smaller roots.

From these facts it follows that for all η, the region $f_r \geq 0$ completely contains the region $\epsilon \geq 0$, and, furthermore, it contains the entire locus of stable points. In addition, only for $\eta < 1/2$ do stable points occur where $\epsilon < 0$. These features are illustrated in Figure 5.4; numerical solutions for the zeros of Q, R, and S have been used to draw the curves.

In the orthogonal case there are microscopically stable points at all azimuths. At none of these is the radial force inward. Stable particles (at $\theta = \pi/2$) in the intervals $\pi/4 \leq \phi \leq 3\pi/4$ and $5\pi/4 \leq \phi \leq 7\pi/4$ have negative energy if they are inside $\alpha = \beta = [2/(2-3\cos^2\phi)]^{1/3}$, and will be macroscopically stable if Criterion 2 determines the opening of field lines. Collection of substantial amounts of material at all other microscopically stable points will lead to an open magnetic field pattern beyond those points.

V. Polar Caps and Period-Pulse-Width Distribution

The polar caps are those areas at the magnetic poles which are bounded by the intersections of the outermost closed field lines with the surface of the neutron star. The symmetry of Ψ under the transformations of Eqs. (5.2.27) implies that the outermost closed field lines, $\beta_c(\phi)$, obey

$$\beta_c(\phi) = \beta_c(2\pi-\phi) \tag{5.5.1}$$

and

$$\beta_c(\phi) = \beta_c(\pi-\phi) \ . \qquad (5.5.2)$$

This means that the shape of a cap is unchanged under rotations of 180^o about the projections of the x- and y-axes onto the planes $z = R_*$ and $z = -R_*$.

If radiation is produced near the neutron star surface and is beamed along open field lines, the half-angle of the emission cone is approximately

$$\psi(\phi) = (3/2)\theta_r(\phi) \qquad (5.5.3)$$

where

$$\theta_r(\phi) \approx \sin\theta_r(\phi) = (R_*/R_{FB})^{1/2}\ \beta_c^{-1/2}(\phi) \ . \qquad (5.5.4)$$

Since we will find that the polar caps and emission cones are roughly elliptical, we will speak of their semi-major $(\phi = \pi/2,\ 3\pi/2)$ and semi-minor $(\phi = 0,\ \pi)$ axes.

In Chapter 4, it was assumed that the last closed field line at a given azimuth was the one which grazed a cylinder of radius R_{FB} centered on the rotation axis. This leads to semi-major axis $\psi_\ell = (3/2)(R_*/R_{FB})^{1/2}$ and semi-minor axis $\psi_b = \psi_\ell\, G(\Theta)$. The definition and properties of the function $G(\Theta)$ are given in Appendix A. We introduce a reduced measure of the angular size of polar caps and emission cones,

$$\kappa(\phi) = \beta_c^{-1/2}(\phi) \ , \qquad (5.5.5)$$

so that the model of Chapter 4 has $\kappa(\pi/2) = 1$ and $\kappa(0) = G(\Theta)$ (see Appendix A).

Choosing alternatively Criterion (1) or (2) for the opening of field lines, we find from the example in Section II that the semi-major axis is

$$\varkappa^{(1)}(\pi/2) = 1 \qquad (5.5.6a)$$

or

$$\varkappa^{(2)}(\pi/2) = (1/2)^{1/6} \approx 0.891 \ , \qquad (5.5.6b)$$

respectively. We have no general expression for the semi-minor axis, so we discuss the two special cases. The aligned case involves a circular polar cap, with the size given by Eqs. (5.5.6). In the orthogonal case we determine the shape of the polar cap as follows: If $\eta > 1/2$, collection always occurs with positive ϵ and f_r, so the first microscopically stable point determines the opening of field lines:

$$\beta_c(\phi) = 2^{5/3} \cos^2\phi \ , \quad \phi \le \pi/4 \ . \qquad (5.5.7)$$

For $\eta < 1/2$ the collection occurs at $\chi_s = 1$ with initially negative energy and positive radial force. Thus

$$\beta_c^{(1)} = [2/(2-3\cos^2\phi)]^{1/3} \ , \quad \phi \ge \pi/4 \ ; \qquad (5.5.8a)$$

$$\beta_c^{(2)} = 2^{1/3} \sin^{-2/3}\phi \ , \quad \phi \ge \pi/4 \ . \qquad (5.5.8b)$$

Therefore, in the orthogonal case, the polar cap has the shape

$$\varkappa(\phi) = (1/2)^{5/6}(1/\cos\phi) \ , \quad \phi \le \pi/4 \ ; \qquad (5.5.9a)$$

$$\varkappa^{(1)}(\phi) = (1/2)^{1/6}(2-3\cos^2\phi)^{1/6} \ , \quad \phi \ge \pi/4 \ ; \qquad (5.5.9b)$$

$$\varkappa^{(2)}(\phi) = (1/2)^{1/6} \sin^{1/3}\phi \ , \quad \phi \ge \pi/4 \ . \qquad (5.5.9c)$$

We illustrate in Figure 5.5 the shapes and relative sizes of the polar caps in the aligned and orthogonal cases. It is interesting to note that in the latter case the simplicity of the model has caused two sides

of the cap to be straight lines. Numerical examination of intermediate angles shows that the caps are close to elliptical. In Figure 5.6 we compare the function $G(\Theta)$ to the ratio $\nu(0)/\nu(\pi/2)$, including points derived for intermediate angles. The differences between $G(\Theta)$ and our results are sufficiently small ($\leq$ 10 percent) to be neglected. Thus we take over from Chapter 3 the theoretical distribution $f(y)$ of pulsars in the variable $y = (T^{2/3}/W)^2$. $f(y)$ peaks when $W/T = 2\psi_\ell/2\pi$ so

$$y_{peak}^{(1)} = (4\pi^2/9)(GM_*/4\pi^2)^{1/3}(1/R_*) \ , \qquad (5.5.10a)$$

$$y_{peak}^{(2)} = 2^{1/3}\, y_{peak}^{(1)} \ , \qquad (5.5.10b)$$

for Criteria (1) and (2), respectively. We have evaluated these quantities for a variety of neutron star models (Cohen and Cameron 1971; Baym, Pethic, and Sutherland 1971; Leung and Wang 1971; Clark et al. 1971); the results are presented in Figure 5.7.

The data in Table 5.1 have been taken from pulse profiles published by Manchester (1971b) and Lyne, Smith, and Graham (1971). We obtained the total width of the pulses by measuring the width at ten percent amplitude, and have included only those pulsars for which the noise at this level was small. In presenting the data, we employ "moving bins" (Turk 1972) to smooth out statistical fluctuations. In Figure 5.8, each data point represents the number of pulsars in a bin centered on that point. The spacing between points is smaller than the bin size, so that each pulsar is counted more than once (seven times in 5.8a and five times in 5.8b). The error bars are just the square root of the number in each bin. The data peak at log (y) = 2.95 ± 0.10. From Figure 5.7 it is clear that all of the

neutron star models cover this region. The best fit occurs for Curves 1 through 4; the models of Cohen and Cameron (based on an earlier "stiffer" equation of state) are less satisfactory. To account for a distribution of neutron star masses we fold together theoretical curves corresponding to a range of neutron-star masses. The smooth curves in Figure 5.8 give the results for uniform distributions of log y of half-width $\Delta \log(y) = 0$, 0.10, and 0.20 around $\log(y_{peak}) = 2.95$. The range of masses to which these correspond may be read off Figure 5.7, for the five distinct models of neutron-star structures.

VI. Interpulses

There are two tests of this model concerning those pulsars with interpulses. First, following the procedure outlined in Chapter 3 and the results of Appendix D, we may calculate the number of pulsars expected to show interpulses by summing $P_i = P_2/P_1$ over the 89 known pulsars (Terzian 1973). Putting $R_Y = \beta R_{FB}$,

$$P_i = 6.79\, \beta^{-1/2}\, R_*^{1/2}\, M_*^{-1/6}\, T^{-1/3}\ ; \qquad (5.6.1)$$

the resulting sum of P_i depends on the neutron star model. Choosing those of Baym, Pethic and Sutherland (1971), the number of pulsars N_i expected to show interpulses lies between 1.6 ($M_* = 1.41\ M_\odot$) and 12.4 ($M_* = 0.0925\ M_\odot$) (taking $\beta = 1$). This is illustrated as a function of the neutron star mass in Figure 5.9, and is in reasonable agreement with the existence of six pulsars with interpulses.

The second test is a consequence of the fact that a pulsar showing two pulses must have $\Theta \approx 90^\circ$, and thus the pulse width will satisfy $W/T \leq 2\Psi_\ell/2\pi$. In other words, these pulsars must have $y \geq y_{peak}$. For

pulsars 0531+21, 0823+26, 0950+08, and 1929+10, comparison of Figure 5.7 and Table 5.1 shows that there are neutron star masses for which this condition is met. We have no reliable pulse width for PSR 0904+77 nor PSR 1055-21, which have periods 1.579 s and 0.1971s, respectively. For neutron star masses between 0.0925 $M_\odot$ and 1.41 $M_\odot$, our model predicts pulse widths less than (320 msec - 43 msec) and (81 msec - 11 msec), respectively. [Terzian (1973) lists upper limits of 80 msec and 30 msec for the fifty percent widths of PSR 0904+77 and PSR 1055-21; these translate into widths at ten percent of peak of about 140 msec and 54 msec, respectively, in agreement with our estimates.]

VII. Discussion

Although we have used the idealized model of dipole field lines and single particle motion to study the collection of non-relativistic gas in pulsar magnetospheres, it appears that the results are substantially independent of these assumptions. Material is trapped stably when the magnetic field line along which it moves cuts the surfaces of constant potential energy in such a way that there exists a point at lower potential than neighboring points in either direction. As distance from the neutron star increases beyond R_{FB}, the equipotentials approach cylinders aligned with the rotation axis. Any closed field line which extends to this distance will have such points, regardless of its detailed shape. It appears that, for almost any field configuration, the field will trap gas starting somewhere near $r = R_{FB}$, and the field will be opened shortly beyond that radius. The magnetic torque on the neutron star will thus be that calculated in Chapter 4, with a braking index of $n = 7/3$.

The assumption of single-particle motion is good provided the term $(\rho/m)\ \nabla V$ in the equation of motion dominates the term $\nabla_{\parallel} p$, where p is the pressure. If $d = x\ R_{FB}$ is the characteristic size of a collection region and $|\nabla V| = y\ F_o$, this requires

$$\omega^2 R_{FB}^{\ 2} xy \gg kT_{\parallel}/m \ . \tag{5.7.1}$$

For parameters of the Crab pulsar, Eq. (5.7.1) implies that the model is acceptable if

$$T_{\parallel} \ll 10^{10.9}\ (m/m_p)\ xy \ . \tag{5.7.2}$$

Reasonable values for x and y are 0.1, so that we need $T \ll 10^{8.9}\ ^{o}K$. We believe that this is not a very restrictive requirement, and infer that gas collected around stable points will not be forced out of those regions by its own pressure.

We have also neglected the mirroring force

$$\frac{1}{2}\ v_{\perp}^{\ 2}\ B^{-1}\ \nabla_{\parallel} B \ . \tag{5.7.3}$$

This is much smaller than $|(\rho/m)\ \nabla V|$ if

$$kT_{\perp}/m \ll \omega^2 R_{FB}^{\ 2}\ xy \ , \tag{5.7.4}$$

the same criterion satisfied by the parallel temperature in Eq. (5.7.1).

Containment of gas also requires that diffusion of plasma across field lines is slow. From Spitzer (1962), the velocity of transverse diffusion is approximately

$$v_{\perp}^{\ D} = 10^{-2.7}\ \ln\Lambda\ B^{-2}\ T^{-1/2}\ \nabla_{\perp}(\rho/m) \ . \tag{5.7.5}$$

Taking the Coulomb logarithm $\ln\Lambda$ to be 5, the time scale for transverse diffusion is about

$$\tau_{\perp}^{D} = d/v_{\perp}^{D} = 10^{13.8}\, x^2 \approx 10^{11.8} \text{ sec} . \qquad (5.7.6)$$

Apparently, transverse diffusion is not a problem. However, since the rate of mass loss from collection regions determines the post-glitch relaxation time (see Chapter 4), more detailed study is needed of these and related processes.

From these discussions it seems that if there is a substantial amount of cool gas in pulsar magnetospheres, the mass and field configurations will be similar to those we have described.

TABLE CAPTION

Table (5.1). The 25 pulsars included in our sample. The ten percent widths measured from the papers of Manchester (1971b) ("RNM") and Lyne, Smith, and Graham (1971) ("LS&G") are listed under the radio frequencies (MHz) used for each observation. Widths which are underlined were judged the most reliable and those in parenthesis the least reliable. Our assessment of the "BEST" width takes this into consideration. The last two columns list the values of [W(sec)]/[T(sec)], and $\log_{10} y$, $y = (T^{2/3}/W)^2$.

Table 5.1

PULSAR	T(sec)	TEN PERCENT PULSE WIDTH (msec)							W/T	log y
		----RNM-----		-------L S & G-------						
		410	1665	151	240	408	610	"BEST"		
0329+54	0.7145	54	52		61	55	53	55	.077	2.32
0450-17	0.5498					26		26	.047	2.82
0525+21	3.7455						225	225	.060	2.06
0531+21	0.0331	(4.7)	1					1	.030	4.03
0628-28	1.2444						145	145	.117	1.80
0809+74	1.2922	86	(104)	110	95			90	.070	2.24
0818-13	1.2381					36		36	.029	3.01
0823+26	0.5307		12		17	15	16	16	.030	3.22
0833-45	0.0892		3.5					3.5	.039	3.51
0834+06	1.2738	32	(35)	33		33		33	.026	3.10
0950+08	0.2531	20	20	35	19	(31)	21	20	.079	2.60
1133+16	1.1879	40	33	48	43		38	40	.034	2.90
1237+25	1.3824	62	54	(68)	62	57		60	.043	2.63
1508+55	0.7397	27	(29)			26		26	.035	3.00
1604-03	0.4218					19		19	.045	2.94
1642-03	0.3877	6.5	(11)			8		7	.018	3.76
1706-16	0.6531	22				(24)		22	.034	3.07
1818-04	0.5981	22	(23)					22	.037	3.02
1911-04	0.8259	14	16			14		14	.017	3.60
1919+21	1.3373	45	(48)		41			43	.032	2.92
1929+10	0.2265	11	11			18		13	.057	2.91
1933+16	0.3587	13	8					12	.033	3.25
2016+28	0.5580	22	22			21		22	.039	2.98
2021+51	0.5292	29	22					25	.047	2.83
2045-16	1.9616	93	82		(93)	96		90	.046	2.48

FIGURE CAPTIONS

Figure 5.1. Structure of the magnetosphere in the aligned case. Entire shaded section--collection region with negative energy. Heavy shading--collection region with inward radial force. (a) Emission cone if Criterion 1 is adopted. (b) Emission cone for Criterion 2. (c) Emission cone if field lines are dipolar out to the light cylinder. (We have used Crab pulsar parameters in this figure.)

Figure 5.2. Left, the magnetosphere model of Goldreich and Julian (1969). Right, this model. The magnetic field configuration is schematic, but the scale (Crab pulsar parameters) is approximately correct, $R_L : R_{FB} : R_* \approx 100:10:1$.

Figure 5.3. Division of (η,β)-space according to (a) the number of zeros of $Q(\chi)$ in the interval $0 < \chi < 1$; (b) the sign of ϵ (clear area, negative everywhere; hatched area, positive around $\chi = 1$, becoming negative somewhere in the interval $0 < \chi < 1$; shaded area, negative around $\chi = 1$, becoming positive and then negative again somewhere in the interval $0 < \chi < 1$); (c) the sign of f_r (same notation as Figure 3b).

Figure 5.4. The roots χ of Q,R, and S, plotted versus β, for several values of η. Entire shaded region, positive radial force. Heavy shading, positive energy. The heavy curves are the stable points of single-particle motion. The features described in the text are illustrated here.

Figure 5.5. Polar caps, plotted as $r = \nu(\phi)$ versus ϕ. Broken lines, aligned case. Solid lines, orthogonal case. In both cases the larger polar cap corresponds to Criterion 1, the smaller one to Criterion 2.

Figure 5.6. Comparison of the function $G(\Theta)$ [smooth curve] with the ratio of minor to major axes derived in this model [open circles, Criterion 1; filled circles, Criterion 2].

Figure 5.7. The quantities $\log_{10}(y_{peak}^{(1)})$ and $\log_{10}(y_{peak}^{(2)})$ for several neutron star models: Curve 1, Leung and Wang (1971) [their curve 1]. Curve 2, Leung and Wang [their curve 2]. Curve 3, Baym, Pethic, and Sutherland (1971). Curve 4, Clark et al. (1971) [their table 5]. Curve 5, Cohen and Cameron (1971).

Figure 5.8. Comparison of the observed distribution of pulsars in the variable $y = (T^{2/3}/W)^2$ with the results of this model. See the text for an explanation of the symbols.

Figure 5.9. The number of pulsars (out of the presently known 89 pulsars) expected to show interpulses as a function of the neutron star mass, for the neutron star models of Baym, Pethic, and Sutherland (1971).

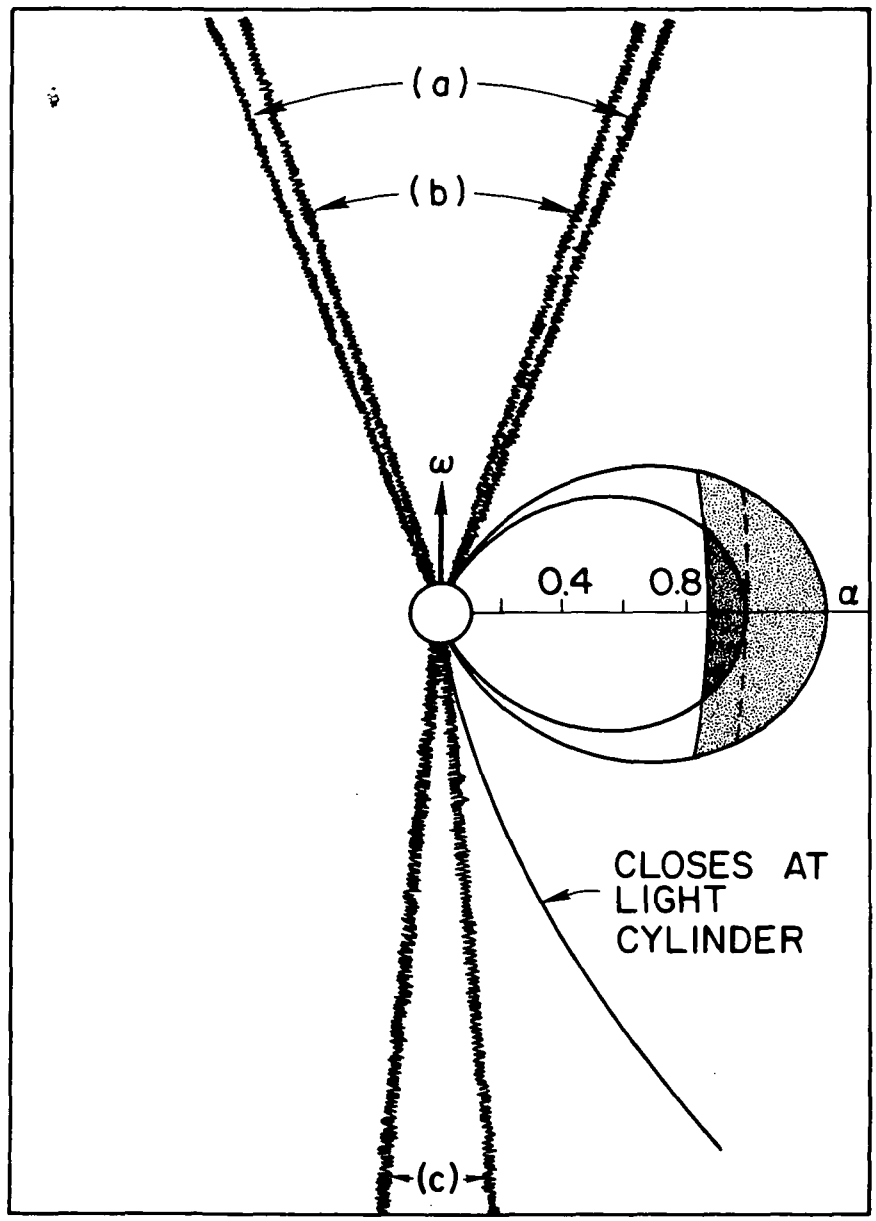

Figure 5.1

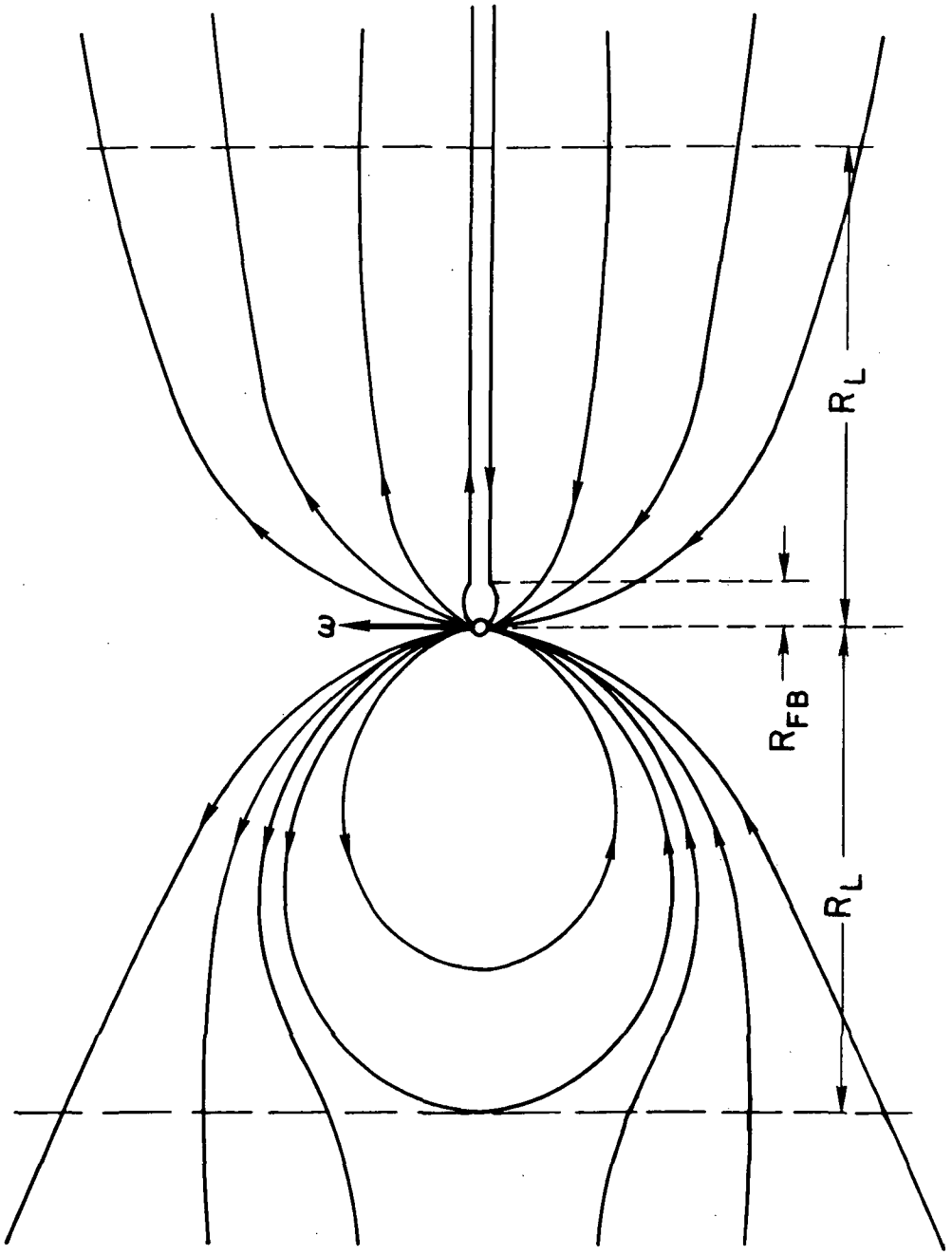

Figure 5.2

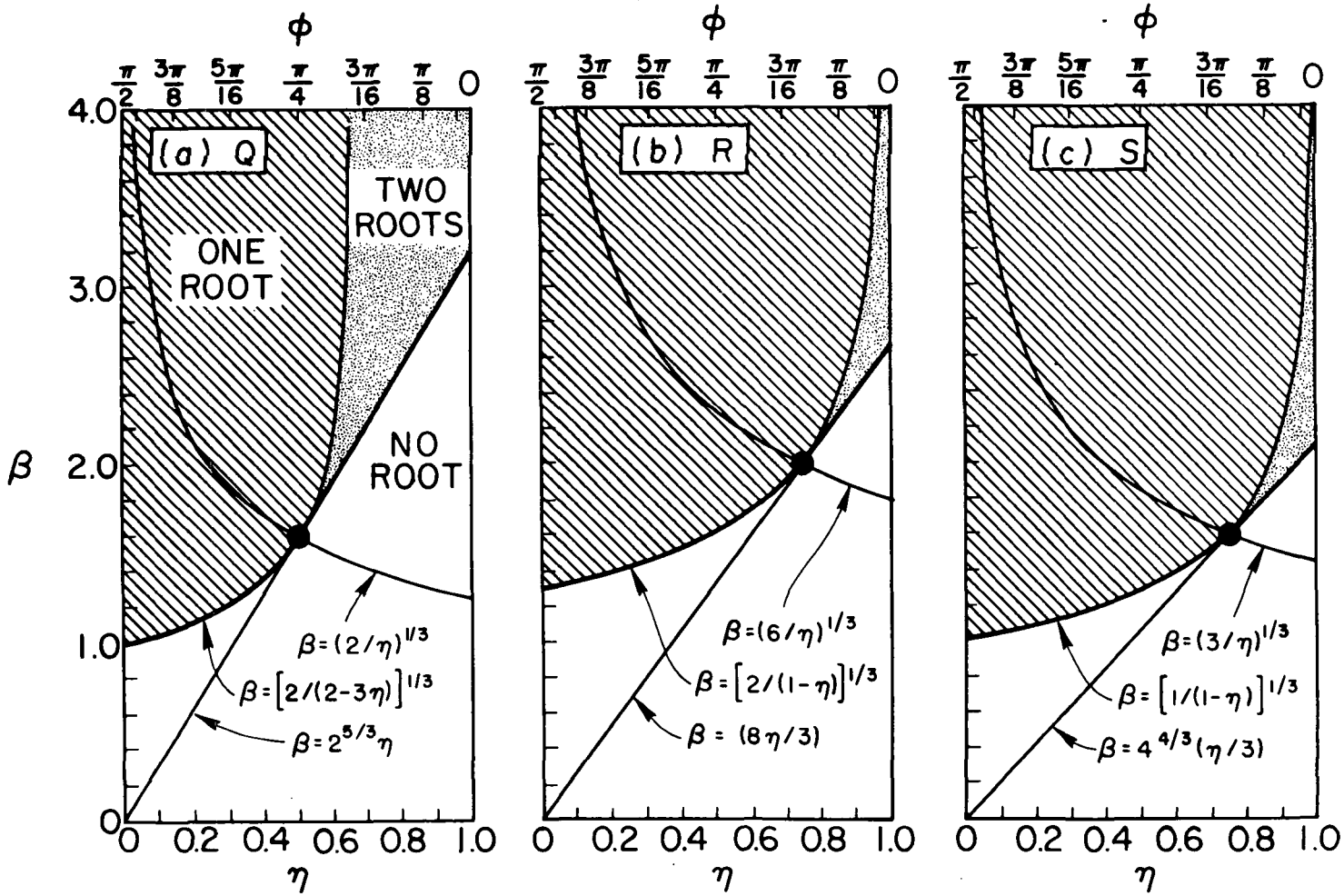
φ
π/2 3π/8 5π/16 π/4 3π/16 π/8 0
(a) Q
ONE ROOT
TWO ROOTS
NO ROOT
β=(2/η)^1/3
β=[2/(2-3η)]^1/3
β=2^5/3 η
(b) R
β=(6/η)^1/3
β=[2/(1-η)]^1/3
β=(8η/3)
(c) S
β=(3/η)^1/3
β=[1/(1-η)]^1/3
β=4^4/3 (η/3)
β
4.0
3.0
2.0
1.0
0
0 0.2 0.4 0.6 0.8 1.0
η

Figure 5.3

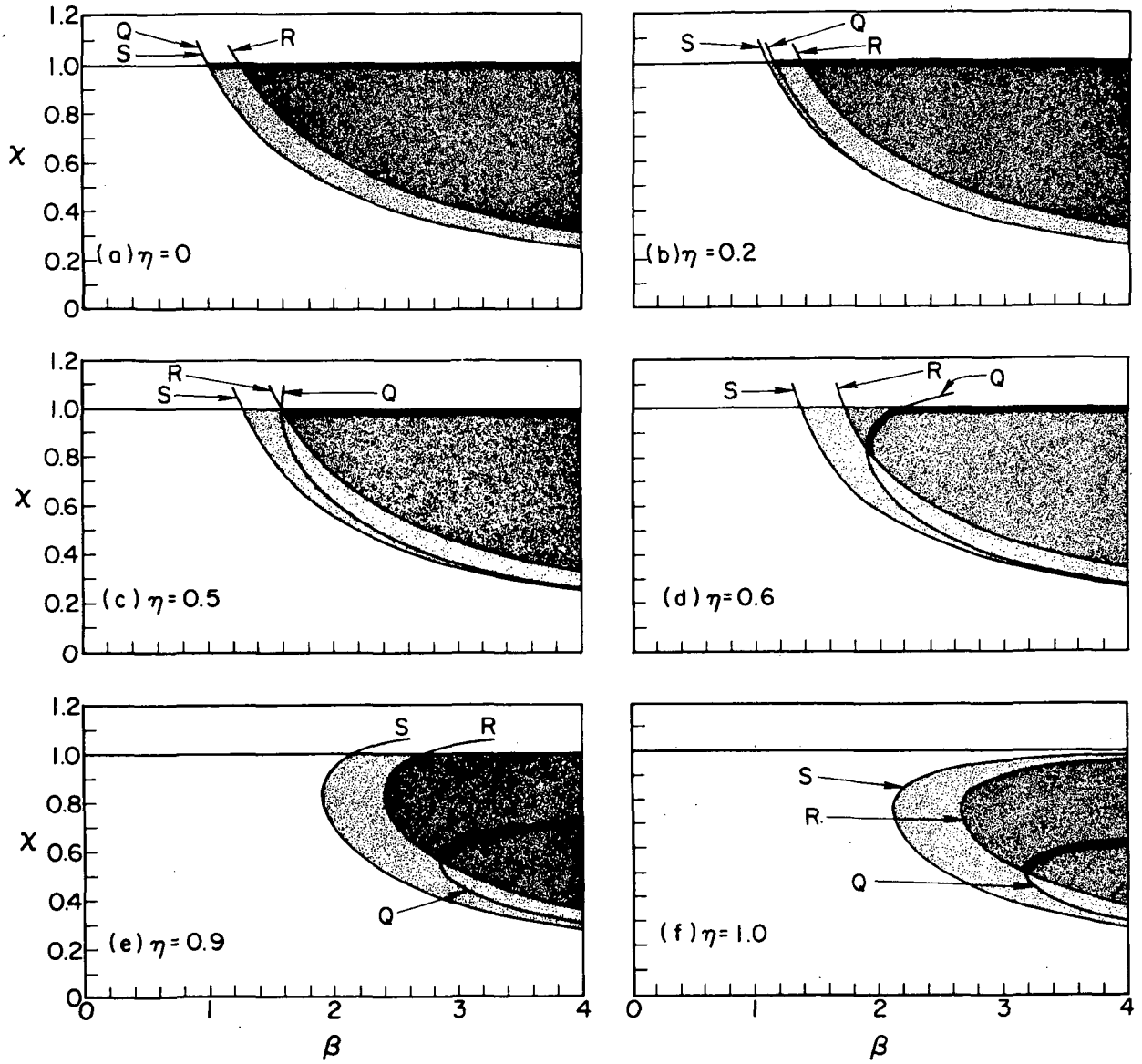

Figure 5.4

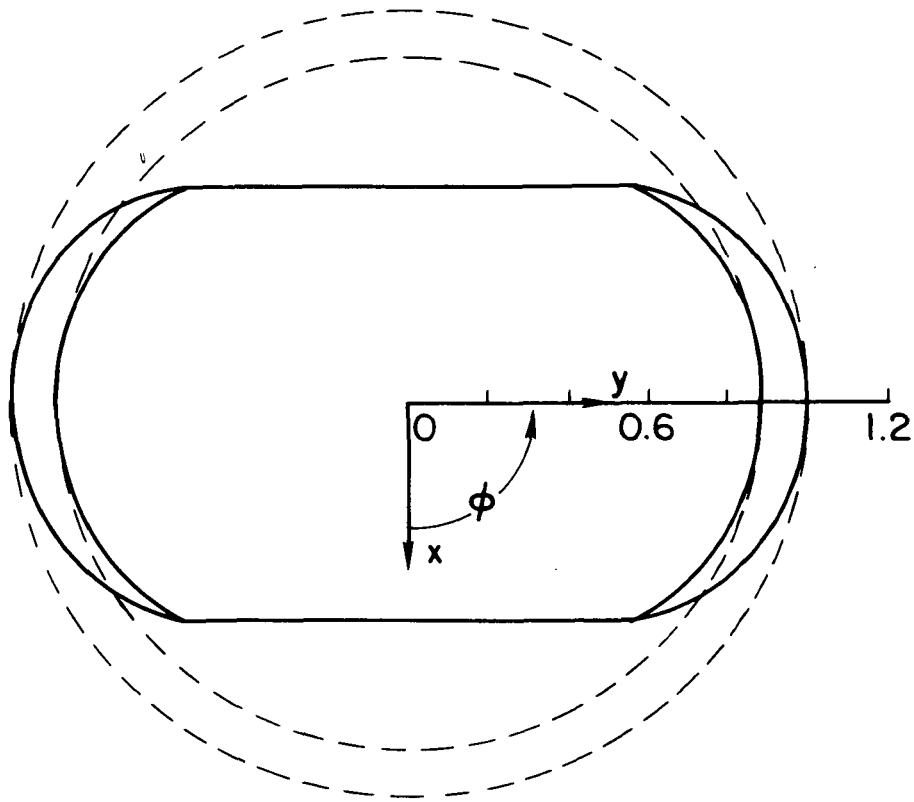

Figure 5.5

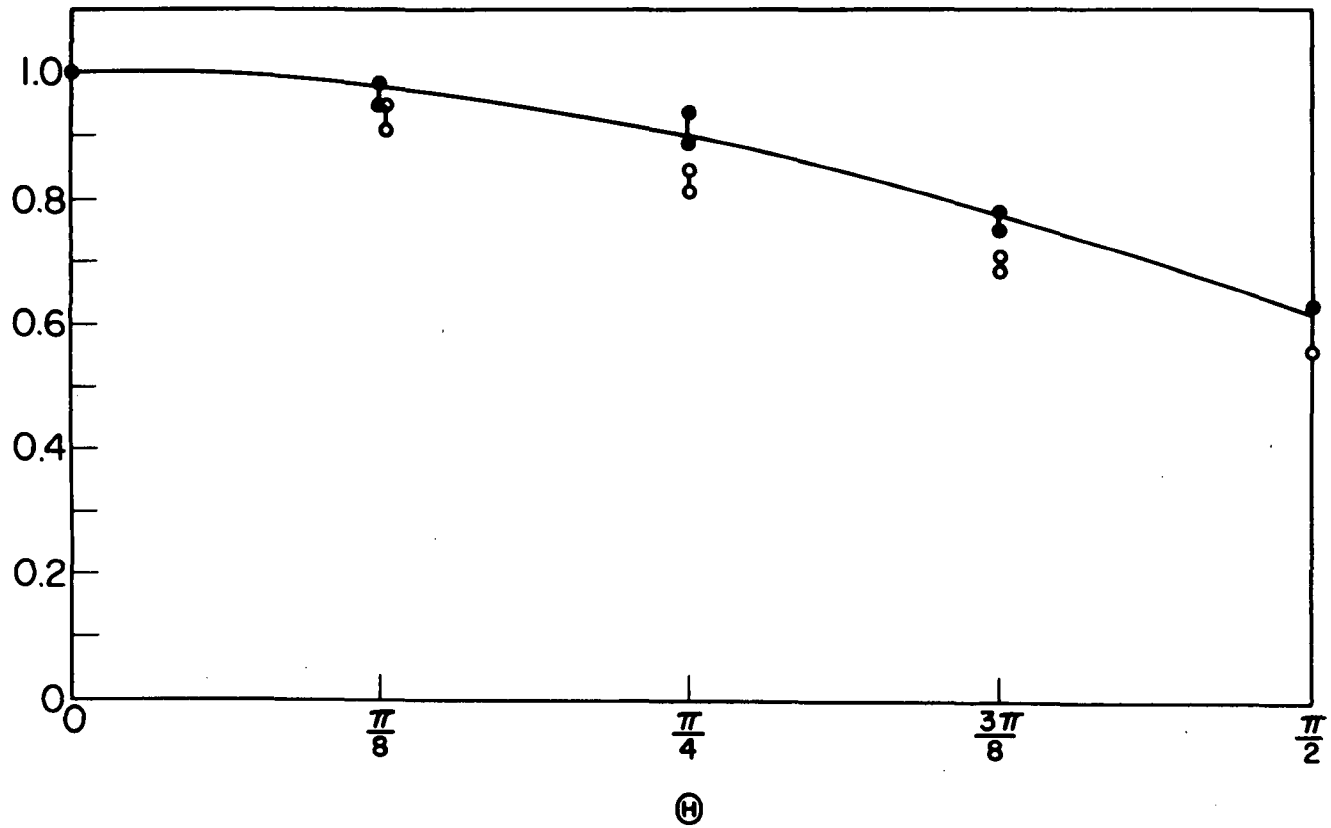

Figure 5.6

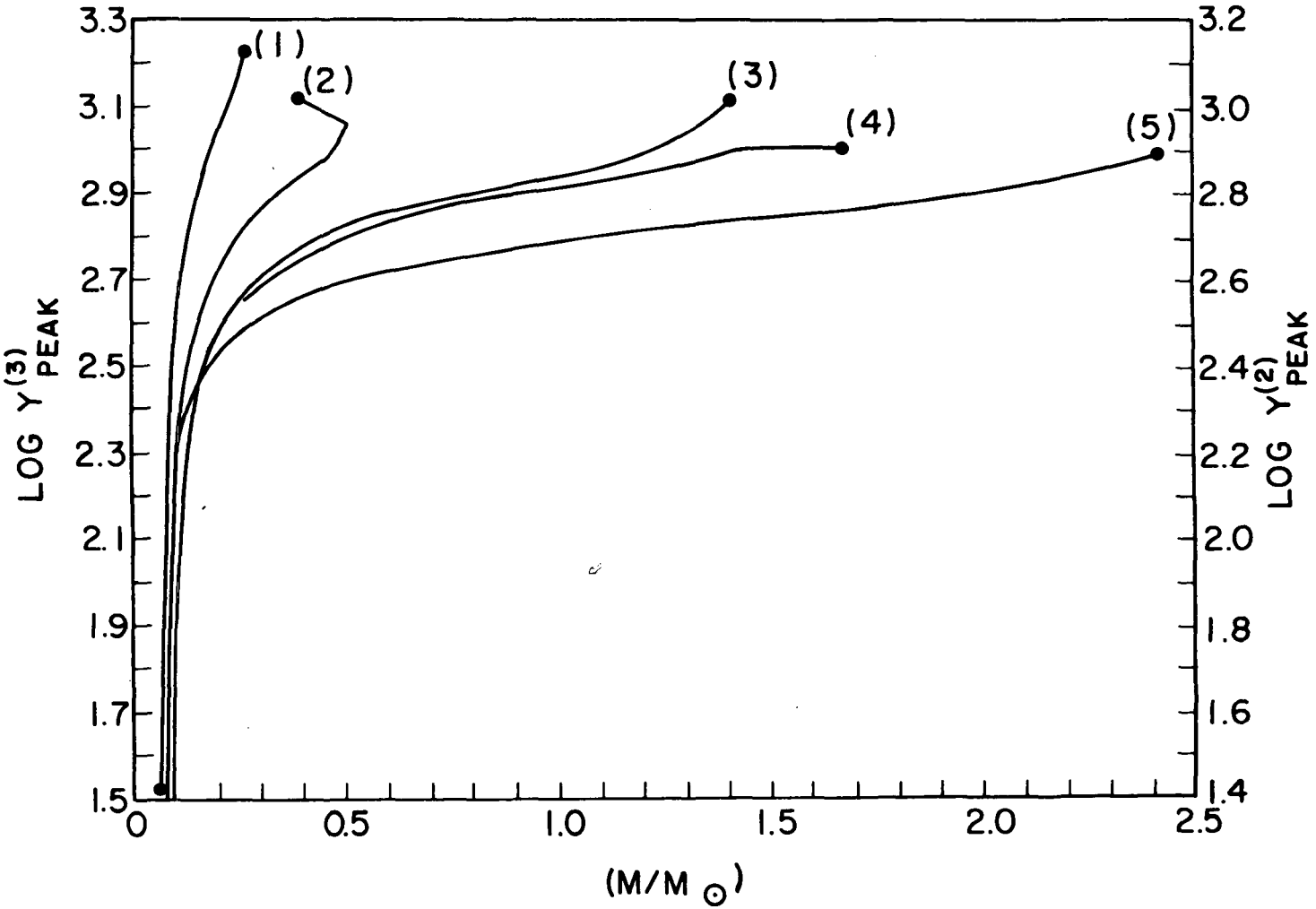
(1)
(2)
(3)
(4)
(5)
3.3
3.1
2.9
2.7
2.5
2.3
2.1
1.9
1.7
1.5
3.2
3.0
2.8
2.6
2.4
2.2
2.0
1.8
1.6
1.4
0
0.5
1.0
1.5
2.0
2.5
LOG Y(3) PEAK
LOG Y(2) PEAK
(M/M ⊙)

Figure 5.7

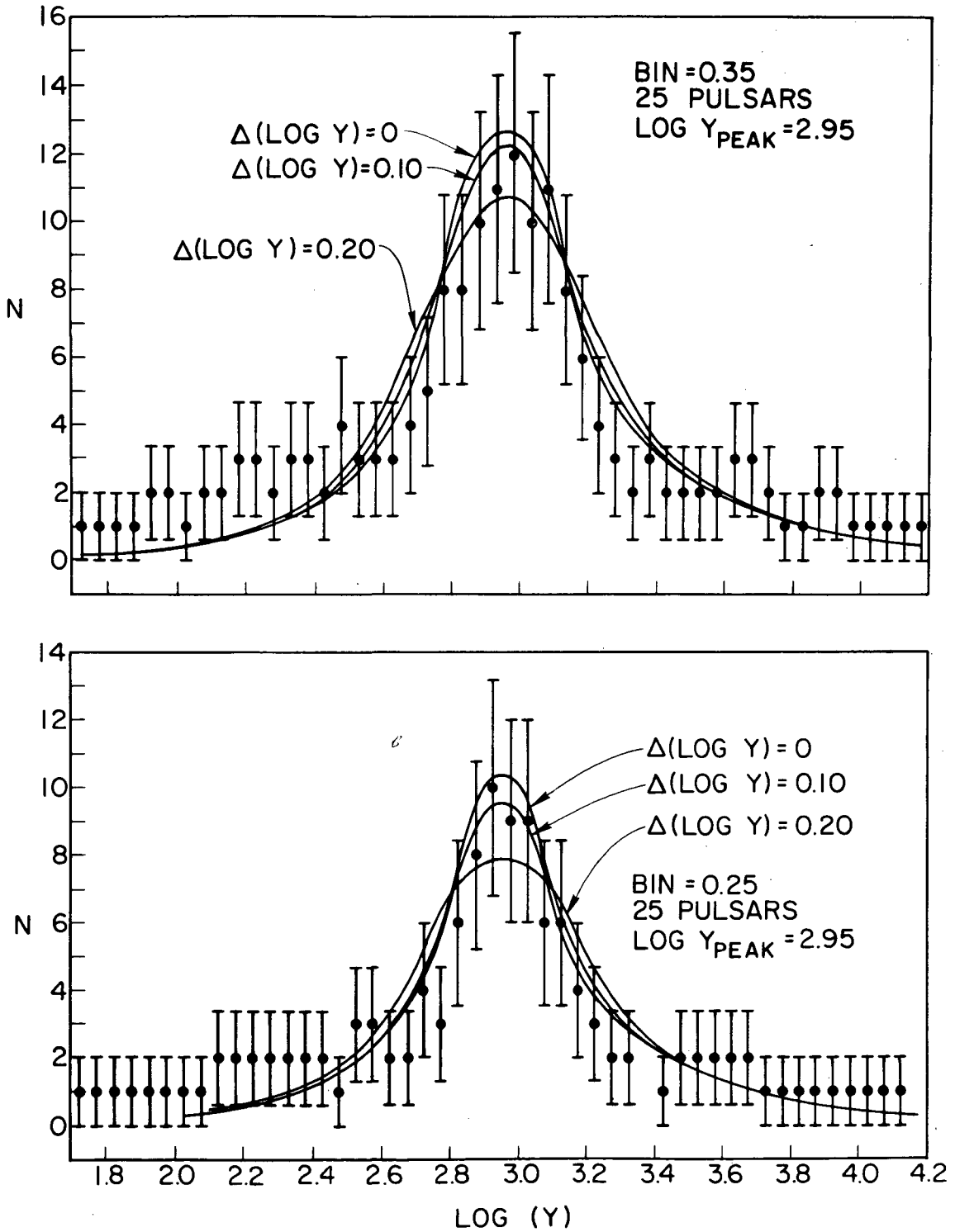
BIN=0.35
25 PULSARS
LOG Y_{PEAK}=2.95
Δ(LOG Y)=0
Δ(LOG Y)=0.10
Δ(LOG Y)=0.20
N
BIN=0.25
25 PULSARS
LOG Y_{PEAK}=2.95
Δ(LOG Y)=0
Δ(LOG Y)=0.10
Δ(LOG Y)=0.20
N
LOG (Y)

Figure 5.8

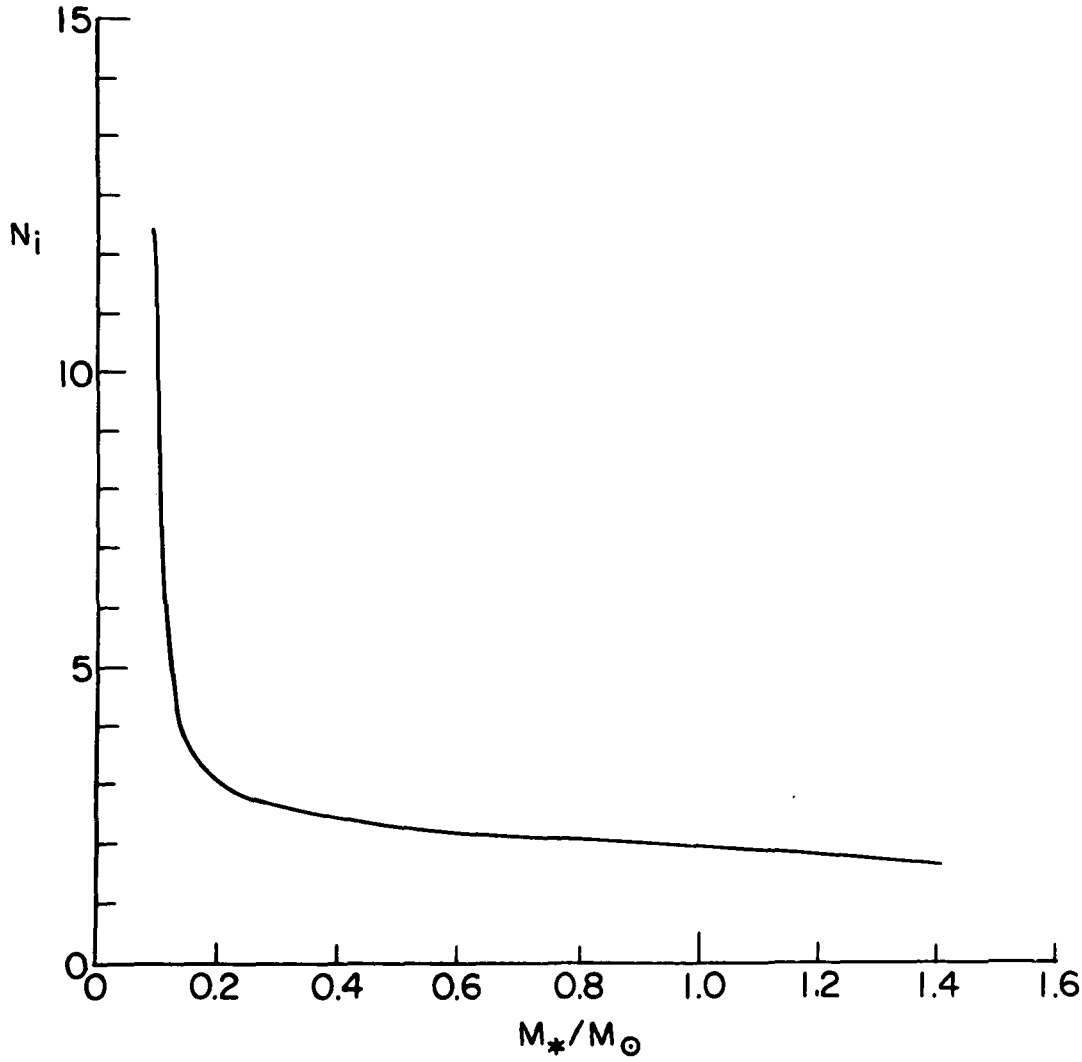

Figure 5.9

Chapter 6

DISCUSSION--CONCLUSIONS AND PROSPECTUS

In the Goldreich-Julian (1969) steady-state model, charged particles in the closed magnetosphere are tied to magnetic field lines which corotate with the underlying neutron star. This follows from the equation of motion under the assumption that gravity and inertia are negligible compared with the electromagnetic forces. In our model on the other hand, gravitational and centrifugal forces are assumed to dominate in the region of closed field lines, but the plasma still is tied to corotating field lines. Thus it is reasonable to inquire as to the consistency of our calculation of microscopic stability.

The electric field which drives corotation is derived from a charge density which may be found from Poisson's equation:

$$e|n_+ - n_-| \sim E/4\pi r \ ; \tag{6.1}$$

r is a characteristic length in the magnetosphere. In a magnetic field this produces an $\vec{E} \times \vec{B}$ drift

$$v_{E\times B} \sim cE/B \sim 4\pi cer|n_+ - n_-|B^{-1} \ , \tag{6.2}$$

so that the condition of corotation, $v_{E\times B} \sim \omega r$, implies that the charge density is

$$|n_+ - n_-| \sim \omega B/4\pi ec \ . \tag{6.3}$$

This is of course the same as that given by Goldreich and Julian [Eq. (2.12)].

The gravitational force per unit volume is

$$f_g \sim GM_* \, m_p(n_+ + n_-) r^{-2} \ , \tag{6.4}$$

the centrifugal force per unit volume is

$$f_c \sim (n_+ + n_-) \, m_p \omega^2 r \ , \tag{6.5}$$

and the electromagnetic force per unit volume is

$$f_{em} \sim |n_+ - n_-| \, evB/c \ . \tag{6.6}$$

Thus gravity dominates electromagnetic forces if

$$\left| \frac{n_+ + n_-}{n_+ - n_-} \right| \gg \left(\frac{r}{R_{FB}} \right)^3 \left(\frac{eB}{m_p \omega c} \right) \tag{6.7}$$

and centrifugal force dominates electromagnetic forces if

$$\left| \frac{n_+ + n_-}{n_+ - n_-} \right| \gg \frac{eB}{m_p \omega c} \ . \tag{6.8}$$

[The criterion (6.8) is the same as that given by Ruderman (1972) in order that the Alfvén cylinder be substantially inside the light cylinder.] Substituting the charge density required for corotation from Eq. (6.3), the mass density must satisfy

$$m_p(n_+ + n_-) \gg B^2/4\pi c^2 \ . \tag{6.9}$$

Evaluated at the force-balance radius for the Crab pulsar, the right hand side of Eq. (6.9) is about 10^{-6} g cm^{-3}. A mass of $10^{21.2}$ g dumped from R_{FB} is appropriate for a glitch in the Crab; if contained in a volume $V = \pi(R_{FB}/5)^2 \, 2\pi \, R_{FB}$ this has a density about 1 g cm^{-3}. Thus it appears that the kind of mass densities involved in magnetospheric

activity insure the consistency of our assumptions about microscopic stability.

The criteria which we have used to decide between macroscopic stability and instability were based on the assumption that so much mass will collect that the magnetic field cannot support it against gravity or contain it against centrifugal force. We have seen that microscopic stability can occur only for radii comparable with or greater than the force-balance distance, so we will concern ourselves with the effects of centrifugal force. The magnetic force which contains plasma is

$$f_m = \nabla(B^2/8\pi) \sim B^2/8\pi r \quad . \tag{6.10}$$

We may define a critical mass density ρ_c by equating f_c and f_m,

$$\rho_c = (B^2/8\pi c^2)(R_L/r)^2 \; ; \tag{6.11}$$

densities which exceed this cannot be held in corotation except in the force-balance region.

The maximum plasma moment of inertia which can be contained by the magnetic field outside of the region of cancellation of gravitational and centrifugal forces is

$$I_{max} = \int_{R_{FB}}^{R_L} \rho_c r^2 \, 4\pi r^2 dr \simeq B_*^2 R_*^6/6\omega^2 R_{FB}^3 \quad . \tag{6.12}$$

Evaluated for Crab pulsar parameters, $I_{max} \sim 10^{32.5}$ g cm^2, so that $I_{max}/I_* \sim 10^{-12}$. This is three or four orders of magnitude too small to account for the glitches, but is suggestive of the noise seen in the Crab timing data. We infer that non-relativistic gas at densities greatly

exceeding ρ_c collects near R_{FB}, and that when densities approaching ρ_c build up outside R_{FB} they result in macroscopic instability. The resulting changes in the magnetic field configuration may be related to the restless behavior of the Crab pulsar.

Lehnert (1960), in a paper on the confinement of rotating plasmas by a magnetic field, notes that "In a theory on the origin of the solar system, Alfvén (1954) considers a cosmic cloud of ionized gas, rotating around a central mass M_c in a magnetic dipole field which has a dipole moment coinciding with the axis of rotation. In the theory is introduced a dividing surface. At the inner side of this surface, the parts of the cloud are attracted and fall down to the central body. Outside of the same surface, the centrifugal force brings matter out along the magnetic field lines down to the equitorial plane where planets or satellites may be formed. Alfvén determines the dividing surface from the balance between the gravitational and centrifugal forces." His expression for the dividing surface, when rewritten in spherical polar coordinates, is

$$r^3 \sin^2\theta = 2\, G\, M_c / 3\omega^2 \; ; \tag{6.13}$$

using Eqs. (5.2.4), (5.2.7), (5.2.11), and (5.2.25), this becomes

$$\chi^4 = 2/3\, \beta^3 \; . \tag{6.14}$$

This is identical with our Eq. (5.3.4), which defines the boundary of the microscopically stable region in the aligned case.

Lehnert further states "In connection with this problem should also be pointed out that a weak magnetic field ... is expanded radially by the centrifugal force. The present deductions merely serve as an illustration to the situation where the magnetic field is strong enough to

balance this force." This is analogous to our assertion that outside of the force-balance region centrifugal force will convert closed field lines into open field lines, and that the resulting magnetic field will fall off as $B \propto r^{-2}$.

The pulsar model at which we have arrived combines the magnetospheric structure laid out in the preceding chapters with the radiation mechanisms described by Sturrock (1970, 1971a). The modifications of Sturrock's work which arise in the change from $R_Y = R_L$ to $R_Y = R_{FB}$ have been worked out in detail by Turk (1972). A discussion of the results has been given by Roberts, Sturrock, and Turk (1973), and we will briefly mention some of their conclusions.

Table 6.1 sums up some of the comparisons between a model where the radiation arises at the light cylinder and the two polar cap models -- first, that for which $R_Y = R_L$, and second that for which $R_Y = R_{FB}$. Concerning the braking index, the first two give $n = 3$, which is wrong. The revised model gives $n = 7/3 = 2.33$, which is consistent with the data. The fact that some pulsars have an interpulse which is off-center is hard to understand in terms of the light cylinder model (this is because multipole moments higher than dipole will have fallen off faster at the light cylinder, unless the contribution to the magnetic field of currents flowing in the open magnetosphere is significant; Sturrock 1971a). However, it follows naturally from either polar cap model. Further, the revised polar cap model enables one to understand the number of pulsars which show an interpulse.

Timing noise is not a natural consequence of either of the first two models, but it is a readily understandable property of the third. Since

radiation is produced near the surface and the magnetospheric configuration is determined near the force-balance radius, it is easy to understand the fact that the pulse-shape of the Crab pulsar did not change around the time of the September 1969 glitch. On the other hand, we do not think it is easy to understand a large glitch, such as have been observed in the Vela timing data, as being a magnetospheric phenomenon. Concerning the period-pulse-width relation, there is no clear indication of what this should be for the first model; we know that the second model gives one which is incorrect, but it appears that the third model gives a relation which is compatible with observation. There is growing evidence, however, that there may be two distinct classes of pulsars, and the W-T distribution should be re-examined in this light.

None of these models offers an obvious explanation of the drifting subpulse phenomenon. However, we have mentioned one possibility in Chapter 5, and the presence of non-relativistic gas in the magnetosphere suggests another--that Alfvén-wave oscillations might be involved. These ideas should be explored more fully.

The radiation properties of the three models are also summarized in Table 6.1. Little is known about the electrodynamics of the light cylinder model, so it is hard to make comparisons with the data. Looking at the two polar cap models, we see that either explains the period-age distribution, and that either can account for the RF properties. According to Turk, Sturrock, and Petrosian (1973), the force-balance model can better explain the optical properties. Either can explain the x-ray properties and the particle flux into the Crab nebula.

TABLE 6.1

MAGNETOSPHERIC STRUCTURE
AND RADIATION MECHANISMS

		LIGHT CYLINDER	POLAR CAP $R_Y = R_L$	POLAR CAP $R_Y = R_{FB}$
1.	BRAKING INDEX	X	X	√
2.	INTERPULSE, OFF-CENTER	X	√	√
3.	TIMING NOISE, CRAB GLITCH	X	X	√
4.	GLITCH (BIG, VELA-TYPE)	?	?	?
5.	PERIOD-PULSE-WIDTH DISTRIBUTION	?	X	√
6.	DRIFTING SUB-PULSE STRUCTURE	X	X	?
7.	PERIOD-AGE DISTRIBUTION	?	√	√
8.	RF PROPERTIES	?	√	√
9.	OPTICAL PROPERTIES	?	X	√
10.	X-RAY PROPERTIES	?	√	√
11.	PARTICLE FLUX INTO CRAB NEBULA	?	√	√

Author's evaluation of properties of models: √ indicates apparent agreement with observational data; X indicates apparent disagreement; ? indicates uncertainty.

Appendix A

POLAR CAPS AND EMISSION CONES

In a coordinate system where the magnetic axis is in the z-direction and the rotation axis lies in the x-z plane at polar angle Θ, dipole field lines are the surfaces

$$r^{-1} \sin^2\theta = r_o^{-1} = \text{constant} , \tag{A.1}$$

and a cylinder of radius R_Y aligned with $\vec{\omega}$ is the surface

$$r \sin\gamma = R_Y , \tag{A.2}$$

where γ is the angle between $\vec{r}$ and $\vec{\omega}$,

$$\cos\gamma = \cos\theta \cos\Theta + \sin\theta \sin\Theta \cos\phi . \tag{A.3}$$

For a given $(\phi;\Theta)$, these two surfaces intersect at (r,θ) determined by

$$r_o \sin^2\theta \sin\gamma = R_Y . \tag{A.4}$$

The first field line to intersect the cylinder (the one which is tangent to it) does so at an angle θ_c such that r_o is a minimum. The condition $\partial r_o/\partial\theta = 0$ is

$$\sin\theta[2\cos\theta \sin\gamma + \sin\theta(\cos\gamma/\sin\gamma)(\sin\theta \cos\Theta - \cos\theta \sin\Theta \cos\phi)] = 0 . \tag{A.5}$$

(The solution $\theta = 0$ corresponds to a maximum of r_o.)

Tracing these grazing field lines back to the star's surface $r = R_*$, they form two polar caps, at colatitudes θ_r and $\pi - \theta_r$, where

$$R_*^{-1}\sin^2\theta_r = r_c^{-1}\sin^2\theta_c = R_Y^{-1}\sin^2\theta_c \sin\gamma(\theta_c) , \tag{A.6}$$

and two emission cones consisting of the tangents to the field lines where they cut the surface. The half-angle ψ of a cone is given by

$$\tan\psi = (3/2)\sin\theta_r\{[1 - \sin\theta_r]/[1 - (3/2)\sin^2\theta_r]\} , \qquad (A.7)$$

which is well approximated (to order [W/T]) by

$$\psi = (3/2)\ \sin\theta_r \ . \qquad (A.8)$$

The solution of Equation (A.5) for general $(\phi;\Theta)$ is involved, and we shall content ourselves with the major and minor axes of the emission cone for arbitrary Θ, and the complete solution for $\Theta = \pi/2$.

y-z Plane ($\phi = \pi/2$), Major Axis:

With $\cos\phi = 0$, Eq. (A.5) is

$$\cos\theta(2\ \sin^2\Theta + 3\ \sin^2\theta\ \cos^2\Theta) = 0 , \qquad (A.9)$$

the only real solution of which is $\theta_c = \pi/2$, $\sin\gamma = 1$, so the half-angle of the emission cone in the direction of increasing longitude (referred to the rotation axis) is

$$\psi_\ell = (3/2)(R_*/R_Y)^{1/2} \ . \qquad (A.10)$$

x-z Plane ($\phi = 0$), Minor Axis:

With $\cos\phi = 1$, Eq. (A.3) implies

$$\gamma = \theta - \Theta , \qquad (A.11)$$

so Eq. (A.5) reads

$$2 \sin\theta \cos\theta \sin(\theta-\Theta) + \sin^2\theta \cos(\theta-\Theta) = 0 \ . \qquad (A.12)$$

From this we find the relation

$$\tan\Theta = (3 \tan\theta_c)/(2 - \tan^2\theta_c) \ . \qquad (A.13)$$

(The expression given in Paper I contains a typographical error.) Noting that $\theta_c \geq \pi/2$, we invert Eq. (A.13) to find

$$\theta_c = \arctan\{[-3-(9+8 \tan^2\Theta)^{1/2}]/[2 \tan\Theta]\} \ . \qquad (A.14)$$

Thus the half-angle in the direction of increasing latitude (referred to the rotation axis) is

$$\psi_b(\Theta) = (3/2)(R_*/R_Y)^{1/2} \ G(\Theta) \ , \qquad (A.15)$$

where G is defined by

$$G(\Theta) = \sin\theta_c \ \sin^{1/2}(\theta_c-\Theta) \ , \qquad (A.16)$$

with θ_c determined by Eq. (A.14).

Polar Caps in the Orthogonal Case:

When $\Theta = \pi/2$, Eq. (A.5) has

$$\sin\theta \cos\theta(2 - 3 \sin^2\theta \cos^2\phi) = 0 \ . \qquad (A.17)$$

One solution is $\sin^2\theta_c = 1$, the other

$$\sin^2\theta_c = 2/(3 \cos^2\phi) \ , \qquad (A.18)$$

for which we must have $\cos^2\phi \geq 2/3$. We may verify that Eq. (A.18) indeed corresponds to the minimum r_o for ϕ in this range. Defining

$$F(\cos^2\phi) = \left[r_o(\sin^2\theta_c = 1)\right] - \left[r_o(\sin^2\theta_c = 2/3\ \cos^2\phi)\right], \qquad (A.19)$$

we find $F(2/3) = 0$, $F'(x)=(1/2)(1-x)^{-3/2} -(1/2)3^{3/2}$. Thus $F'(x \geq 2/3) \geq 0$, so that $F(x \geq 2/3) \geq 0$, QED. The resulting polar cap has the shape

$$\sin\theta_r = \begin{cases} (R_*/R_Y)^{1/2}\ 2^{1/2}\ 3^{-3/4}/\cos\phi\ , & \cos^2\phi \geq 2/3\ , \\ (R_*/R_Y)^{1/2}\ \sin^{1/2}\phi\ , & \cos^2\phi \leq 2/3\ . \end{cases} \qquad (A.20)$$

The simplified model of Chapter 4 has $R_Y = R_{FB}$, and we may compare the resulting polar cap to those found in the more complete model of Chapter 5. In Figure A.1 we have shown the scaled polar cap size $\varkappa(\phi)$ predicted by Eq. (A.20), along with those from Chapter 5, for the orthogonal case. The qualitative similarity occurs because the equipotentials of Chapter 5 are nearly cylindrical in shape, and the quantitative differences because they are perturbed by the gravitational potential.

Case of General ϕ and Θ:

For completeness, we note that for arbitrary $(\phi;\Theta)$ we may transform Eq. (A.5) into a cubic equation in $x = \tan\theta$:

$$a\ x^3 + b\ x^2 + c\ x + d = 0\ , \qquad (A.21)$$

where

$$\begin{aligned} a &= \sin\Theta\ \cos\Theta\ \cos\phi\ , \\ b &= 3 - \sin^2\Theta(1 + 3\ \cos^2\phi)\ , \\ c &= -5\ a\ , \\ d &= 2\ \sin^2\Theta\ . \end{aligned} \qquad (A.22)$$

FIGURE CAPTION

Figure A.1. Polar cap in the orthogonal case, plotted as $r = \varkappa(\phi)$ versus ϕ. Solid lines, the model of Chapter 4, where $R_Y = R_{FB}$. Broken lines, the model of Chapter 5. The larger cap corresponds to Criterion 1, the smaller one to Criterion 2.

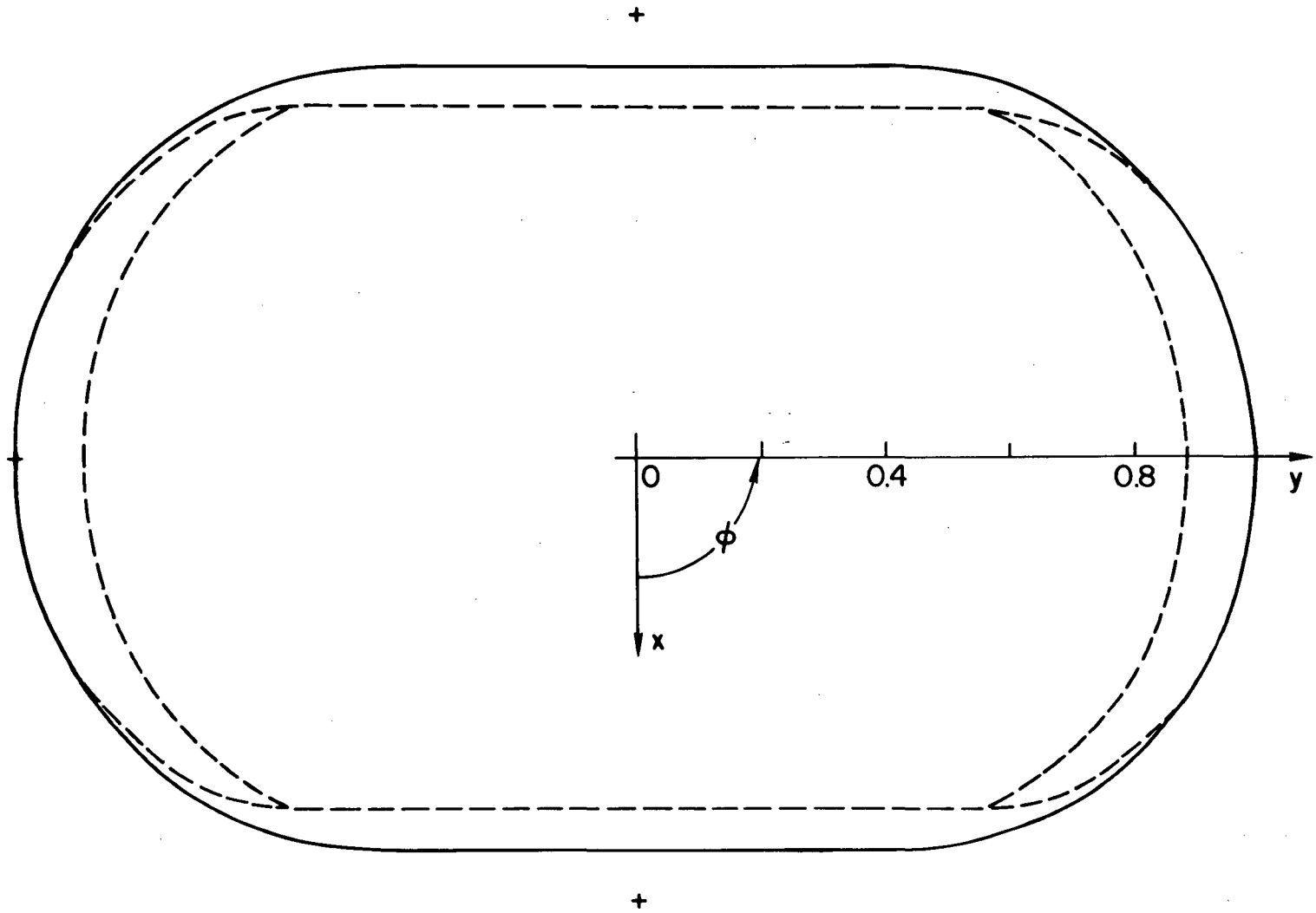

Figure A.1

Appendix B

THE PERIOD-PULSE-WIDTH DISTRIBUTION

Here we derive the period-pulse-width distribution expected from two emission cones located at opposite magnetic poles. Measuring angles from the rotation axis, let the cones be located at colatitudes Θ and $\pi - \Theta$, and have longitude and latitude half-angles ψ_ℓ and ψ_b, respectively. Assuming the shape of the cones to be approximately elliptical, and that ψ_ℓ and ψ_b are sufficiently small that plane geometry may be used, the pulse width W is related to the rotation period T by

$$\frac{W}{T} = \frac{2\psi_\ell\left[1 - \frac{(\phi-\Theta)^2}{\psi_b^2}\right]^{1/2}}{2\pi \sin\phi} , \qquad (B.1)$$

and a similar expression with $\Theta \to \pi - \Theta$ for the other pole. Here ϕ is the colatitude of the line of sight of the observer. If neither expression is found to be real, radiation is not detectable by the observer. This geometry is illustrated in Figure B.1.

The probability that W is in the range W to $W + dW$, given by twice the probability for one cone, is $P_W(W,T)dW$, where

$$P_W(W,T) = 2\int_0^\pi \frac{1}{2}\sin\Theta\, d\Theta \int_0^\pi \frac{1}{2}\sin\phi\, d\phi\, \delta\left\{W - \frac{T\,\psi_\ell}{\pi \sin\phi}\left[1 - \frac{(\phi-\Theta)^2}{\psi_b^2}\right]^{1/2}\right\} . \qquad (B.2)$$

[real integrand]

We have assumed that both the locations Θ of the emission cones and the angle of the line of sight ϕ are randomly distributed on $(0,\pi)$.

To transform the delta function we use the well-known rule

$$\delta[f(x)] = \sum_n \left|\frac{\partial f}{\partial x}\right|^{-1}_{x=x_n} \delta(x-x_n) , \qquad (B.3)$$

where

$$f(x_n) = 0 \ . \tag{B.4}$$

Defining

$$G(\Theta,\phi) = W - \frac{T\,\psi_\ell}{\pi \sin\phi}\left[1 - \frac{(\phi-\Theta)^2}{\psi_b^{\,2}}\right]^{1/2} \ , \tag{B.5}$$

we have

$$\frac{\partial G}{\partial \phi} = \frac{T\,\psi_\ell}{\pi \sin\phi}\left[1 - \frac{(\phi-\Theta)^2}{\psi_b^{\,2}}\right]^{-1/2}(\phi-\Theta)\psi_b^{-2} + \frac{T\,\psi_\ell \cos\phi}{\pi \sin^2\phi}\left[1 - \frac{(\phi-\Theta)^2}{\psi_b^{\,2}}\right]^{1/2} \ . \tag{B.6}$$

Here ϕ_n are the solution of $G = 0$, i.e., of

$$W = \frac{T\,\psi_\ell}{\pi \sin\phi_n}\left[1 - \frac{(\phi_n-\Theta)^2}{\psi_b^{\,2}}\right]^{1/2} \ . \tag{B.7}$$

Since we assume ψ_ℓ and ψ_b are small, we may put $\sin\phi_n \simeq \sin\Theta$, and thus

$$\phi_n = \Theta \pm \psi_b\sqrt{1 - \frac{W^2\pi^2\sin^2\Theta}{T^2\psi_\ell^{\,2}}} \ , \tag{B.8}$$

and (B.6) becomes

$$\left.\frac{\partial G}{\partial \phi}\right|_{\phi=\phi_n} = \pm \frac{T^2\psi_\ell^{\,2}\sqrt{1 - \dfrac{W^2\pi^2\sin^2\Theta}{T^2\psi_\ell^{\,2}}}}{\psi_b W\,\pi^2\sin^2\Theta} + W\sin^3\Theta\cos\Theta \ . \tag{B.9}$$

To order (W/T) the first term dominates, so both solutions to $G = 0$ are the same, and we may easily do the delta-function integration over ϕ;

$$P_W(W,T) = T^{-1}\, 2\pi \int_0^{\Theta_M} \frac{\sin^4\Theta(\psi_b/\psi_\ell)d\Theta}{\sqrt{\frac{\psi_\ell^2 T^2}{W^2\pi^2} - \sin^2\Theta}} \quad , \tag{B.10}$$

where

$$\Theta_M = \begin{cases} \frac{\pi}{2} & , \quad \frac{\psi_\ell T}{\pi W} \geq 1 \\ \sin^{-1}\left(\frac{\psi_\ell T}{\pi W}\right) & , \quad \frac{\psi_\ell T}{\pi W} < 1 \end{cases} . \tag{B.11}$$

We have used the invariance of the integrand under $\Theta \to \pi - \Theta$.

In our model

$$\psi_\ell = \frac{3}{2} R_*^{1/2} R_Y^{-1/2} ,$$
$$\psi_b = \psi_\ell\, G(\Theta) . \tag{B.12}$$

We may parametrize $R_Y(T)$ by R_o and η by defining

$$R_Y = R_o T^\eta ; \tag{B.13}$$

if we further define

$$k = \frac{9R_*}{4\pi^2 R_o} , \tag{B.14}$$

$$y = T^{2-\eta} W^{-2} , \tag{B.15}$$

so that

$$\frac{\psi_\ell^2 T^2}{W^2\pi^2} = ky , \tag{B.16}$$

then

$$P_W(W,T) = 2\pi T^{-1} \int_0^{\Theta_M} \frac{\sin^4\Theta\, G(\Theta)\, d\Theta}{\sqrt{ky - \sin^2\Theta}} \quad . \tag{B.17}$$

It is convenient to transform to the probability that y is in the range y to $y+dy$. Using the identity

$$|P_W(W,T)dW| = |P_y(y,T)dy| \tag{B.18}$$

we find the central result

$$P_y(y,T) = \frac{1}{2}\, T^{-\eta/2}\, y^{-3/2}\, L(ky) \quad , \tag{B.19}$$

where we have defined

$$L(x) = 2\pi \int_0^{\Theta_M} \frac{\sin^4\Theta\, G(\Theta)\, d\Theta}{\sqrt{x - \sin^2\Theta}} \quad , \tag{B.20}$$

with

$$\Theta_M = \begin{cases} \frac{\pi}{2} & , \quad x \geq 1 \\ \sin^{-1} x & , \quad x < 1 \end{cases} \quad . \tag{B.21}$$

Calculation of the function $L(x)$ and its integrals is discussed in detail in Appendix C.

FIGURE CAPTION

Figure B.1. The geometry of the polar cap model, showing only one magnetic pole.

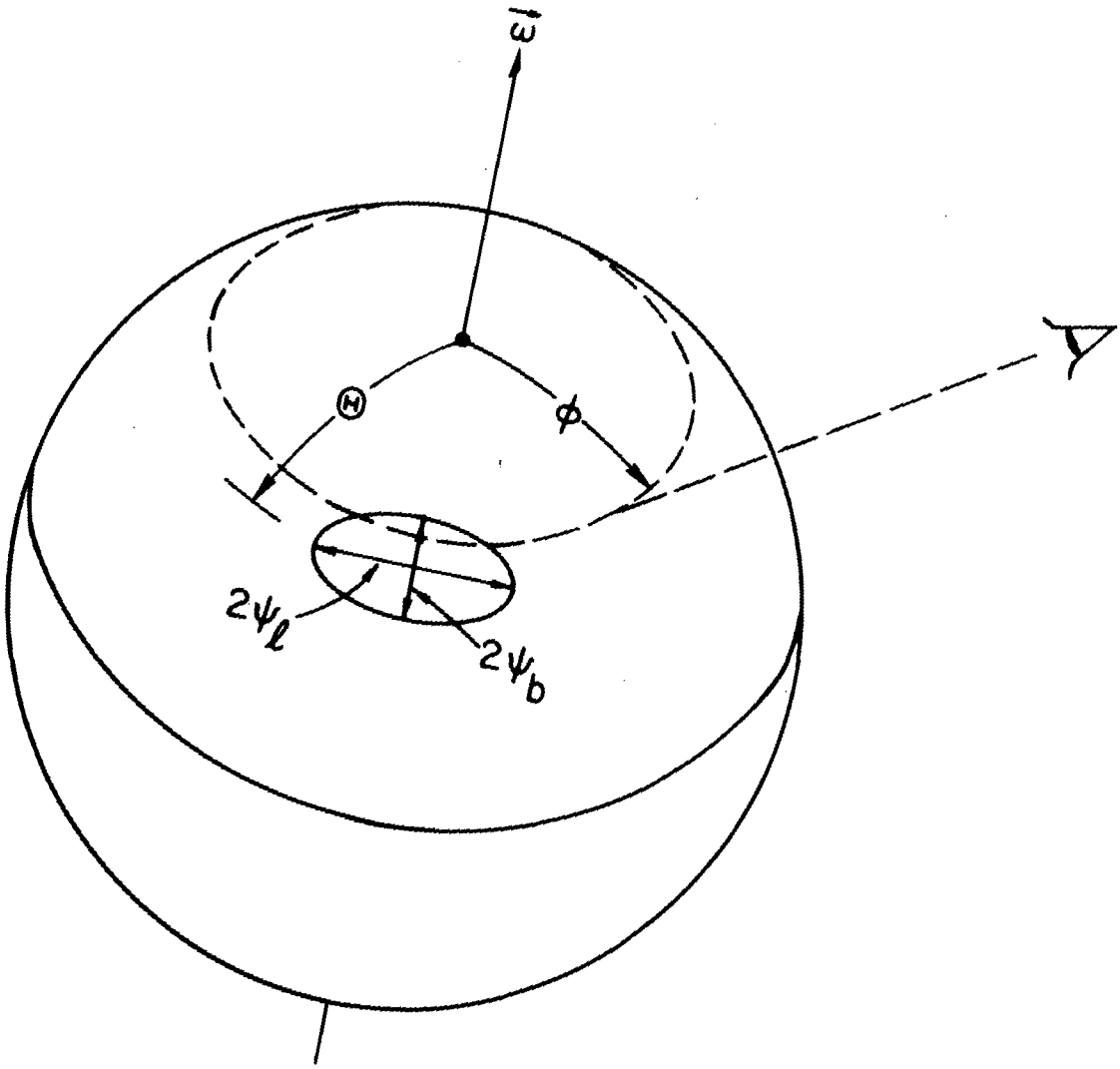

Figure B.1

Appendix C

THE FUNCTION L(x)

The function $L(x)$ is defined by

$$L(x) = 2\pi \int_0^{\Theta_m} \frac{\sin^4\Theta \, G(\Theta) d\Theta}{\sqrt{x-\sin^2\Theta}} \quad , \tag{C.1}$$

where

$$\Theta_m = \begin{cases} \frac{\pi}{2} & , \quad x \geq 1 \\ \sin^{-1}\sqrt{x} \, , & x < 1 \end{cases} \quad . \tag{C.2}$$

We first demonstrate that L is integrable near the singularity at $x = 1$. For $x \geq 1$ we use $z = \sin\Theta$ to rewrite L as

$$L(x) = 2\pi \int_0^1 \frac{z^4 G(\sin^{-1} z) dz}{\sqrt{(1-z^2)(x-z^2)}} \quad (x \geq 1) \, , \tag{C.3}$$

and for $x \leq 1$ we employ $\sin\Theta = z\sqrt{x}$ to write

$$L(x) = 2\pi \, x^{3/2} \int_0^1 \frac{z^4 G[\sin^{-1}(z\sqrt{x})] dz}{\sqrt{(1/x-z^2)(1-z^2)}} \quad (x \leq 1) \, . \tag{C.4}$$

The complete elliptic integral of the first kind is defined (Abramowitz and Stegun 1970, 17.3.1) as

$$K(m) = \int_0^1 [(1-t^2)(1-mt^2)]^{-1/2} \, dt \tag{C.5}$$

so

$$\int_0^1 [(1-t^2)(m-t^2)]^{-1/2} dt = \frac{1}{\sqrt{m}} K\left(\frac{1}{m}\right) . \qquad (C.6)$$

As z^4 and G are less than one, from (C.3) and (C.4) we find

$$L(x) \leq 2\pi\, x^{-1/2} K\left(\frac{1}{x}\right) \quad (x \geq 1) , \qquad (C.7)$$

and

$$L(x) \leq 2\pi\, x^2 K(x) \quad (x \leq 1) . \qquad (C.8)$$

The asymptotic form of $K(m)$ is (Abramowitz and Stegun 17.3.26)

$$K(m) \xrightarrow[m \to 1^-]{} \frac{1}{2} \ln \frac{16}{1-m} , \qquad (C.9)$$

so putting

$$x = 1 \pm \varepsilon \quad (x \gtrless 1) \qquad (C.10)$$

we have

$$L(x) \leq 2\pi(1+\varepsilon)^{-1/2} \frac{1}{2} \ln(16/\varepsilon) , \quad (x = 1+\varepsilon > 1) , \qquad (C.11)$$

$$L(x) \leq 2\pi\, (1-\varepsilon)^2 \frac{1}{2} \ln(16/\varepsilon) , \quad (x = 1-\varepsilon < 1) . \qquad (C.12)$$

It is evident that we need consider only one case, so we examine

$$\int_1^{1+\varepsilon} L(x)dx \leq \pi \int_0^{\varepsilon} (1+\varepsilon)^{-1/2} \ln(16/\varepsilon) d\varepsilon . \qquad (C.13)$$

For small ε this is dominated by $-\pi\varepsilon \ln \varepsilon$, which shows that $L(x)$ is integrable across $x = 1$.

In order to tabulate the function L and its integrals we use the forms (C.3) and (C.4). Subtracting off the singularities at $z = 1$,

$$L(x) = 2\pi \int_0^1 g_>(z)dz + 2\pi\, G(\tfrac{\pi}{2})\sqrt{\frac{2}{x-1}} \quad , \qquad (x \geq 1) \quad (C.14)$$

$$g_>(z) = \frac{z^4 G(\sin^{-1} z)}{\sqrt{(1-z^2)(x-z^2)}} - \frac{G(\pi/2)}{\sqrt{2(1-z)(x-1)}}$$

and

$$L(x) = 2\pi\, x^{3/2} \int_0^1 g_<(z)dz + 2\pi\, x^{3/2}\, G(\sin^{-1}\sqrt{x})\sqrt{\frac{2x}{1-x}} \quad , \qquad (x \leq 1) \quad (C.15)$$

$$g_<(z) = \frac{z^4 G[\sin^{-1}(z\sqrt{x})]}{\sqrt{(1-z^2)(1/x-z^2)}} - \frac{G(\sin^{-1}\sqrt{x})}{\sqrt{2(1-z)(1/x-1)}} \quad .$$

The remaining numerical integrals may be handled easily by standard methods. The resulting function $L(x)$ may be integrated numerically, as we have shown that the contribution from the singularity at $x = 1$ may be made arbitrarily small. The precise integral required is [see Eq. (3.16)]

$$\Delta(z_1, z_2) \equiv \frac{1}{\lambda} \int_{z_1}^{z_2} z^{-3/2} L(z)dz \quad . \qquad (C.16)$$

From Eqs. (C.3) and (C.4) it is easily demonstrated that

$$L(x) \underset{x \gg 1}{\leqslant} \pi^2 x^{-1/2} \qquad (C.17)$$

and

$$L(x) \underset{x \ll 1}{\approx} \pi^2 x^2 \qquad (C.18)$$

so that λ, defined by

$$\lambda = \int_0^\infty z^{-3/2} L(z) dz \ , \qquad (C.19)$$

is finite ($\lambda = 7.772$). The function Δ is recorded in Table C for steps of 0.1 in $\log_{10}(z)$, and is illustrated in Figure C.1.

TABLE CAPTION

Table C. The function $\Delta(z_1, z_2)$, as defined by Eq. (C.16), for steps of 0.1 in log (z). The value of Δ for each interval is the number in column 3 times 10 to the power entered in column 4.

TABLE C.1

$\log z_1$	$\log z_2$	$\Delta(z_1, z_2)$	$\times 10^{\alpha}$	SUMS OF BINS	
-2.0	-1.9	.131302	-3	.0003	.000951
-1.9	-1.8	.185621	-3		
-1.8	-1.7	.262470	-3	.0006	
-1.7	-1.6	.371237	-3		
-1.6	-1.5	.525261	-3	.0012	.003814
-1.5	-1.4	.743518	-3		
-1.4	-1.3	.105307	-2	.0026	
-1.3	-1.2	.149258	-2		
-1.2	-1.1	.211752	-2	.0051	.015506
-1.1	-1.0	.300781	-2		
-1.0	-0.9	.427929	-2	.0104	
-0.9	-0.8	.610122	-2		
-0.8	-0.7	.872385	-2	.0212	.065637
-0.7	-0.6	.125231	-1		
-0.6	-0.5	.180777	-1	.0444	
-0.5	-0.4	.263121	-1		
-0.4	-0.3	.387964	-1	.0973	.372073
-0.3	-0.2	.585078	-1		
-0.2	-0.1	.925510	-1	.2748	
-0.1	0.0	.182218	0		
0.0	0.1	.177488	0	.2720	.383792
0.1	0.2	.945468	-1		
0.2	0.3	.647181	-1	.1117	
0.3	0.4	.470388	-1		
0.4	0.5	.352098	-1	.0620	.098719
0.5	0.6	.268172	-1		
0.6	0.7	.206565	-1	.0367	
0.7	0.8	.160350	-1		
0.8	0.9	.125165	-1	.0223	.036114
0.9	1.0	.980978	-2		
1.0	1.1	.771177	-2	.0138	
1.1	1.2	.607641	-2		
1.2	1.3	.479629	-2	.0086	.013962
1.3	1.4	.379101	-2		
1.4	1.5	.299959	-2	.0054	
1.5	1.6	.237536	-2		
1.6	1.7	.188224	-2	.0034	.005497
1.7	1.8	.149225	-2		
1.8	1.9	.118354	-2	.0021	
1.9	2.0	.938993	-3		
2.0	2.1	.745159	-3	.0013	.002179
2.1	2.2	.591454	-3		
2.2	2.3	.469527	-3	.0008	
2.3	2.4	.372782	-3		
2.4	2.5	.295999	-3	.0005	.000866
2.5	2.6	.235050	-3		
2.6	2.7	.186663	-3	.0002	
2.7	2.8	.148244	-3		

SUMS TO 0.9991

FIGURE CAPTION

Figure C.1. Histogram of the function $\Delta(z_1, z_2)$, as defined by Eq. (C.16).

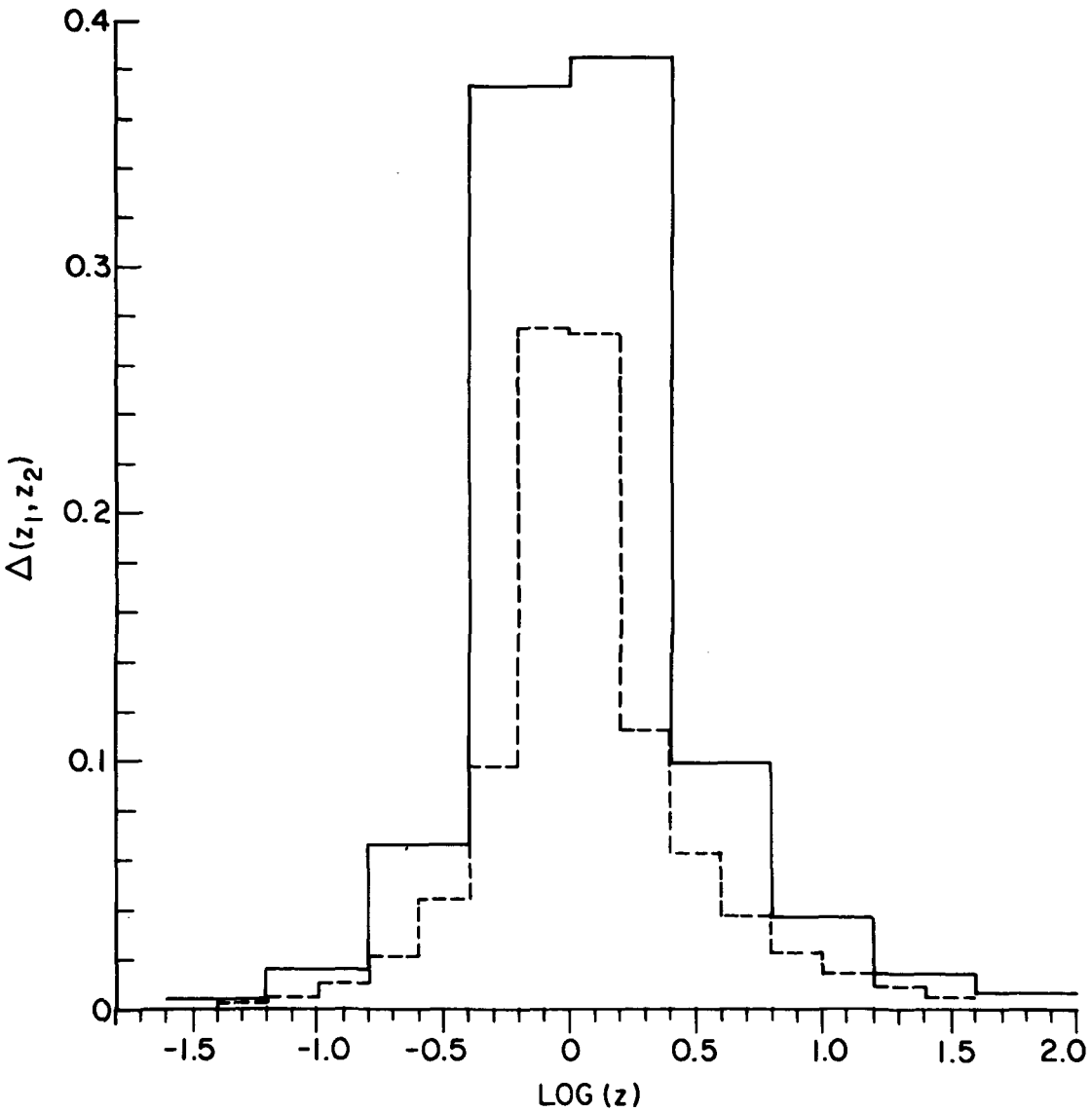

Figure C.1

Appendix D

INTERPULSES

We first consider the fraction of pulsars which are observed. If the (+) magnetic pole is at colatitude Θ and the (-) pole at colatitude $\pi - \Theta$, the observer detects radiation from the (+) pole if the line of sight ϕ satisfies

$$\Theta - \psi_b < \phi < \Theta + \psi_b \ , \tag{D.1}$$

and he sees the (-) pole if

$$\pi - \Theta - \psi_b < \phi < \pi - \Theta + \psi_b \ . \tag{D.2}$$

These regions are shown in Figure D.1. Assuming random orientations of Θ and ϕ, the probabilities that he sees the (+) or (-) poles are

$$P_+ = \int_0^{\pi} \frac{1}{2} \sin\Theta \, d\Theta \int_{\Theta-\psi_b}^{\Theta+\psi_b} \frac{1}{2} \sin\phi \, d\phi \ , \tag{D.3}$$

and

$$P_- = \int_0^{\pi} \frac{1}{2} \sin\Theta \, d\Theta \int_{\pi-\Theta-\psi_b}^{\pi-\Theta+\psi_b} \frac{1}{2} \sin\phi \, d\phi \ . \tag{D.4}$$

Clearly $P_+ = P_-$, and we evaluate only P_+:

$$P_+ = \frac{1}{4} \int_0^{\pi} \sin\Theta [-\cos(\Theta+\psi_b) + \cos(\Theta-\psi_b)] d\Theta \ , \tag{D.5a}$$

$$P_+ = \int_0^{\pi/2} \sin^2\Theta \sin\psi_b \, d\Theta \ . \tag{D.5b}$$

Now $\sin\psi_b = (3/2)(R_*/R_Y)^{1/2}\, G(\Theta)$, so

$$P_+ = (3/2)(R_*/R_Y)^{1/2} \int_0^{\pi/2} \sin^2\Theta\, G(\Theta)\, d\Theta \qquad (D.6)$$

and the total probability that we see at least one pulse is

$$P_1 = 2P_+ = 3(R_*/R_Y)^{1/2} \int_0^{\pi/2} \sin^2\Theta\, G(\Theta)\, d\Theta\ . \qquad (D.7)$$

By numerical integration

$$\int_0^{\pi/2} \sin^2\Theta\, G(\Theta)\, d\Theta = 0.620958\ , \qquad (D.8)$$

so

$$P_1 = 1.8629\ (R_*/R_Y)^{1/2}\ . \qquad (D.9)$$

[Of course, we could also obtain P_1 from

$$P_1(T) = \int_0^{\infty} P_y(y,T)\, dy \qquad (D.10)$$

which becomes (see Appendix B),

$$P_1(T) = 1/2\ T^{-\gamma/2}\ k^{1/2}\ \lambda\ . \qquad (D.11)$$

Using the definitions of k and R_ρ, we find that

$$T^{-\gamma/2}\ k^{1/2} = (3/2\pi)(R_*/R_Y)^{1/2}\ , \qquad (D.12)$$

so that Eq. (D.11) becomes

$$P_1(T) = (3\lambda/4\pi)(R_*/R_Y)^{1/2} \quad . \tag{D.13}$$

The numerical value of $\lambda = 7.772$, so that $3\lambda/4\pi = 1.855$. The difference between Eqs. (D.9) and (D.13) is about 0.4%, perfectly satisfactory agreement considering the approximations used in the derivation of Eq. (B.19)].

We now consider the number of pulsars expected to show two pulses. The region of $\Theta - \phi$ space for which Eqs. (D.1) and (D.2) hold simultaneously is illustrated in Figure D.1. When weighted with $1/2 \sin\Theta\ 1/2 \sin\phi$, this area is the probability of a pulsar showing an interpulse,

$$P_2 = \int_{\pi/2-\psi_b}^{\pi/2} \frac{1}{2} \sin\phi \, d\phi \int_{\pi-\phi-\psi_b}^{\phi+\psi_b} \frac{1}{2} \sin\Theta \, d\Theta + \int_{\pi/2}^{\pi/2+\psi_b} \frac{1}{2} \sin\phi \, d\phi \int_{\phi-\psi_b}^{\pi-\phi+\psi_b} \frac{1}{2} \sin\Theta \, d\Theta \quad . \tag{D.14}$$

Clearly the two contributions are equal; evaluating the first gives

$$P_2 \simeq 2 \cdot \frac{1}{2} \cdot \frac{1}{2} \int_{\pi/2-\psi_b(\frac{\pi}{2})}^{\pi/2} \sin\phi [2 \sin\phi \sin\psi_b(\tfrac{\pi}{2}) - 2 \cos\phi \cos\psi_b(\tfrac{\pi}{2})] \, d\phi \quad , \tag{D.15a}$$

$$P_2 \simeq \frac{1}{2} \psi_b(\tfrac{\pi}{2}) \sin\psi_b(\tfrac{\pi}{2}) \simeq \frac{1}{2} \psi_b^2(\tfrac{\pi}{2}) \simeq 0.433 \, (R_*/R_Y) \quad . \tag{D.15b}$$

[This agrees with the observation that the weighting factor is very nearly 1/4 in the region of integration, and that the area of the square is $(2\psi_b/\sqrt{2})^2 = 2\psi_b^2(\frac{\pi}{2})$.]

FIGURE CAPTION

Figure D.1. The regions of (θ,ϕ)-space. Entire hatched area, observer detects at least one pulse. Cross-hatched area, observer detects both pulses.

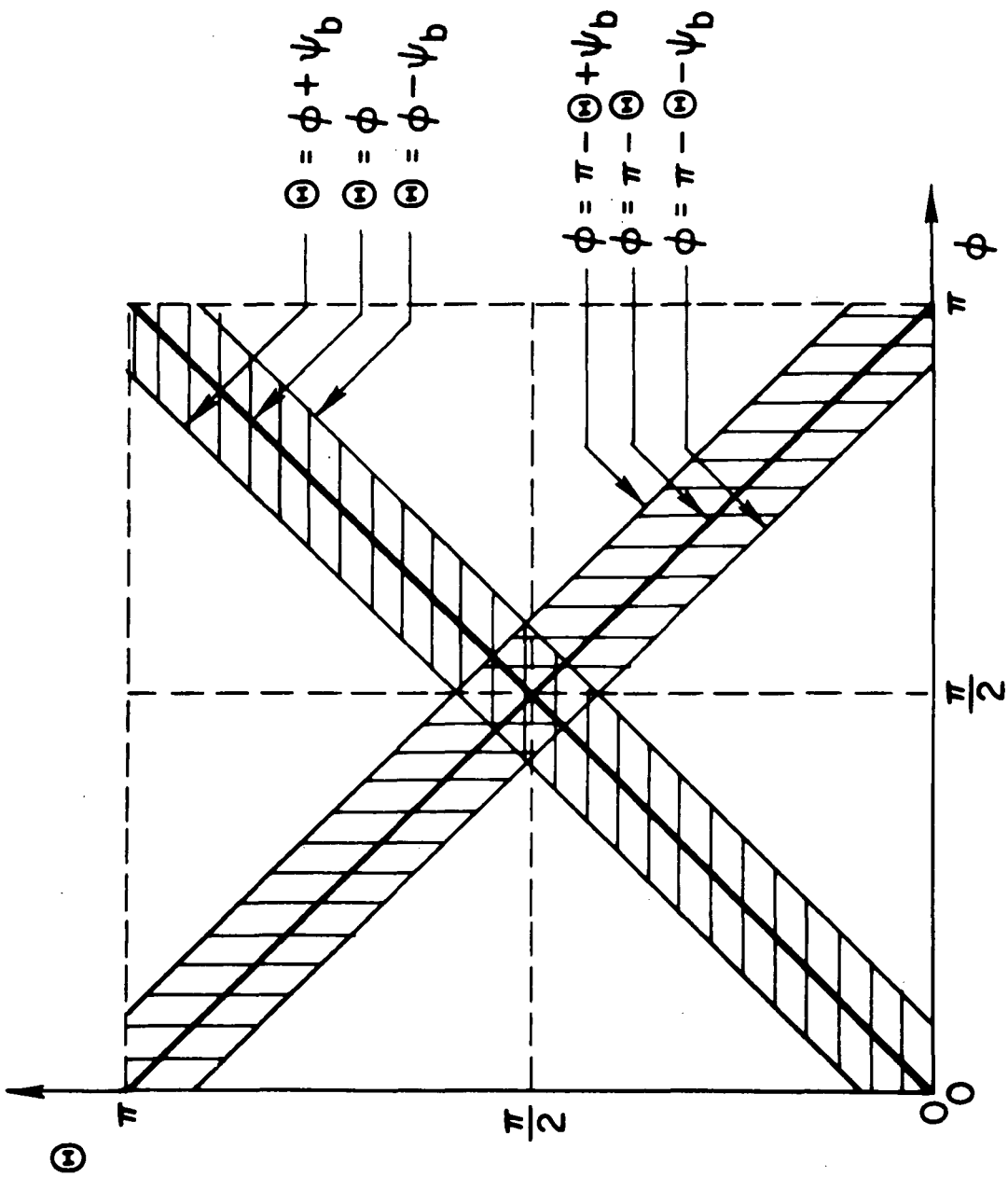

Figure D.1

BIBLIOGRAPHY

Alfvén, H. 1954, On the Origin of the Solar System (New York: Oxford University Press).

Backer, D.C. 1970, Nature 228, 42.

_____. 1973, Ap. J. 182, 245.

Backer, D.C., Boriakoff, V., and Manchester, R.N. 1973, Nature Phys. Sci. 243, 77.

Baym, G., Pethic, C., and Sutherland, P. 1971, Ap. J. 170, 299.

Boynton, P.E., Groth, E.J., Hutchinson, D.P., Nanos, G.P., Jr., Partridge, R.B., and Wilkinson, D.T. 1972, Ap. J. 175, 217.

Chiu, H.-Y. and Canuto, V. 1971, Ap. J. 163, 577.

Clark, J.W., Heintzmann, H., Hillebrandt, W., and Grewing, M. 1971, Astrophys. Lett. 10, 21.

Cocke, W.J., Disney, M.J., and Taylor, D.J. 1969, Nature 221, 525.

Cohen, J.M. and Cameron, A.G.W. 1971, Astrophys. Sp. Sci. 10, 227.

Davies, J.G. and Large, M.I. 1970, M.N.R.A.S. 149, 301.

Dicke, R.H. 1964, Nature 202, 432.

Duthie, J.G. and Murdin, P. 1971, Ap. J. 163, 1.

Eastlund, B.J. 1969, Nature 220, 1293.

_____. 1970, Nature 225, 430.

Fritz, G., Henry, R.C., Meekins, J.F., Chubb, T.A., and Friedman, H. 1969, Science 164, 709.

Furth, H.P., Killeen, J., and Rosenbluth, M.N. 1963, Phys. Fluids 6, 459.

Ginzburg, V.L. 1971, Sov. Phys. Uspekhi 14, 83.

Ginzburg, V.L. and Usov, V.V. 1972, ZhETF Pis. Red. 15, 280.

Ginzburg, V.L., Zheleznyakov, V.V., and Ziatsev, V.V. 1969, Astrophys. Sp. Sci. 4, 464.

Gold, T. 1968, Nature 218, 731.

_____. 1969, Nature 221, 25.

Goldreich, P. and Julian, W.H. 1969, Ap. J. 157, 869.

Greenstein, G. 1972, Ap. J. 177, 251.

Gunn, J.E. 1971, Pub. A.S.P. 83, 594.

Gunn, J.E. and Ostriker, J.P. 1969, Nature 221, 454.

_____. 1970, Ap. J. 160, 979.

ter Haar, D. 1972, Phys. Rep. 3C, 57.

Harnden, F.R., Johnson, W.N., III, and Haymes, R.C. 1972, Ap. J. (Lett.) 172, L91.

Haymes, R.C., Ellis, D.V., Fishman, G.J., Glenn, S.W., and Kurfess, J.D. 1968, Ap. J. (Lett.) 151, L131.

Henry, G.R. and Paik, H.-J. 1969, Nature 224, 1189.

Hewish, A. 1970, Ann. Rev. Astron. Astrophys. 8, 265.

Hillier, R.R., Jackson, W.R., Murray, A., Redfern, R.M., and Sake, R.G. 1970, Ap. J. (Lett.) 162, L177.

Huguenin, G.R., Manchester, R.N., and Taylor, J.H. 1971, Ap. J. 169, 97.

Julian, W.H. 1973, to be published in Ap. J.

Komesaroff, M.M. 1970, Nature 225, 612.

Landau, L.D. and Lifshitz, E.M. 1960, Mechanics (Oxford: Pergamon Press), p. 128.

Lehnert, B. 1960, Rev. Mod. Phys. 32, 1012.

Lerche, I. 1970a, Ap. J. 160, 1003.

_____. 1970b, Ap. J. 162, 153.

Leung, Y.C. and Wang, C.G. 1971, Ap. J. 170, 499.

Lyne, A.G., Smith, F.C., and Graham, D.A. 1971, M.N.R.A.S. 153, 337.

Manchester, R.N. 1971a, Nature Phys. Sci. 231, 189.

_____. 1971b, Ap. J. Suppl. 23, No. 199, 283.

Maran, S.P. and Modali, S.B. 1970, Earth and Extraterr. Sci. 1, 147.

Mestel, L. 1973, Nature Phys. Sci. 233, 149.

Michel, F.C. 1969, Ap. J. 158, 727.

_____. 1973a, Ap. J. 180, 207.

_____. 1973b, Ap. J. (Lett.) 180, L133.

Ostriker, J.P. and Gunn, J.E. 1969, Ap. J. 157, 1395.

Pacini, F. 1968, Nature 219, 145.

_____. 1971, Ap. J. (Lett.) 169, L11.

Pacini, F. and Rees, M. 1970, Nature 226, 622.

Papaliolios, C., Carleton, N.P., and Horowitz, P. 1970, Nature 228, 445.

Radhakrishnan, V. and Cooke, D.J. 1969, Astrophys. Lett. 3, 225.

Radhakrishnan, V., Cooke, D.J., Komesaroff, M.M., and Morris, D. 1969, Nature 221, 443.

Radhakrishnan, V. and Manchester, R.N. 1969, Nature 222, 228.

Rankin, J.M., Campbell, D.B., and Counselmann, C.C., III 1971, Paper presented at 136th Meeting of AAS, San Juan, Puerto Rico, Dec. 5-8.

Rankin, J. and Counselmann, C.C., III 1973, Ap. J. 181, 875.

Rankin, J., Counselmann, C.C., III and Richards, D. 1971, Astron. J. 76, 686.

Rankin, J.M. and Roberts, J.A. 1971, IAU Symp. No. 46 (Dordrecht: Reidel Publishing Co.), p. 114.

Reichley, P.E. and Downs, G.S. 1969, Nature 222, 229.

_____. 1971, Nature Phys. Sci. 234, 48.

Richards, D.W., Pettengill, G.H., Counselmann, C.C., III and Rankin, J.M. 1970, Ap. J. (Lett.) 160, L1.

Roberts, J.A. and Richards, D.W. 1971, Nature Phys. Sci. 231, 25.

Roberts, D.H. and Sturrock, P.A. 1972a, Ap. J. 172, 435 (Paper I).

_____. 1972b, Ap. J. (Lett.) 173, L33 (Paper II).

_____. 1973, Ap. J. 181, 161 (Paper III).

Roberts, D.H., Sturrock, P.A., and Turk, J.S. 1973, Stanford University Institute for Plasma Research Report No. 503, Stanford University, Stanford, California, to be pub. in Annals of the New York Academy of Sciences.

Ruderman, M. 1969, Nature 223, 597.

_____. 1971, Phys. Rev. Lett. 27, 1306.

_____. 1972, Ann. Rev. Astron. Astrophys. 10, 427.

Scargle, J.D. 1969, Ap. J. 156, 401.

Scargle, J.D. and Harlan, E.A. 1970, Ap. J. (Lett.) 159, L143.

Scargle, J.D. and Pacini, F. 1971, Nature Phys. Sci. 231, 144.

Scharlemann, E.T. and Wagoner, R.V. 1973, Ap. J. 182, 951.

Schmidt, G. 1966, Physics of High Temperature Plasmas (New York: Academic Press).

Shklovsky, I.S. 1968, Supernovae (London: Wiley).

_____. 1970, Ap. J. (Lett.) 159, L77.

Spitzer, L. 1962, The Physics of Fully Ionized Gases (New York: Interscience).

Sturrock, P.A. 1966, Phys. Rev. Lett. 16, 270.

_____. 1970, Nature 227, 465.

_____. 1971a, Ap. J. 164, 529.

_____. 1971b, Ap. J. (Lett.) 169, L7.

Sturrock, P.A. and Smith, S.M. 1968, Sol. Phys. 5, 87.

Sutton, J.M., Staelin, D.H., and Price, R.M. 1971, IAU Symp. No. 46 (Dordrecht: Reidel Publishing Co.), p. 97.

Tademaru, E. 1971, Astrophys. Sp. Sci. 12, 193.

Taylor, J.H. and Huguenin, G.R. 1971, Ap. J. 167, 273.

Terzian, Y. 1973, privately circulated data tables.

Turk, J.S. 1972, private communication.

Turk, J.S., Sturrock, P.A., and Petrosian, V. 1973, Stanford University Institute for Plasma Research Report No. 529, submitted to Ap. J. Lett.

Wang, C.G. and Sartori, L. 1973, preprint.

Weber, E.J. and Davis, L.J. 1967, Ap. J. 148, 217.